Dissertation

Johannes Thielking

Hyperfine studies of Th-229 in its nuclear ground and isomeric state

Die Serien der PTB-Berichte:

Dosimetrie	PTB-Dos
Elektrizität	PTB-E
Elektronische Entwicklung	PTB-EW
Fertigungsmesstechnik	PTB-F
Informationstechnik	PTB-IT
Mechanik und Akustik	PTB-MA
Medizinische Messtechnik	PTB-MM
Neutronenphysik	PTB-N
Optik	PTB-Opt
Physikalische Grundlagen	PTB-PG
Radioaktivität	PTB-Ra
Thermodynamik	PTB-Th
Explosionsschutz	PTB-Ex
Chemische Physik	PTB-CP

Eingestellte Serien:

Akustik	(bis 1985)	PTB-Ak
Forschungs- und Meßreaktor Braunschweig	(bis 1988)	PTB-FMRB
Institut Berlin	(bis 1985)	PTB-IB
Mechanik	(bis 1985)	PTB-Me
Neutronendosimetrie	(bis 1988)	PTB-ND
Sicherstellung und Endlagerung radioaktiver Abfälle	(bis 1989)	PTB-SE
Wärme	(bis 3/97)	PTB-W
Literaturzusammenstellungen und Veröffentlichungshinweise	(bis 2001)	PTB-L
Akkreditierung, Qualitätsmanagement, Zertifizierung	(bis 2003)	PTB-AQZ
Atomphysik	(bis 2003)	PTB-APh
Internationale Organisation für Gesetzliches Messwesen	(bis 2003)	PTB-OIML
Thermodynamik und Explosionsschutz	(bis 2003)	PTB-ThEx
Technisch-Wissenschaftliche Dienste	(bis 2003)	PTB-TWD

Physikalisch-Technische Bundesanstalt

Johannes Thielking

Hyperfine studies of Th-229 in its nuclear ground and isomeric state

Hyperfine studies of Th-229 in its nuclear ground and isomeric state

Von der Fakultät für Mathematik und Physik
der Gottfried Wilhelm Leibniz Universität Hannover

zur Erlangung des akademischen Grades
Doktor der Naturwissenschaften
Dr. rer. nat.

genehmigte Dissertation von

Johannes Thielking, M.Sc.

2020

To my wife Susanne,

for her incredible support in everything I do.

Abstract

The ^{229}Th nucleus possesses an exceptionally low-lying isomeric state of about $8\,\text{eV}$, about four orders of magnitude lower than common nuclear excitation energies. This state is coupled to the ground state by a magnetic dipole transition with an estimated linewidth of less than $1\,\text{mHz}$. It has been proposed to use this unique transition as a reference for a new type of optical clock. Such a nuclear clock is expected to be highly immune to perturbations from external electromagnetic fields, as well as a sensitive probe for temporal variations of fundamental constants.

A non-destructive optical detection method for the isomeric state is a key feature in the ongoing experimental search for the direct excitation of the nucleus, as well as the future clock operation. The realization of such a detection scheme based on hyperfine spectroscopy is the main focus of this thesis. To this end, the hyperfine structures of several electronic transitions in ^{229}Th$^+$ and ^{229}Th^{2+} are investigated. Their splitting constants, as well as their isotope shift with respect to ^{232}Th are measured using laser spectroscopy. Measurements are also performed on thorium ions produced by the α decay of ^{233}U, where $2\,\%$ of the thorium ions are in the isomeric state. This led to the first optical detection of the isomer via hyperfine spectroscopy and to the measurement of its nuclear magnetic dipole moment $\mu = -0.37(6)\,\mu_N$, its electric quadrupole moment $Q_s = 1.74(6)\,eb$, as well as the increase in mean squared charge radius compared to the nuclear ground state $\delta\langle r^2\rangle^{229\text{m},229} = 0.0107(16)\,\text{fm}^2$. Based on these values, a first experimental estimation on the sensitivity of the nuclear transition to temporal variations of the fine structure constant α is given.

In a further experiment, the excitation of the isomeric state in ^{229}Th^{2+} via electronic bridge processes is investigated. Selected electronic states of ^{229}Th^{2+} are addressed in a two-step excitation scheme to search for a coupling to the nuclear transition in the energy range from $7.14\,\text{eV}$ to $10.46\,\text{eV}$. Since no excitation has been observed so far, limits on the detectable excitation rate are given.

Thorium, Th-229, nuclear clock, hyperfine spectroscopy, electronic bridge

Contents

Chapter 1

Introduction

Precise clocks are essential in a wide range of daily applications, e.g., in global navigation satellite systems (GNSS) or in high-speed network synchronization, with the best available timekeepers being atomic clocks [1]. They are also employed in fundamental research, like the search for dark matter [2], tests of the local Lorentz invariance [3] and tests of the temporal variation of fundamental constants [4].

Atomic clocks are based on the principle of coupling an electromagnetic oscillator (e.g., microwave generator or laser) to a transition frequency of a certain chemical element [1]. The success of this concept is visible in the fact, that the current definition of the second, the SI unit of time, is based on the ground-state hyperfine transition frequency of the caesium-133 atom [5]. An improvement in clock performance can therefore be expected to benefit fundamental science, as well as industrial applications.

Two of the main characteristics of a clock are its accuracy and its stability. A visualization of this properties is given in Fig. 1.1. The accuracy determines how well the natural frequency f_0 of the transition is realized over a long averaging period. It can be described by the relative shift $\delta f/f_0$ from the transition and the relative uncertainty u/f_0 of the shift. Usually the relative uncertainty is the determining value when comparing clock performance, since the absolute shift can be taken into account in the evaluation. Current optical atomic clocks based on optical transitions in trapped ions or atoms (e.g., Yb^+, Al^+, In^+, Sr, Yb) can reach fractional uncertainties below 10^{-18} [6].

The stability of a clock is influenced by several factors which cause the mea-

sured frequency to fluctuate over time, which is usually characterized by the Allan deviation $\sigma_y(\tau)$ [1]. A fundamental limitation of the stability of optical clocks is the so called quantum projection noise, arising from the quantum fluctuation in the state detection. This influence on the stability can be reduced by investigating a larger ensemble of particles, since $\sigma_y \propto 1/\sqrt{N}$, with N being the number of atoms or ions that are investigated. Among the most stable clocks are currently strontium lattice clocks with a reported fractional instability of $4.8 \cdot 10^{-17}\tau^{-1/2}$ [7].
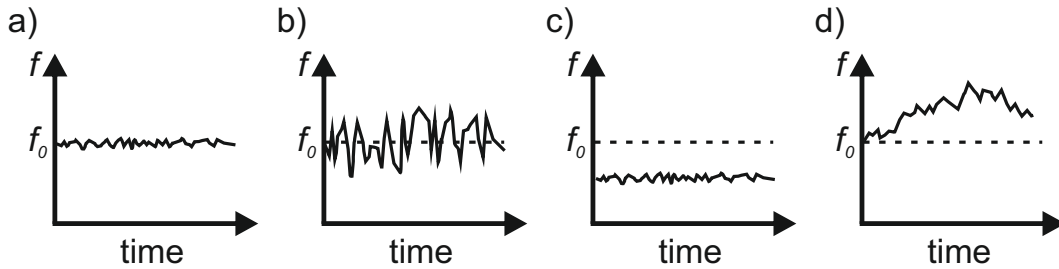
Figure 1.1: **Schematic representation of different clock performances.** a) stable and accurate, b) accurate but not stable, c) stable but not accurate, d) neither stable nor accurate.

1.1 ^{229}Th nuclear clock

In 2003, a new type of optical clock based on a magnetic dipole transition inside the nucleus ^{229}Th between its ground state and its first excited state has been proposed [8]. The excited state, denoted ^{229m}Th, lies at an energy of 8.28(17) eV [9] and is the lowest of all known long-lived nuclear excited states, called isomers. This transition of ^{229}Th is currently the only viable candidate for a 'nuclear clock', since its wavelength of 150(3) nm can be produced with current laser technology.

The second lowest isomer, ^{235m}U, has an excitation energy of about 76.7 eV [10] with a corresponding wavelength of 16 nm. However, its expected radiative lifetime of about 10^{15} years and its large internal conversion factor on the order of 10^{20} [11] make it unsuitable as a clock transition.

In the case of a bare ^{229}Th nucleus, the nuclear transition is expected to have a linewidth of < 1 mHz [12]. It is also expected to be less sensitive to external

perturbations, like frequency shifts caused by electromagnetic fields, compared to atomic clock transitions, due to the significantly smaller size of the nucleus compared to an atom. It has been shown for the ^{229}Th^{3+} ion, that influences from external fields on the nuclear transition can be strongly suppressed by choosing specific electronic states, so called stretched states [13]. The resulting relative inaccuracy for a single ion clock was estimated as $1.5 \cdot 10^{-19}$.

A unique feature of nuclear transitions is, that they can be investigated while the atom is bound in a solid state. This gives the chance to build a solid state nuclear clock based on $\approx 10^{14}$ nuclei doped inside a transparent crystal (see, e.g., Refs. [14; 15]). Although the accuracy of such a clock is limited by the influence of the crystal lattice environment, it is expected to reach a stability of $10^{-17}\tau^{-1/2}$. It could therefore serve as a secondary standard when calibrated with respect to a primary clock.

A clock based on the ^{229}Th nuclear transition has also been proposed as a highly sensitive system with respect to temporal variations of the fine-structure constant $\alpha = e^2/4\pi\epsilon_0\hbar c$ and the strong interaction parameter m_q/Λ_{QCD} [16]. This proposal is based on the model, that the small energy difference between ground state and isomer is the result of a near cancellation of the change in Coulomb energy and the change in nuclear energy linked to the strong interaction. Both contributions are expected to be in the keV to MeV energy range, but with opposite signs. The sensitivity to a change in α arises from the ratio of the change in Coulomb energy to the isomer excitation energy, which is about five orders of magnitude.

1.2 $^{229\mathrm{m}}$Th history

Although the existence of this low energy nuclear transition in ^{229}Th has been assumed for several decades, the corresponding optical clock has not been realized yet. The main hindrances are the challenges related to the measurement of a nuclear transition energy with sufficient precision. The following section gives a short overview of central research advances concerning ^{229}Th with regards to its isomeric state. A more comprehensive review of theoretical and experimental investigations can be found in Ref. [17].

The first indication of a nuclear level with very low energy in ^{229}Th was

given in 1976 by Kroger and Reich [18]. Analyzing the γ-spectrum of ^{229}Th after its production via α decay of ^{233}U, they identified that the bandhead of the $K^\pi = 3/2^+$ rotational band (see Ch. 2) must lie within $100\,\text{eV}$ of the ground state to satisfy the observed level structure. Further independent support for the existence of this low-lying state came from the investigation of ^{230}Th$(d,t)^{229}$Th reactions in 1990 [19].

A first energy measurement was published in the same year by Reich and Helmer, based on the energy difference of γ-ray transitions ending up in the nuclear ground state and the low-lying isomer. The γ-photons were measured with an intrinsic germanium detector and the energy difference between the two states was given as $\Delta E = -1(4)\,\text{eV}$ [20], which was updated to $\Delta E = 3.5(1.0)\,\text{eV}$ in 1994 by the same group [21].

In 2007, an analysis of the γ-photons emitted by ^{229}Th with higher resolution was published [12]. In this study the authors used a microcalorimeter spectrometer to determine the energies of the photons emitted from selected intraband and interband transitions (see Fig. 1.2). The energy of the low-lying isomer has been determined as $7.6(5)\,\text{eV}$ by calculating the difference of these energies. This value was updated by the same group to $7.8(5)\,\text{eV}$ in 2009 [22].

Results of an experiment for the direct optical excitation of the isomer were published in 2015 [23]. The authors exposed a ^{229}Th-doped LiSrAlF$_6$ crystal to tunable synchrotron radiation and measured the resulting fluorescence. However, they reported no evidence of the nuclear excitation for the energy range from $7.3\,\text{eV}$ to $8.8\,\text{eV}$ and isomer lifetime of $(1-2)\,\text{s} < \tau < (2000-5600)\,\text{s}$.

A first direct observation of the decay of the isomeric state was reported by the thorium group at the Ludwig-Maximilians-Universität München (LMU) in 2016 [24]. In this experiment, ^{229}Th was also produced via α decay of ^{233}U. Of all produced thorium nuclei via this process, $2\,\%$ end up in the isomeric state. Using a buffer-gas stopping cell and a radio frequency (rf) quadrupole mass separator, a monoisotopic beam of ^{229}Th ions with charge states up to $3+$ was formed and subsequently deposited on a microchannel plate (MCP). On the MCP the ions neutralized, which opens the internal conversion decay channel for the isomer, since the ionization potential of neutral thorium ($E = 6.3\,\text{eV}$, Ref. [25]) is below the isomer energy. The isomer excitation energy is therefore transferred to the outermost electron, which is ejected from the atom. These
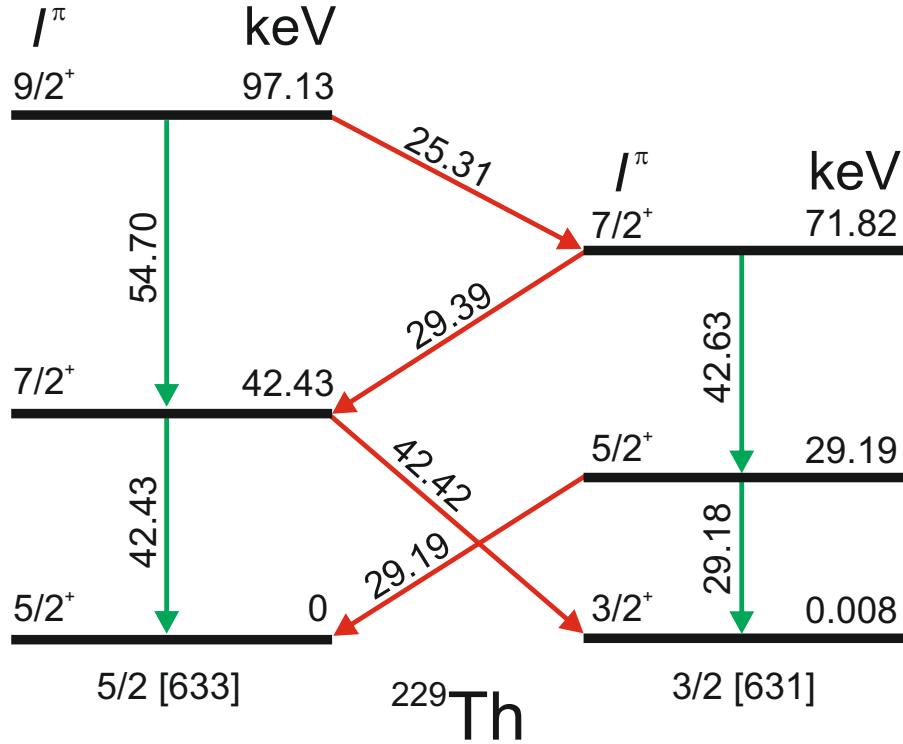
Figure 1.2: **Partial level structure of the ^{229}Th nucleus.** The three lowest levels of the two rotational bands $5/2^+[633]$ and $3/2^+[631]$ of ^{229}Th are shown, labeled by their nuclear momentum I, parity π and excitation energy [12]. Intraband and interband transitions are depicted as green and red arrows, respectively.

electrons were then detected using the MCP, a phosphor screen and a CCD camera.

In 2017, a collaboration of the thorium group at the Physikalisch-Technische Bundesanstalt (PTB), the group at LMU and the group for super heavy elements at the Johannes Gutenberg-Universität Mainz (JGU) performed the first measurement of the nuclear magnetic dipole and the electric quadrupole moment, as well as the mean squared charge radius of the isomer [26]. These values were obtained via hyperfine spectroscopy of isomeric ^{229}Th^{2+} ions. This experiment is a central part of this thesis and will be discussed in Ch. 5 and Ch. 6.

Recently, the LMU group reported an improved value for the isomer energy [9]. Using a modified version of their experimental apparatus which is

introduced above, they measured the excess energy of the electron which is emitted after internal conversion. To this end, the ions were neutralized in flight by passing through a graphene foil and the energy of the subsequently emitted electrons was measured with a magnetic bottle spectrometer to deduce an isomer excitation energy of $8.28(17)\,\mathrm{eV}$. This result was most recently supported by the determination of the isomer energy as $E = 8.30(92)\,\mathrm{eV}$ from γ-spectroscopy of the decay of the $5/2^+[631]$ level (see Fig. 1.2) in Ref. [27]. This experiment benefited from the precise determination of the branching ratio from this level to ground state and isomer, as well as the energy of the $5/2^+[633] \rightarrow 5/2^+[631]$ transition in Ref. [28].

However, the current uncertainty of the isomer excitation energy is still about 17 orders of magnitude larger than the expected natural linewidth. Optical excitation of the isomeric state is expected to significantly improve its energy determination. For this reason, various excitation schemes are currently pursued by several experimental groups (see, e.g., Ref. [29]). Two of these schemes are presented in Ch. 7 and Ch. 8.

1.3   This thesis

The structure and main aspects of this thesis are outlined hereafter by a short description of each chapter:

- **Chapter 2** gives an overview of the theoretical models used throughout the thesis to describe nuclear and atomic properties of ^{229}Th. A short introduction to selected nuclear models is followed by a description of the interaction between nucleus and electrons in the form of hyperfine splitting and the isotope shift. The energy transfer between nucleus and electron shell is discussed with a focus on the electronic bridge mechanism.

- **Chapter 3** introduces the experimental apparatus used to perform hyperfine spectroscopy on Th$^+$ and Th^{2+} ions and to search for optical excitation of the nucleus. It consists of two different ion traps, one at PTB and one at LMU, as well as the employed laser excitation and detection system. For the system at PTB, the production and long-term storage of Th^{2+} ions are discussed.

- **Chapter 4** describes hyperfine spectroscopy experiments performed on Th$^+$ ions, which are aimed at identifying an isomeric signal using ions loaded

from a ^{233}U recoil source. These experiments include the investigation of the hyperfine structure (HFS) of the 49960 cm^{-1} level via two-step excitation, following up on previous experiments [30; 31].

- In **Chapter 5**, selected optical electronic transitions of Th^{2+} are investigated. In particular, the isotope shift between ^{229}Th^{2+} and ^{232}Th^{2+}, as well as the hyperfine structure of these lines in ^{229}Th^{2+} are measured. Doppler-free hyperfine spectroscopy is also performed on isomeric ^{229m}Th ions, conducted in cooperation with LMU and JGU.

- **Chapter 6** gives the evaluation of the isomer HFS to deduce the underlying nuclear moments and the mean squared charge radius. These values are then used to make estimates on the performance of a future ^{229}Th nuclear clock and its sensitivity to temporal variations of the fine structure constant α.

- **Chapter 7** discusses an experiment aimed at the optical excitation of the nucleus in ^{229}Th^{2+} ions via electronic bridge processes [32; 33]. Hyperfine spectroscopy is employed in this experiment as a nuclear state detection scheme.

- **Chapter 8** presents a summary of the main results of this thesis, as well as planned steps for the future. This includes an experiment for direct optical excitation of the isomer based on a four-wave mixing laser system.

Chapter 2

Nuclear and atomic theory

This chapter provides a short introduction to the theoretical background used throughout this thesis. The first two parts are a brief overview of nuclear models leading up to the Nilsson model, which is usually used to describe strongly deformed nuclei and their excitation states, such as ^{229}Th and $^{229\mathrm{m}}$Th, and their treatments of nuclear moments. This overview is based on Ref. [34]. The third part introduces the interaction between the electron shell and the nucleus, resulting in the hyperfine structure of spectroscopic lines and the isotope shift. This part is based on Refs. [35; 36]. The fourth section discusses the energy transfer between the nucleus and the electron shell, in particular via the electronic bridge process.

2.1   Nuclear models

So far, no complete treatment of the atomic nucleus in the framework of quantum chromodynamics is available. Nuclear models are therefore adjusted to incorporate specific nuclear properties. In the nuclear shell model, the nucleons are treated as independent non-interacting particles inside a mean potential. This model is derived analogously to the electronic states of an atom, where the Coulomb potential acting on the electrons is replaced by a mean potential arising from the attractive force between the nucleons. This potential has to account for the nuclear radius, which has been experimentally observed to be well defined. A suitable potential, which also incorporates continuity, is the

Woods-Saxon potential:

$$V(r) = -V_0 \left(1 + e^{\frac{r-R}{a}} \right)^{-1}. \tag{2.1}$$

V_0 is the potential depth, R is the nuclear radius and a represents the surface thickness. This potential, which lies between a box potential and a harmonic oscillator (see Fig. 2.1), agrees well with the measured density distribution of the nucleons. This model already describes discrete excitations of the nucleus, which are not present in more simplified models, like the droplet model.
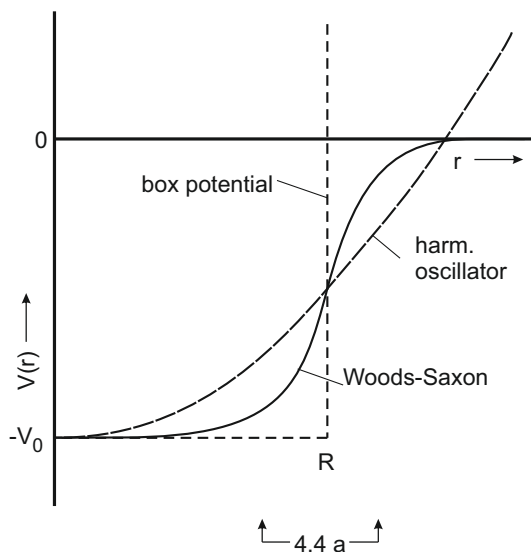
Figure 2.1: **Comparison of nuclear model potentials.** The Woods-Saxon potential can be viewed as a compromise between a box potential and a harmonic oscillator to describe the nuclear potential. It incorporates the nuclear radius R, as well as the surface thickness a. The figure is adapted from Ref. [34].

A characteristic feature of nuclear structure are the so called magic numbers of protons and neutrons, at which the separation energy to remove one nucleon exhibits a large step. This phenomenon arises from the closure of a neutron or proton shell. To incorporate this effect into the model, one has to take into account the spin-orbit coupling of the nucleons. This is achieved by adding an energy term that is dependent on the scalar product of angular momentum $\vec{l}$ and spin $\vec{s}$ of the nucleon:

$$V_i = V(r) + V_{ls}(r)(\vec{l} \cdot \vec{s}). \tag{2.2}$$

The expectation value of $\vec{l}\cdot\vec{s}$ can be derived from the square of the total angular momentum $\vec{j} = \vec{l} + \vec{s}$:

$$\langle \vec{l}\cdot\vec{s}\rangle = \frac{1}{2}\left[\langle j^2\rangle - \langle l^2\rangle - \langle s^2\rangle\right] = \frac{1}{2}[j(j+1) - l(l+1) - \frac{3}{4}]. \qquad (2.3)$$

The radial function $V_{ls}(r)$ can be assumed constant for a simplified discussion of the nuclear level structure.

So far, the nuclear model always used a spherically symmetric potential, but this assumption is only valid in the case of closed shells. In fact, for partially filled shells experiments show large quadrupole moments which indicate strong nuclear deformations. A model to describe these deformed nuclei was presented by Nilsson in 1955 [37]. Instead of using a deformed Woods-Saxon potential, he used a deformed harmonic oscillator to simplify calculations:

$$V(\vec{r}) = \frac{m}{2}[\omega_{xy}^2(x^2 + y^2) + \omega_z^2 z^2], \qquad (2.4)$$

with m being the magnetic quantum number associated to the total angular momentum $\vec{j}$. To account for the deviation from the Woods-Saxon potential, a correction term Dl^2 was added. For the contribution of the spin-orbit coupling $V_{ls}(r) = C = const$ was assumed:

$$V_i = \frac{m}{2}[\omega_{xy}^2(x^2 + y^2) + \omega_z^2 z^2] + C\vec{l}\cdot\vec{s} + Dl^2. \qquad (2.5)$$

Taking into account a constant nuclear volume, the two frequencies ω_{xy} and ω_z can be defined as

$$\omega_z = \omega_0(1 - \frac{2}{3}\delta), \ \omega_{xy} = \omega_0(1 + \frac{1}{3}\delta), \qquad (2.6)$$

employing the deformation parameter δ. The deformation can also be expressed by the Nilsson quadrupole deformation parameter ϵ_2 as [38]:

$$\epsilon_2 = \delta + \frac{1}{6}\delta^2 + \frac{5}{18}\delta^3 + \frac{37}{216}\delta^4 + ..., \qquad (2.7)$$

which is related to the deformation parameter β_2 via:

$$\beta_2 = \sqrt{\frac{16\pi}{5}}\sum_{n=1}^{\infty}\frac{1}{3^n}\epsilon_2^n. \qquad (2.8)$$

The resulting single particle energy levels are characterized by the asymptotic quantum numbers [N,n_z,l_z], together with the nuclear spin I and the parity.

$N = n_x + n_y + n_z$ is the main quantum number of the potential, n_z and l_z are excitation and angular momentum along the z-axis. In the case of ^{229}Th, the nuclear ground state is described as $5/2^+[633]$ and the isomer as $3/2^+[631]$.

The Nilsson model only takes into account the quadrupole deformation of the nucleus, which has been estimated for ^{229}Th to be $\beta_2 \approx 0.24$ [39]. However, ^{229}Th is predicted to also exhibit an octupole ($\beta_3 \approx 0.115$ [39]) and a hexadecapole ($\beta_4 \approx 0.114$ [40]) deformation, resulting in a reflection-asymmetric pear-like shape (see Fig. 2.2). These higher multipolarity deformations need to be accounted for in model approaches to describe the ^{229}Th nucleus, e.g., in order to predict the radiative transition probability between isomeric and nuclear ground state [39].
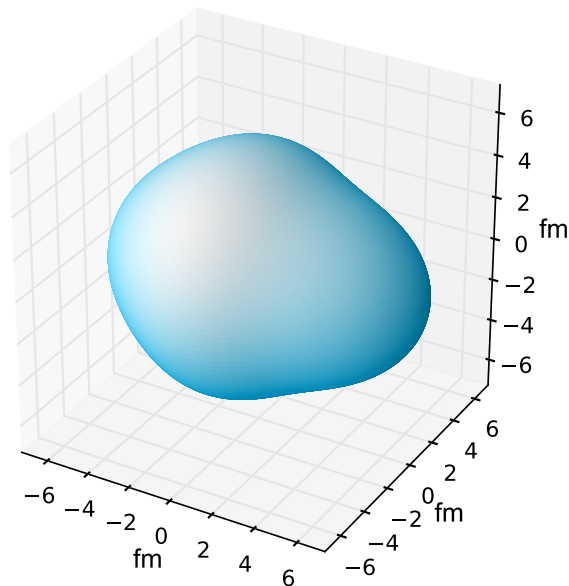
Figure 2.2: **Simulated shape of the ^{229}Th nucleus.** The shape is based on the theoretically predicted deformation parameters β_2, β_3 and β_4 presented in Refs. [39; 40] and the experimentally determined nuclear radius given in Ref. [41].

Deformed nuclei can also show collective excitations in the form of rotations. The Hamilton operator in this case is a combination of inner excitations H_i

and a rotational term H_{rot}:

$$H = H_i + H_{rot} = H_i + \sum_{i=x,y,z} \frac{R_i^2}{2\theta_i}, \tag{2.9}$$

with $\vec{R}$ being the angular momentum of the rotation and θ_i being the effective moments of inertia with respect to the three axes x, y and z, with z being the symmetry axis of the nucleus. Since rotations around the z-axis would be indistinguishable, the expectation value of θ_z is zero. The vector $\vec{R}$ is therefore orthogonal to the z-axis, because excitation energies for rotations around the z-axis are infinitely high. Furthermore, $\theta_x = \theta_y = \theta$ follows from the axial symmetry of the nucleus. The total angular momentum $\vec{I}$ of the nucleus is the sum of the angular momentum of the valence nucleon $\vec{j}$ and the angular momentum $\vec{R}$ of the rotation, $\vec{I} = \vec{j} + \vec{R}$. $\vec{R}$ can therefore be expressed as $\vec{R} = \vec{I} - \vec{j}$. The rotational term is then given by:

$$H_{rot} = (1/2\theta)[I_x^2 + I_y^2 + j_x^2 + j_y^2 - 2(I_x j_x + I_y j_y)]. \tag{2.10}$$

The term $(1/2\theta)(j_x^2 + j_y^2)$ does not dependent on the rotation and can therefore be combined with H_i to H_i'. When including $I_x^2 + I_y^2 = \vec{I}^2 - I_z^2$, Eq. 2.9 can be expressed as:

$$H = H_i' + \frac{1}{2\theta}(\vec{I}^2 - I_z^2) + \frac{1}{\theta}(I_x j_x + I_y j_y). \tag{2.11}$$

When neglecting the last term, which is analogous to the classical Coriolis interaction and expected to be small, the energy values of the rotation can be given as:

$$E_{rot} = \frac{\hbar^2}{2\theta}[I(I+1) - K^2], \tag{2.12}$$

with $K = j_z$ being the projection of $\vec{j}$ along the z-axis. Eq. 2.12 describes therefore a so called *rotational band* of excitations for each value of $\vec{j}$ with

$$I = K, K+1, K+2, ... \ (K \neq 0). \tag{2.13}$$

The case $I = K$ is called the *bandhead* of the rotational band.

2.2 Nuclear moments

Assuming a bare nucleus, the transition between the nuclear ground state and the low-lying isomeric state in ^{229}Th is a magnetic dipole transition (M1). The

nuclear magnetic moments of the two states are therefore of central interest, since they are directly coupled to the transition rate B(M1) [42].

To estimate the magnetic moment of a nucleus one can start with the model developed by Schmidt in 1937 [43]. Following the observation that all nuclei with an even number of protons and an even number of neutrons have a spin of 0, the model assumes that for nuclei with an odd nucleon number the spin and magnetic moment only arise from the unpaired valence nucleon. The nuclear spin $\vec{I}$ is therefore equal to the total angular momentum of this nucleon $\vec{I} = \vec{j} = \vec{l} + \vec{s}$, resulting in $I = l \pm 1/2$. The magnetic moment $\vec{\mu}$ can then be calculated as follows:

$$\vec{\mu} = g\mu_N \vec{I} = (\mu_N/|I|^2)(g_l(\vec{l} \cdot \vec{I}) + g_s(\vec{s} \cdot \vec{I}))\vec{I}. \qquad (2.14)$$

μ_N is the nuclear magneton and the g-factors are $g_s = -3.8263$ and $g_l = 0$ in case of a valence neutron, as it is the case for ^{229}Th. The absolute value of the magnetic moment can therefore be calculated as:

$$\mu = \frac{g_s(I(I+1) + (3/4) - l(l+1))}{2I(I+1)} I\mu_N, \qquad (2.15)$$

resulting in $\mu = -1.913\,\mu_N$ in the case of $I = l + 1/2$ and $\mu = 1.913 \cdot \frac{I}{I+1}\,\mu_N$ for $I = l - 1/2$. These results are also called Schmidt-lines (see Fig. 2.3).

This model only takes into account the valence nucleon, neglecting influences from the remaining nucleus. The results have therefore to be regarded more as limiting cases rather than realistic predictions. Using the more suited Nilsson model and taking into account Coriolis mixing, theoretical predictions for the magnetic moments of the two lowest nuclear states of ^{229}Th were derived in Ref. [44]. The magnetic moment is calculated in this case as:

$$\mu = g_R K + (g_K - g_R)K^2/(I+1). \qquad (2.16)$$

The values for the rotational gyromagnetic ratio $g_R = 0.309(16)$ and the internal gyromagnetic ratio $g_K = 0.128(17)$ of the nuclear ground state $5/2^+[633]$ were taken from Ref. [45]. The value $g_K - g_R = -0.58(9)$ for the isomeric state $3/2^+[631]$ was measured in Ref. [18] and $g_K \approx -0.29$ was estimated based on Ref. [46]. For both states K is equal to I because they are the bandheads of their respective rotational band. The resulting predictions are $\mu_{gr} = 0.45\,\mu_N$ for the nuclear ground state and $\mu_{is} \approx -0.076\,\mu_N$ for the isomeric state.
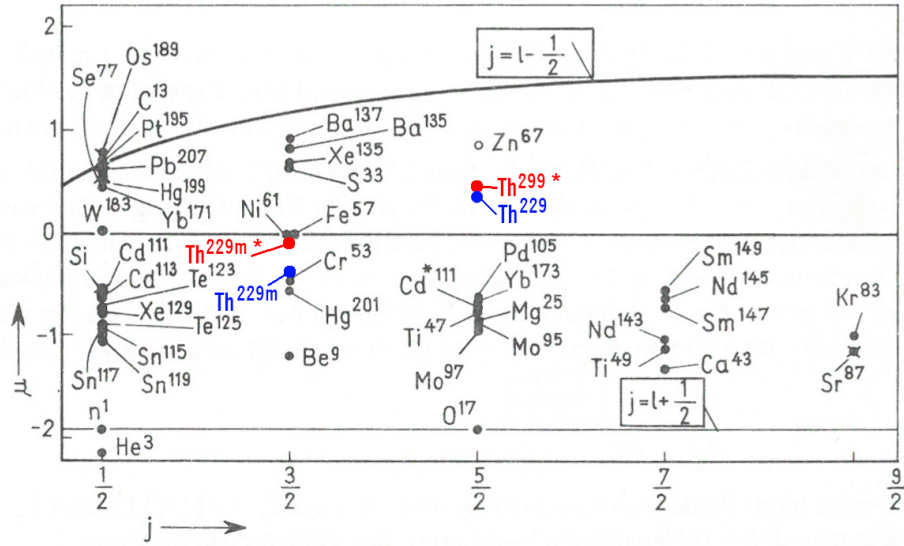
Figure 2.3: **Measured nuclear magnetic moments and Schmidt-lines.**
Magnetic moments of nuclei with an unpaired neutron are shown. The theoretical predictions of the Schmidt model are visible as the so called Schmidt-lines. The dipole moments for the nuclear ground state and isomer of ^{229}Th predicted in Ref. [44] are shown in red and marked with (*). Experimental values are shown in blue, taken from Ref. [47] for the nuclear ground state and measured in this thesis for the isomer. The figure is adapted from Ref. [34].

When the nuclear shape, or rather the charge distribution, differs from a sphere, the nucleus also exhibits an electric quadrupole moment Q_0. If the nucleus is described as a homogeneously charged spheroid with the charge $Z \cdot e$ and the half-axes a and b, the quadrupole moment can be calculated as:

$$Q_0 = \frac{2}{5} Ze(b^2 - a^2) = \frac{4}{5} Ze\bar{R}^2 \left(\frac{\Delta R}{\bar{R}} \right) = \frac{4}{5} Ze\bar{R}^2 \cdot \delta, \qquad (2.17)$$

with $\bar{R} = (a+b)/2$, $\Delta R = (b-a)$ and the previously introduced deformation parameter δ. Q_0 is also called the intrinsic quadrupole moment, which is defined in the body-fixed reference frame of the nucleus. The observable quadrupole moment in the laboratory frame is called the spectroscopic quadrupole moment Q_s, which is related to Q_0 by [48]:

$$Q_s = Q_0(3K^2 - I(I+1))/((I+1)(2I+3)). \qquad (2.18)$$

In the case of ^{229}Th, it follows that $Q_s = \frac{5}{14} Q_0$ for the nuclear ground state

$(I = 5/2)$ and $Q_s = \frac{1}{5}Q_0$ for the isomeric state $(I = 3/2)$, since $K = I$.

2.3 Nuclear influence on atomic transitions

If the nuclear moments differ from zero, the resulting electromagnetic fields interact with the electron shell, which is called hyperfine interaction. This causes a splitting of an electronic level with angular momentum J into $2I + 1$ sub-levels if $J \geq I$, or into $2J + 1$ sub-levels if $J < I$. These sub-levels are now described by the total angular momentum $\vec{F} = \vec{I} + \vec{J}$ (see Fig. 2.4). This effect was first theoretically interpreted by Pauli in 1924, where he already pointed out its possible application as a method to investigate the nuclear structure via atom spectroscopy [49].
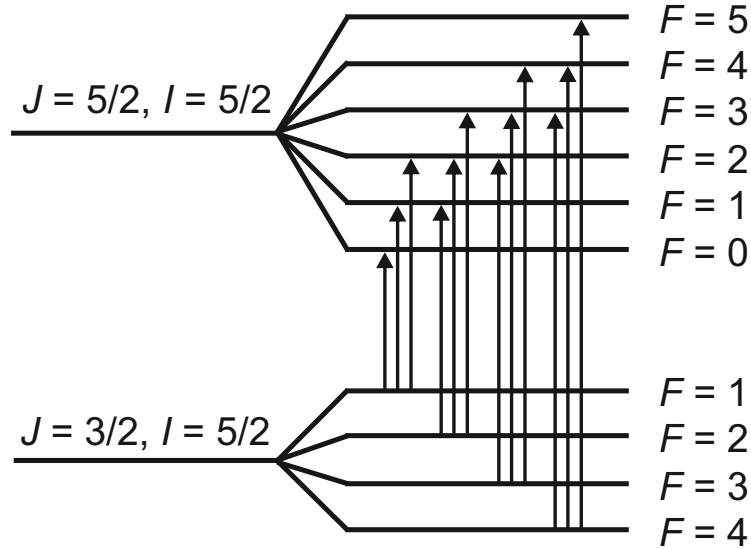
Figure 2.4: **Schematic representation of the hyperfine splitting.** The two electronic levels with angular momenta $J = 3/2$ and $J = 5/2$ split into four and six sub-levels respectively, due to their interaction with the nuclear spin $I = 5/2$. The resulting hyperfine structure of a transition between the two levels consists therefore of twelve individual transitions.

The energy shift associated with this splitting can be expressed as (see, e.g., Refs. [48; 35]):

$$\Delta E_{HFS}(JIF) = A\frac{C}{2} + B\frac{\frac{3}{4}C(C+1) - I(I+1)J(J+1)}{2I(2I-1)J(2J-1)}, \qquad (2.19)$$

with $C = F(F+1) - J(J+1) - I(I+1)$. The hyperfine constants A and B represent the coupling to the nuclear moments with:

$$A = \frac{\mu H(0)}{IJ}, B = Q_s \phi_{JJ}(0). \tag{2.20}$$

$H(0)$ is the magnetic field strength and ϕ_{JJ} the electric field gradient caused by the electrons at the place of the nucleus. Only the magnetic dipole moment μ and the electric quadrupole moment Q of the nucleus are considered, since the influences of moments with higher multipolarity are significantly smaller [50] and therefore beyond the precision of the experimental setup employed in this thesis.

Due to the high accuracy that can be achieved in microwave and laser atomic spectroscopy, it is now a well established method to determine nuclear moments based on their influence on atomic levels, called hyperfine spectroscopy. In such experiments, the hyperfine constants A and B are usually not known, but have to be inferred from the measured spectra. To this end, it is necessary to assign the observed resonances to their corresponding hyperfine transitions. It is therefore beneficial to know the expected line strength of the individual transitions. The strength S of an HFS transition between the states $|\gamma J I F\rangle$ and $|\gamma' J' I F'\rangle$ in the case of an electric dipole transition is given by:

$$S_{HFS} = |\langle \gamma J I F || \hat{P} || \gamma' J' I F' \rangle|^2 = |F, F'| \begin{Bmatrix} J & I & F \\ F' & 1 & J' \end{Bmatrix}^2 |\langle \gamma J || \hat{P} || \gamma' J' \rangle|^2,$$
$$\tag{2.21}$$

with $|F, F'| = (2F+1)(2F'+1)$, $\hat{P}$ being the dipole moment of the atom, γ, γ' being all additional quantum numbers needed to describe the states and the $\{\}$ expression being the Wigner 6j-symbol. The squared matrix element at the end represents the total line strength. This term can be neglected in the case when only the relative intensities of the components are of interest. Dividing by $(2I+1)$ gives the normalized expression [51]:

$$S = \frac{(2F+1)(2F'+1)}{2I+1} \cdot \begin{Bmatrix} J & I & F \\ F' & 1 & J' \end{Bmatrix}^2. \tag{2.22}$$

A further influence on the atomic transitions arises from the finite size and mass of the nucleus, called the isotope shift. Since the nucleus is not a point-like object, part of the electron wave function extends inside the nuclear

radius, where the field is not described by a Coulomb potential anymore. If the nucleus is assumed to be a homogeneously charged sphere with the radius r_N, the potential inside the nucleus can be modeled as [52]:

$$V(r) = \frac{Ze^2}{4\pi\epsilon_0 r_N} \left(-\frac{3}{2} + \frac{r^2}{2r_N^2} \right), 0 \leq r \leq r_N. \tag{2.23}$$

The energy shift for the electron wave function ψ_{nlm} follows then from the difference between nuclear and Coulomb potential:

$$\Delta E \approx |\psi_{nlm}(0)|^2 \int_0^{r_N} (V(r) - V_{\text{Coul}}) 4\pi r^2 \mathrm{d}r = \frac{4\pi}{10} |\psi_{nlm}(0)|^2 \frac{Ze^2}{4\pi\epsilon_0} r_N^2. \tag{2.24}$$

This lowers the binding energy of the electrons with increasing nuclear radius, causing the levels to be shifted upwards. This so called field shift is typically the dominant contribution to the overall isotope shift for heavy elements. It also causes the isomeric shift between different states of the same nucleus.

Additional to the field shift is the effect of the finite mass of the nucleus. Since the nucleus is not infinitely heavy, it moves relative to the center of mass of the atom. Taking this into account by employing a reduced mass for the electron yields the so called normal mass shift (NMS). In the case of hydrogen-like atoms this causes the electronic levels to be shifted further down with increasing nuclear mass M:

$$E_n = -\frac{1}{2} \frac{\mu_e e^4}{\hbar^2 n^2} = -\frac{1}{2} \frac{m_e e^4}{\hbar^2 n^2} \cdot \frac{M}{m_e + M} \approx E_n^0 \left(1 - \frac{m_e}{M} \right). \tag{2.25}$$

For many-electron systems the coupling between the electrons is an additional factor, causing the so called specific mass shift (SMS). Since the kinetic energy of the nucleus is about m_e/M times smaller compared to the electrons, the motion of the nucleus can be treated with perturbation theory. The total mass shift is assumed to be $\Delta E = \langle \vec{P}^2/2M \rangle$, with $\vec{P}$ being the nuclear momentum. Due to momentum conservation, the nuclear momentum has to compensate the electron momenta $\vec{P} = -\sum_i \vec{P}_i$. The mass shift then follows as:

$$\Delta E = \Delta E_n + \Delta E_s = \frac{m_e}{M} \left(\sum_i \frac{\vec{P}_i^2}{2m_e} \right) + \frac{m_e}{M} \left(\sum_{i \neq k} \frac{\vec{P}_i \cdot \vec{P}_k}{2m_e} \right). \tag{2.26}$$

The first term represents the NMS and the second the SMS. Although the NMS can be usually neglected for heavy elements ($Z > 60$), the SMS can constitute up to a few percent of the isotope shift, making it relevant in high precision calculations and experiments [53].

2.4 Energy transfer between nucleus and electron shell

A central goal of the research directed at ^{229}Th is the driven excitation of the isomeric state. Apart from the direct coupling of the nucleus to the electromagnetic field, energy can also be transferred via the electron shell. A well known process is the nuclear de-excitation via internal conversion (IC) (see, e.g., Ref. [54]). In this case, the nuclear excitation energy is transferred to a shell electron via a virtual photon, which then leads to ionization, due to the fact that most nuclear excitations are several orders of magnitude higher than the binding energy of the electron. Although this is a higher order process compared to γ-radiation, it can be the dominant decay channel, effectively suppressing γ decay.

In Ref. [55], Krutov and Fomenko discuss the de-exitation of the nucleus via radiation from the electron shell, calling the process 'electronic bridge' (EB). It has also been referred to as 'bound internal conversion' due to the similarity to IC [56; 57], except that the electron is only intermediately excited, but not ejected from the shell. The probability of this process therefore depends strongly on a resonance between the nuclear excitation and the electronic transition. A scheme of the process is shown in Fig. 2.5. The involvement of the electron shell can also open further decay channels, in the case of the isomer ^{229m}Th the electric quadrupole (E2) transition, which is not present in the direct optical decay (see, e.g., Ref. [39]).

First experimental observation of the EB mechanism was reported by Kekez et al. in 1985 [58], studying the decay of the 30.7 keV isomeric level in ^{93}Nb. The corresponding excitation scheme was first theoretically discussed by Morita in 1973 [59], introduced as 'nuclear excitation by electron transition' (NEET), and later observed experimentally by Fujioka et al. in 1984 [60]. The term *electronic bridge* has subsequently also been used to describe the excitation process.

In the case of the isomer ^{229m}Th, the nuclear excitation energy of 8.28(17) eV is comparable to electronic transitions (see Fig. 2.6). An enhancement of the nuclear excitation and de-excitation via the EB mechanism is therefore expected to play an important role, especially for systems with a dense electronic

structure. A recent experiment indicated that the isomeric lifetime in ^{229}Th$^+$, a three valence electron system, might be below $10\,\mathrm{ms}$ due to a strong EB decay channel [61].

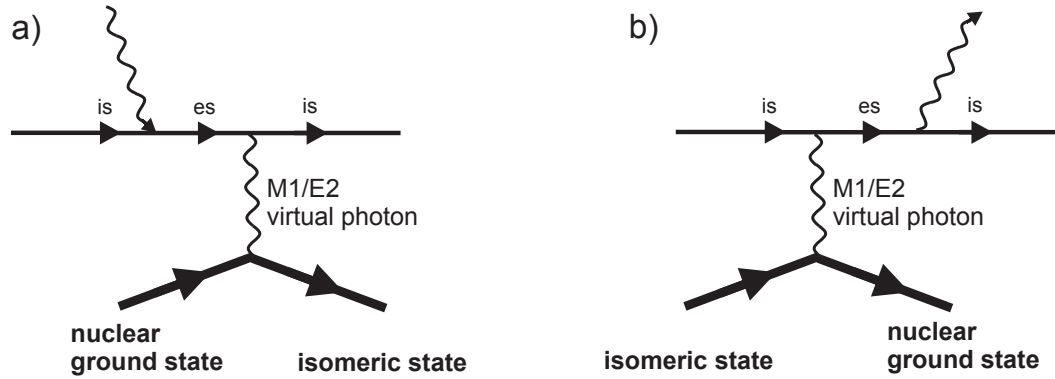Figure 2.5: **Feynman diagrams of the electronic bridge mechanism.** The state of the electron shell is depicted with a thin line and the nuclear state as bold. The process of nuclear excitation (a) and de-excitation (b) via the transition of the electron shell between its initial state (is) and an excited state (es) is shown. In the case of ^{229}Th, the nuclear and electronic states are coupled via a virtual M1 or E2 photon.
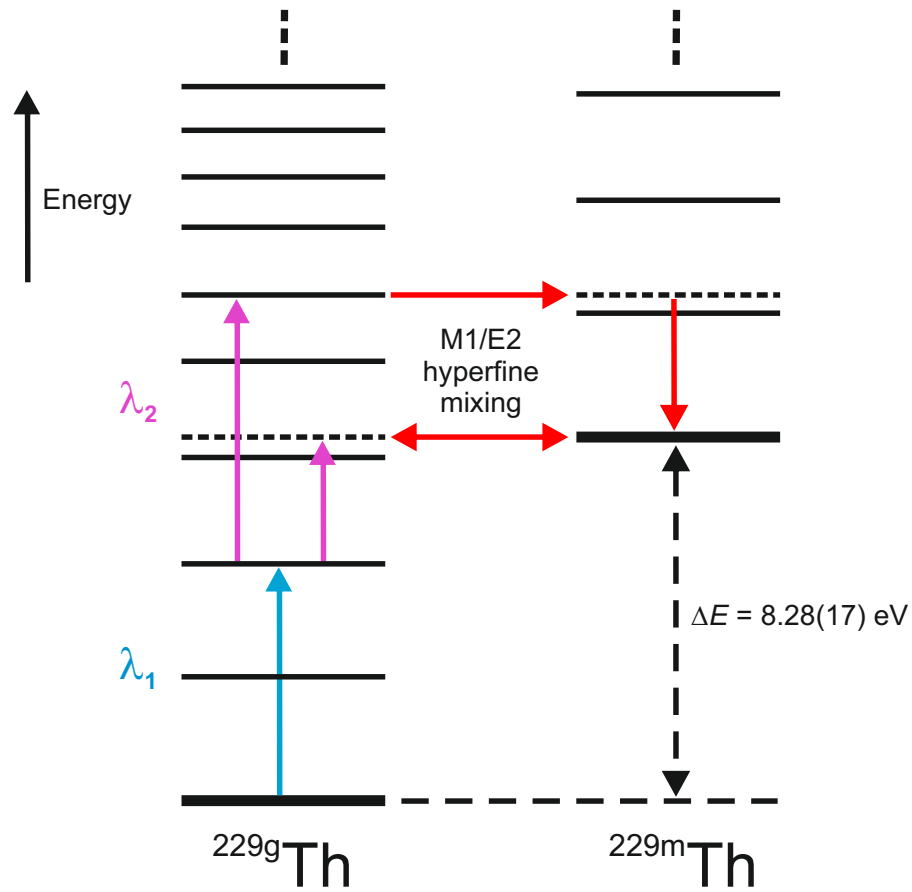
Figure 2.6: **Scheme of the electronic bridge mechanism.** The electronic level structure for both nuclear states is shown schematically. Levels in the isomeric state are treated as shifted by the nuclear excitation energy. The electron shell in the nuclear ground state is excited via two photons λ_1 and λ_2 to either a virtual (dashed line) or a real excitation state (solid line). These can in turn couple to a real or a virtual electronic state of the isomer via hyperfine mixing.

Chapter 3

Experimental setup

This chapter gives a short overview of the laser excitation and fluorescence detection setup used for hyperfine spectroscopy, as well as the ion traps and loading schemes at PTB and LMU used in this thesis.

3.1 Optical excitation and detection

The spectroscopy of the thorium hyperfine structure in the experiments within this thesis is provided by continuous wave (cw) extended cavity diode lasers (ECDLs). These lasers are available for a variety of wavelengths and typically exhibit a linewidth of $\approx 100\,\text{kHz}$ (see, e.g., Ref. [62]). To achieve a mode-hop free scanning range of several gigahertz, which is needed for the experiments, the laser drive current is changed together with the voltage of a piezo transducer, which controls the tuning of the cavity via a feed forward scheme. The resulting change in laser output power during the scanning has to be accounted for when evaluating the recorded spectra. The radiation of the lasers is delivered to the trap by single mode polarization maintaining fibers. The specific lasers and their parameters are introduced in the according chapters.

In the experiments, the successful excitation of an electronic level by a laser is recorded via detecting the fluorescence decay of the excited level using photo multiplier tubes (PMTs). These detectors are available for several spectral ranges from infrared up to vacuum ultraviolet (VUV) and can provide high gain, as well as high quantum efficiencies [63]. If possible, a decay channel is selected, that differs in wavelength from the excited transition. In this

case an optical narrowband filter can be used in front of the PMT to suppress background from laser stray light (see, e.g., Fig. 4.3). In the case of a high photon flux the PMT signals are read out using gated integrators (SRS, SR250). Single photon counting of weak signals is provided by photon counters (SRS, SR400).

3.2 Ion trap at PTB

Measurements on Th^+ and Th^{2+} ions at PTB are conducted using a radiofrequency linear Paul trap (see Fig. 3.1), which is described in detail in Ref. [64]. This trap consists of four segmented stainless steel rods with a total length of 160 mm, a rod diameter of 8 mm and a diagonal distance between the electrodes of 7 mm. The rods are segmented into three parts with a central trapping section of 20 mm length. The resonance frequency of the trap is 1.92 MHz and the rf field has a typical peak-to-peak voltage of $U_{pp} = 1700$ V, which corresponds to a trap depth of about 40 eV for Th^+ ions. The end-cap sections are on a dc potential of $+20$ V relative to the trapping section to achieve axial confinement. The radial secular frequency of the ions is about 270 kHz and the trap has a capacity to store up to $\approx 10^6$ Th^+ ions. It is housed in a stainless steel vacuum chamber under ultra-high vacuum conditions with a background pressure of 10^{-8} Pa. A turbomolecular pump evacuates the system continuously while a non-evaporative getter pump is activated every six months.

3.2.1 Ablation loading

The trap can be loaded with the isotopes ^{229}Th and ^{232}Th. The low-lying isomeric nuclear state only exists in ^{229}Th, but due to its radioactivity only an amount of up to 150 ng is permitted in the laboratory at the same time, which corresponds to an activity of 1 kBq. However, the permitted amount for the naturally occurring isotope ^{232}Th is 2.5 g due to its long half life of $\approx 10^{10}$ years, making it a good test system when the nuclear properties are not important. Ions are loaded via laser ablation from samples located between the lower electrodes of the trap (see Fig. 3.1). Ablation is achieved by using a Nd:YAG laser emitting 5 ns pulses with an energy of below 1 mJ at 1064 nm. For the isotope ^{232}Th, the sample consists of a solid thorium wire. Since ^{229}Th
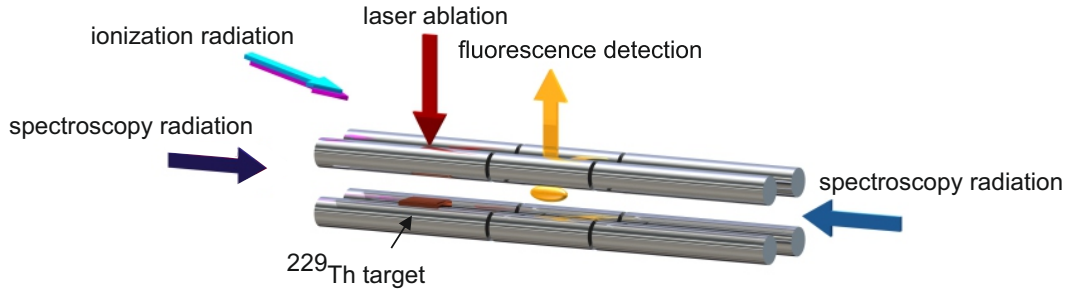
Figure 3.1:   **Schematic of the PTB ion trap.** Th$^+$ ions are loaded via laser ablation from a dried Th(NO$_3$)$_4$ solution, deposited on a tungsten wire, and cooled via an argon buffer gas at 0.1 Pa pressure. The trap has a capacity to store up to 10^6 Th$^+$ ions. Th^{2+} ions are produced via resonance enhanced three-photon ionization. Spectroscopy laser beams are applied along the trap axis. The figure is adapted from Ref. [26].

has to be produced artificially, it is only available in small quantities. Our ^{229}Th targets for laser ablation are produced by drying droplets of Th(NO$_3$)$_4$ solution on a tungsten wire, with a thorium amount per target of about 75 ng. From such a sample the ion trap can be loaded about 100 times per sample before it has to be replaced [65]. ^{229}Th and ^{232}Th are present on the dried solution target in about equal proportions, causing both isotopes to be loaded and trapped simultaneously.

3.2.2   Buffer-gas system and photodissociation

The level structures of Th$^+$ and Th^{2+} do not provide fast decaying closed transitions that could be employed for laser cooling. The ions are therefore only cooled to room temperature by collisions with an argon buffer gas (purity of 99.99999 %, Ar 7.0) at 0.1 Pa pressure, which also depopulates metastable states via collisional quenching [30]. The buffer gas is applied from a reservoir, which in turn is filled periodically from the gas bottle with the gas running through a catalytic noble gas purifier (SAES Getters, MC190-902F).

Since the vacuum system still contains small amounts of reactive contaminants after cleaning and baking, the time the ions are available for the experiment is ultimately limited by the formation of molecules with these impurities. However, it was shown that the accumulation of ThX$^+$ molecules can be

strongly suppressed via photodissociation using radiation with a wavelength below 289 nm and an intensity above $50\,\mathrm{kW/cm^2}$ [66]. To this end, the 4th harmonic radiation of a Q-switched Nd:YAG laser at 266 nm with a pulse energy of $\approx 10\,\mu\mathrm{J}$ is employed. The effective storage time rises in this case from 650 s to $5 \cdot 10^5$ s.

For a better understanding of the dissociation process, the masses of the $\mathrm{ThX^+}$ molecules present in the trap have been measured in a previous work to be between 246 and 259 amu, indicating the presence of the molecules $\mathrm{ThCH_2^+}$, $\mathrm{ThO^+}$ and $\mathrm{ThOH^+}$ [66]. The dissociation process is therefore expected to be mainly characterized by the bond-dissociation energies $DH(\mathrm{ThCH_2^+}) = 4.8\,\mathrm{eV}$ [67] and $DH(\mathrm{ThO^+}) = 9.1\,\mathrm{eV}$ [68]. The ability to dissociate $\mathrm{ThCH_2^+}$ molecules is tested by switching the 266 nm dissociation laser off and on while using $5 \cdot 10^{-3}\,\mathrm{Pa}$ of methane as buffer gas with trapped $\mathrm{Th^+}$ ions, showing a recovery of almost the full fluorescence signal (see Fig. 3.2). Based on the difference of up to 0.5 eV between photon energy and $\mathrm{ThCH_2^+}$ bond-dissociation energy in Ref. [66], it has been concluded that the dissociation has to occur at least in a two-photon process.

Theoretical estimations for the bond-dissociation energies of the corresponding $\mathrm{ThX^{2+}}$ molecules are $DH(\mathrm{ThCH_2^{2+}}) = 5.6\,\mathrm{eV}$ and $DH(\mathrm{ThO^{2+}}) \geq 7.8\,\mathrm{eV}$ [69; 70]. Irradiating trapped $\mathrm{Th^{2+}}$ ions and their molecular compounds in the ion trap, using the third harmonic generation (THG) of a pulsed titanium-sapphire (Ti:Sa) laser, does not show any dissociation process for wavelengths from 280 nm to 250 nm with intensities up to $300\,\mathrm{kW/cm^2}$ and down to 236 nm with intensities of $30\,\mathrm{kW/cm^2}$. It is therefore assumed that the photodissociation of $\mathrm{ThX^+}$ compounds benefits from enhancement, possibly due to a higher level density compared to $\mathrm{ThX^{2+}}$ compounds.

3.2.3 $\mathrm{Th^{2+}}$ production and storage

In the setup at PTB, $\mathrm{Th^{2+}}$ is not directly loaded via laser ablation. To prepare a sample of $\mathrm{Th^{2+}}$ ions, the trap is first loaded with $\mathrm{Th^+}$ ions and then doubly charged ions are generated via resonant three-photon ionization (see Fig. 3.3). A 402 nm ECDL with an output power of 20 mW, shaped into pulses with a duration of 90 ns by an acousto-optic modulator, is used to pump the $24874\,\mathrm{cm^{-1}}$ level of $\mathrm{Th^+}$ as a first excitation step.
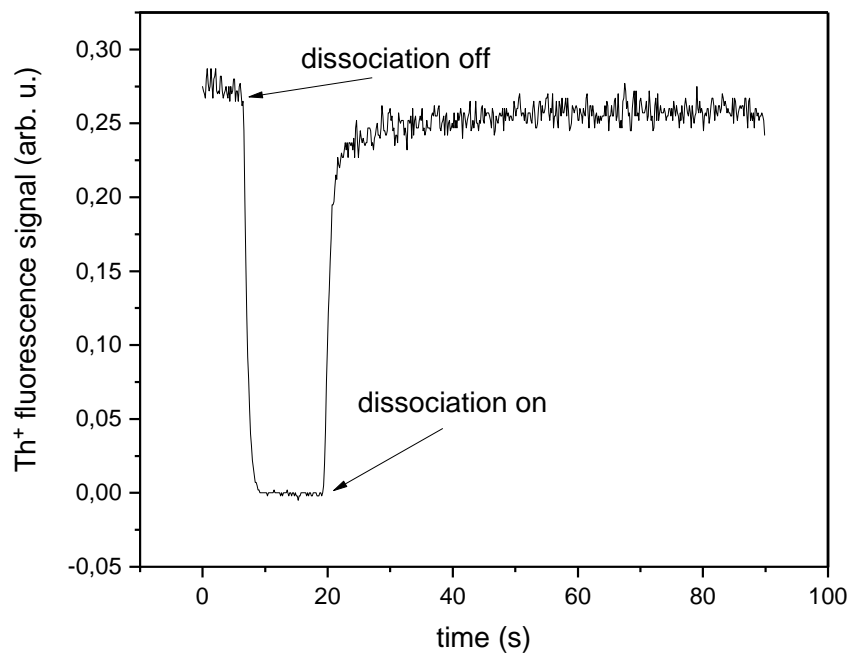
Figure 3.2: **Photodissociation of ThX$^+$ compounds in CH$_4$ buffer gas.** Th$^+$ ions are initially stored in the trap while applying the 266 nm laser radiation and using $5 \cdot 10^{-3}$ Pa of methane as buffer gas. The dissociation laser is switched off 7 s after the start of the measurement, followed by a rapid decrease in fluorescence signal due to the predominant formation of ThCH$_2^+$ molecules [67]. Switching the 266 nm laser on initiates dissociation of the molecules, visible as a reappearing fluorescence signal. The final fluorescence signal level is smaller than the initial, possibly due to further reactions to non-dissociable molecules with impurities of the buffer gas while the 266 nm laser is switched off.

The second and third excitation step photons are provided by the THG of a pulsed Ti:Sa laser (pulse duration of 10 ns, THG peak power of $\approx 1\,\text{kW}$) via the $63258\,\text{cm}^{-1}$ Th^+ state [66]. Both lasers operate at a repetition rate of 1 kHz and pulses of the Ti:Sa laser and the ECDL are synchronized and overlapped in time.
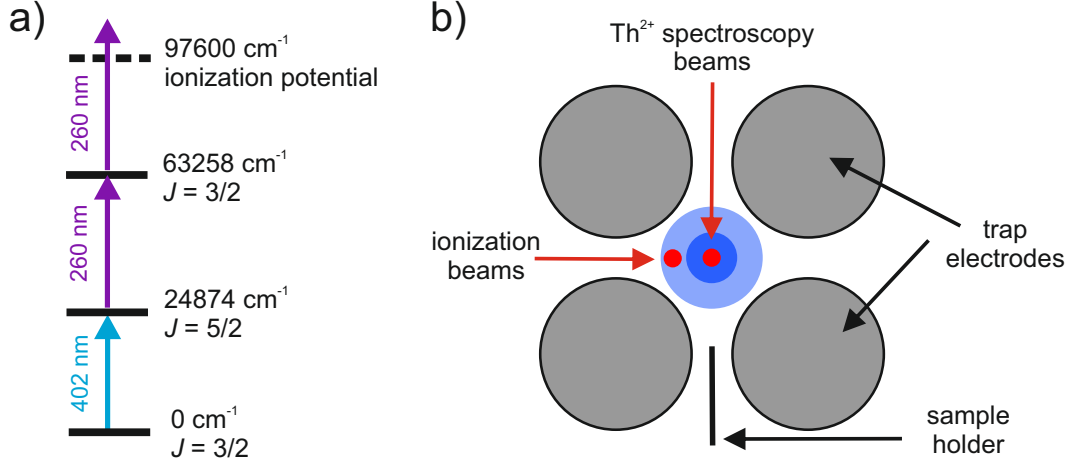

Figure 3.3: **Th^{2+} production and trapping.** a) Th^{2+} ions are produced via resonance enhanced three-photon ionization of Th^+. b) Cross-section of the ion trap, showing schematically (not to scale) the Th^{2+} ion cloud (dark blue), which is surrounded by a shell of Th^+ ions (light blue). The ionization laser beams are shifted from the trap center by 1 mm to maximize the overlap with the Th^+ ions, while the laser beams for Th^{2+} spectroscopy are adjusted to the trap center.

The larger mass-to-charge ratio of the Th^+ ions causes them to be mostly located in a shell around the Th^{2+} ions, which are stronger concentrated to the trap center, since they experience a twice deeper trap potential. The ionization laser beams are therefore shifted by about 1 mm from the trap center to maintain overlap with the Th^+ cloud also in the presence of Th^{2+} ions (see Fig. 3.3). This reduces the initially produced amount of Th^{2+} when applying the ionization beams, but enlarges the steady state amount. A stable amount of $> 10^3$ Th^{2+} ions can be reached, defined by an equilibrium of the ionization rate and losses due to chemical reactions with impurities in the buffer gas.

A cryogenic buffer-gas cleaning based on a cold finger is employed to further extend the storage time of the Th^{2+} ions. The cold finger is mounted on the

main vacuum chamber close to the ion trap and is cooled by a continuous flux of liquid nitrogen (LN_2), supplied from a 120 liter dewar. Using the cold finger over the course of four months to concentrate impurities for more efficient pumping increased the storage time of Th^+ (without dissociation) and Th^{2+} from $\tau(Th^+) = 650\,s$ and $\tau(Th^{2+}) = 350\,s$ to $\tau(Th^+) = 1000\,s$ and $\tau(Th^{2+}) = 600\,s$. During the operation of the cold finger the storage time of Th^+ and Th^{2+} ions increases additionally by $\approx 60\,\%$ up to $1600\,s$ and $1000\,s$ respectively. Together with the aforementioned continuous ionization from Th^+ to Th^{2+}, this gives an operational time for one loading of $\tau(Th^{2+}) \approx 2 \cdot 10^5\,s$, suitable for 3 days of experiments (see Fig. 3.4).
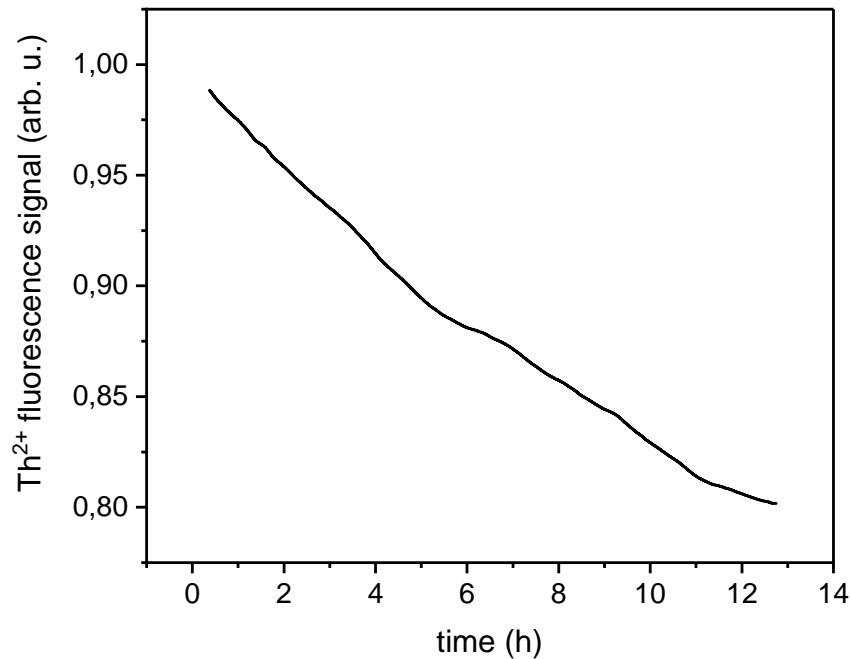

Figure 3.4: **Long term measurement of Th^{2+} fluorescence.** An operational time for Th^{2+} of $\tau \approx 2 \cdot 10^5\,s$ per loading is reached by constantly ionizing a small amount of trapped Th^+ ions and using a liquid nitrogen cold finger for cryogenic buffer-gas cleaning. Molecules with Th^+ ions are photodissociated.

3.3   Ion trap at LMU

Parts of the experiments are also performed at the Maier-Leibnitz-Laboratorium at LMU. Only a brief introduction will be given here, since the setup has already been described extensively in Refs. [24; 71].

The experimental setup uses thorium ions which are produced by the α decay of ^{233}U [72]. The reason for this is, that a fraction of about 2 % of these thorium nuclei are in the low-lying isomeric state, which is populated via the γ cascade following the ^{233}U α decay. The ^{233}U source was produced via molecular plating by the group for super heavy elements at JGU in Mainz [73]. It consists of 290 kBq of ^{233}U, which is deposited onto a titanium-sputtered silicon wafer over a circular area with a diameter of 90 mm. To allow for on-axis laser-spectroscopy experiments, the ^{233}U source has a central hole of 8 mm diameter [24] (see Fig. 3.5).
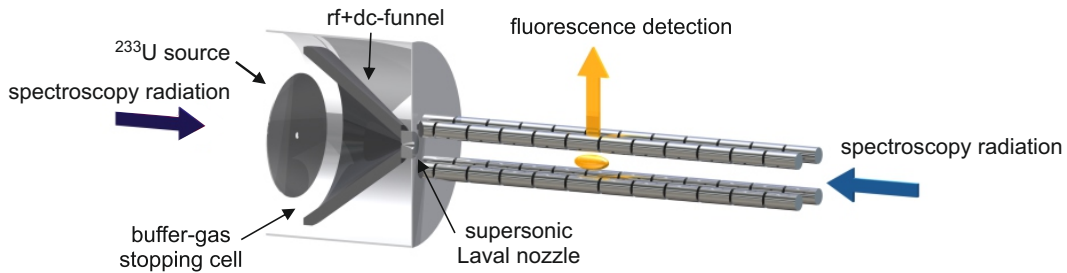

Figure 3.5:   **Schematic of the LMU ion trap.** A ^{233}U source produces ^{229}Th ions with a kinetic energy of about 84 keV. The ions are stopped in a buffer-gas cell filled with $3.2 \cdot 10^3$ Pa of helium and directed to a nozzle via an rf funnel system. The ions are then dragged by the gas through the nozzle and trapped in a segmented rf quadrupole, acting as a Paul trap. The figure is adapted from Ref. [26].

Since the thorium ions leave the uranium source with a high kinetic energy of about 84 keV, they need to be decelerated in order to be trapped. To this end, the uranium source is housed in a buffer-gas stopping cell filled with $3.2 \cdot 10^3$ Pa of helium (purity of 99.9999 %) [74], which is additionally purified by catalytic purification and an LN$_2$ cryo trap [24; 72]. Highly charged thorium ions undergo charge exchange with the buffer gas during the stopping process, producing mostly ions in the charge states 2+ and 3+. These ions, together

with the daughter products of the ^{233}U decay chain, are guided by an electric rf+dc-funnel system, consisting of 50 concentric ring electrodes, towards a Laval extraction nozzle with a throat diameter of 0.6 mm. The Laval nozzle forms a supersonic gas jet, which drags the ions into a 12-fold segmented rf quadrupole. This quadrupole is operated as an ion trap by applying dc voltages to selected segments. The trapping region is continuously evacuated by a turbo molecular pump, resulting in a He pressure of about 0.1 Pa.

3.3.1   Ion loading

About 10^5 ^{229}Th α-recoil ions are leaving the ^{233}U source per second. The charge states 2+ and 3+ have an extraction efficiency of $\approx 5\,\%$ and $\approx 10\,\%$, respectively. The extraction efficiency is defined as the ratio of the amount of ions of a specific charge state which enters the rf quadrupole and the total amount of ions leaving the recoil source. This means that more than 10^4 ^{229}Th ions enter the rf quadrupole per second. The trap is therefore continuously loaded with ^{229}Th ions, but only about 10^3 ^{229}Th^{2+} ions are actually trapped due to the selected operating parameters of the trap.

Due to charge exchange, the ^{229}Th^{3+} ions are reduced to ^{229}Th^{2+} over time. This is visible in an increase in the Th^{2+} amount. Depending on the amount of impurities in the vacuum chamber (the main source for charge exchange) the maximum number of Th^{2+} ions is reached 5 to 30 s after applying the dc trapping voltages. Afterward, the Th^{2+} amount decreases due to the accumulation of molecular compounds in the trap formed via chemical reactions with impurities. Since the system is continuously pumped via a turbo molecular pump, the amount of impurities decreases slowly over time. This is visible in the measurements as a slower charge exchange and a slower accumulation of molecular compounds (see Fig. 3.6). Each experimental cycle therefore starts with a loading time of up to 20 s, followed by 60 s of data acquisition. Afterward, the trap is emptied by setting the dc trapping potential to 0 V for one second before a new cycle starts.
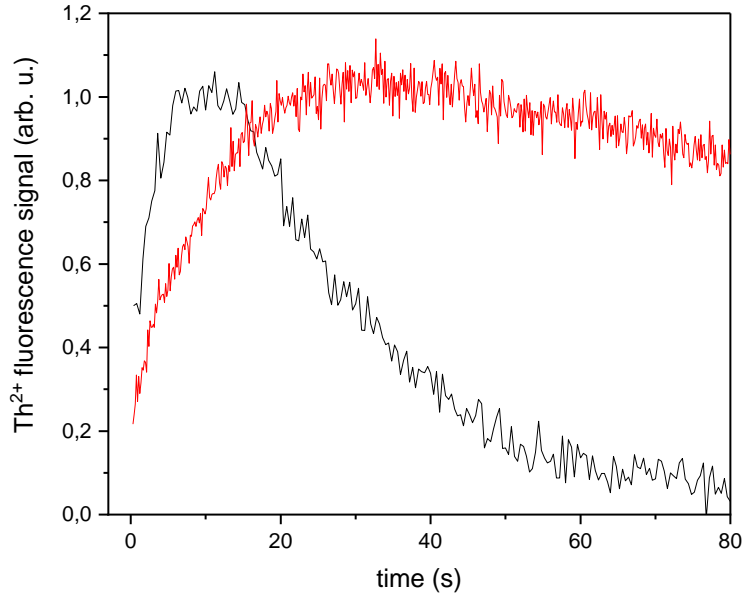
Figure 3.6:   **Th^{2+} ion amount in the LMU trap over time.** The Th^{2+} fluorescence signal is acquired while continuously loading the trap. The black curve shows a measurement performed two days after evacuating and baking the chamber, the red curve shows a measurement performed 24 days later.

3.3.2   Other trapped nuclides

The recoil source also contains ^{232}U with a fraction of below 10^{-6}. Due to its short lifetime of about 70 years and fast decaying daughter products [75], even a small relative amount can lead to a significant additional activity of the recoil source. Daughter isotopes of ^{233}U and ^{232}U were removed via ion-exchange chromatography before deposition (25 months prior to the experiments).

However, due to ingrowth over time these isotopes have to be expected to enter the ion trap. Additionally, ions of uranium are emitted via recoil sputtering, i.e. energy transfer from recoil ions to surrounding uranium atoms of the source. Expected isotopes in the trap, together with an estimation of their relative abundance compared to ^{229}Th [26], are listed in Tab. 3.1.

Table 3.1: **Relative extraction of isotopes from the ^{233}U source.** The relative amounts of ions leaving the ^{233}U source via α decay and recoil sputtering are listed. The extraction ratios are estimated upper limits on the number of extracted ions relative to the number of ^{229}Th [26].

Isotope	Extraction (rel. to Th-229)	Isotope	Extraction (rel. to Th-229)
Th-229	1	Th-228 decay chain	$7 \cdot 10^{-4}$
U-233	≈ 1	Pu-240	$4 \cdot 10^{-4}$
U-234	$2 \cdot 10^{-2}$	Th-229 decay chain	$2 \cdot 10^{-4}$
U-235	$1 \cdot 10^{-2}$	Ac-227	$1 \cdot 10^{-4}$
U-236	$1 \cdot 10^{-2}$	Pa-231	$2 \cdot 10^{-5}$
Th-230	$7 \cdot 10^{-3}$	Ac-227 decay chain	$6 \cdot 10^{-6}$
Pu-239	$2 \cdot 10^{-3}$	Pu-238	$4 \cdot 10^{-6}$
Th-228	$1 \cdot 10^{-3}$	U-232	$6 \cdot 10^{-7}$

Chapter 4

Th$^+$ measurements

The hyperfine structures of several transitions in ^{229}Th$^+$ have already been investigated previously in Refs. [31; 76; 77], in particular the transition from the electronic ground state $0_{3/2}$ (denoted in cm^{-1} with the angular momentum J as subscript) to the excited state $24874_{5/2}$, including its isotope shift compared to ^{232}Th$^+$ [31]. In this case, the excitation of this transition was driven by laser radiation at a wavelength of 402 nm, provided by an ECDL. A saturated absorption spectroscopy technique has been used to determine the hyperfine structure. Non-linear spectroscopy signals of the hyperfine structure of ^{229}Th$^+$ are depicted in Fig. 4.1. The employed spectroscopy technique is also used in this thesis and is therefore briefly introduced in the following, based on Ref. [78].

4.1 Doppler-free spectroscopy

If the ions were at rest, the HFS components would show a linewidth of $\gamma_s = \gamma(1 + S_0)^{1/2}$, where γ is the natural linewidth of the transition and S_0 is the saturation parameter, which depends on the applied laser intensity. However, if the ions are only cooled by buffer gas to room temperature, the spectroscopic features of the HFS components exhibit a Doppler-broadening of:

$$\Delta f_{FWHM} = \sqrt{\frac{8ln(2)k_bT}{mc^2}}f_0, \tag{4.1}$$

where k_b denotes the Boltzmann constant, T the ion temperature, m the ion mass and c the speed of light. In the case of the $0_{3/2} \rightarrow 24874_{5/2}$ transition

in Th$^+$ this amounts to $\Delta f_{FWHM} \approx 600\,\text{MHz}$ for $T = 300\,\text{K}$, which is on the same order as the hyperfine splitting [31]. A spectroscopy technique that obtains Doppler-free resonances is therefore necessary to resolve the hyperfine structure.
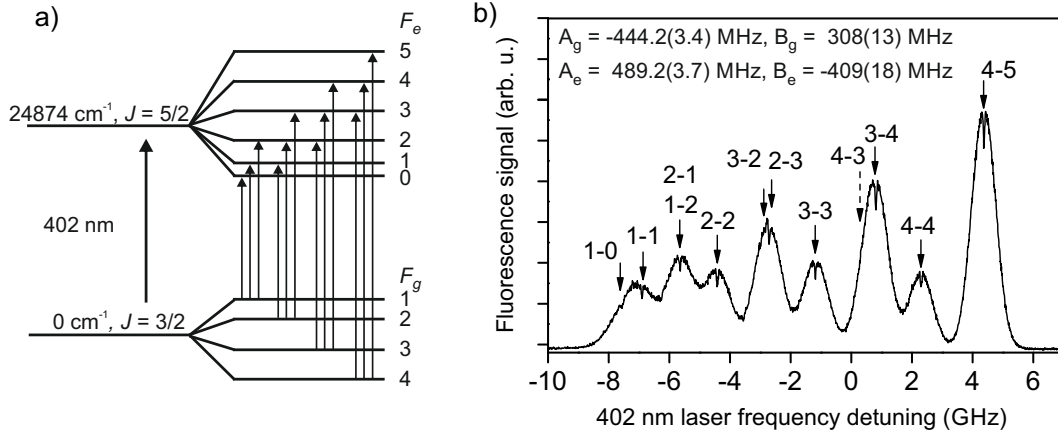

Figure 4.1: **Hyperfine structure of the $0_{3/2} \rightarrow 24874_{5/2}$ transition of ^{229}Th$^+$.** a) Level scheme showing the individual hyperfine transitions. b) HFS recorded using saturated absorption spectroscopy by retro-reflecting the 402 nm excitation laser, taken from Ref. [31]. The individual hyperfine transitions are labeled by their $F_g \rightarrow F_e$ quantum numbers. The transition $4 \rightarrow 3$ was not observed. Its predicted position is marked with a dotted arrow. The hyperfine constants are shown with subscript 'g' for the ground state and 'e' for the excited state.

4.1.1   Saturated absorption spectroscopy

Doppler-free resonances can be achieved by retro-reflecting the excitation laser beam through the ion trap. For the laser frequency f, the two beams create Bennet holes in the ground state population velocity distribution at $v_z = (2\pi(f - f_0))/k$ and $v_z = -(2\pi(f - f_0))/k$, with v_z being the ion velocity along the z-axis of the trap, f_0 being the resonance frequency of the transition and k being the absolute value of the laser radiation wave vector. The width of the Bennet holes is determined by γ_s and the laser linewidth γ_l. Usually γ_l can be neglected, since in most cases $\gamma_l \ll \gamma_s$. If $f = f_0$, both beams are

interacting with the same velocity class of ions $v_z = 0$, i.e. ions which are moving practically perpendicular to the beams. In this case the two Bennet holes overlap, causing a narrow decrease in the fluorescence signal, the so called Lamb dip [79].

In the experimental apparatus employed in this thesis, the full width at half maximum (FWHM) of this dip is not only given by the linewidth γ_s, but is further broadened by mechanisms like the transit time effect and frequency modulation from micromotion [80]. Nevertheless, the FWHM of this dip is still about one order of magnitude smaller than the Doppler-broadened linewidth [31] (see Fig. 4.1). The Lamb dip enables therefore a more precise determination of the central frequency for each transition of the HFS.

However, this spectroscopy technique is not guaranteed to resolve the HFS of isomeric ions loaded from a ^{233}U recoil source, since only about 2% of the trapped ions will be in the isomeric state. The isomeric HFS might thus be covered by the signal from ions in the nuclear ground state. A two-step excitation spectroscopy scheme is therefore employed as well [81; 76].

4.1.2 Two-step excitation

In this type of excitation scheme the ions are first excited via one laser from the initial state (g) to an intermediate state (i). Ions are only excited by this first excitation step laser if the following resonance condition is fulfilled: $f_1 - k_1 v_z/2\pi = f_{gi}$. The frequency of the laser is f_1 and the transition frequency is f_{gi}. The velocity spread of ions in the intermediate state is therefore not Doppler-broadened anymore, but mainly determined by γ_s. These ions are then probed by a second laser via excitation to a higher state (e), which is detected via fluorescence decay (see, e.g., Fig. 4.3b). The resonance condition for the second step is $\pm k_2 v_z/2\pi = f_2 - f_{ie}$, with the laser frequency f_2 and the transition frequency f_{ie}. The sign depends on the configuration of the two beams, $+k_2 v/2\pi$ corresponds to co- and $-k_2 v/2\pi$ to counter-propagating beams (see Fig. 4.2). Assuming that the ions do not change their velocity in the intermediate state, the two resonance conditions can be combined to:

$$f_2 = \pm \frac{k_2}{k_1}(f_1 - f_{gi}) + f_{ie}. \tag{4.2}$$

For the selected two-step excitations in this thesis, the ratio (k_2/k_1) only changes on the order of 10^{-5} and is therefore approximated as constant. It follows from Eq. 4.2, that if the frequency of the first step excitation laser f_1 is shifted by Δf_1, the resonance frequency of the second step will shift by $\Delta f_2 = \pm \Delta f_1 \cdot k_2/k_1$. However, the observed interval $(f_2 - f_2')$ for two different second step transitions f_{ie} and f_{ie}' is independent of f_1. This is also true for two different first step transitions f_{gi} and f_{gi}'. The amplitude of an observed resonance is given by the fraction of ions which interacts with the first step laser radiation, determined by $(f_1 - f_{gi})$, and the product of Ω_{gi}^2 and Ω_{ie}^2, where Ω is the Rabi frequency of the respective transition (see, e.g., Ref. [81]).
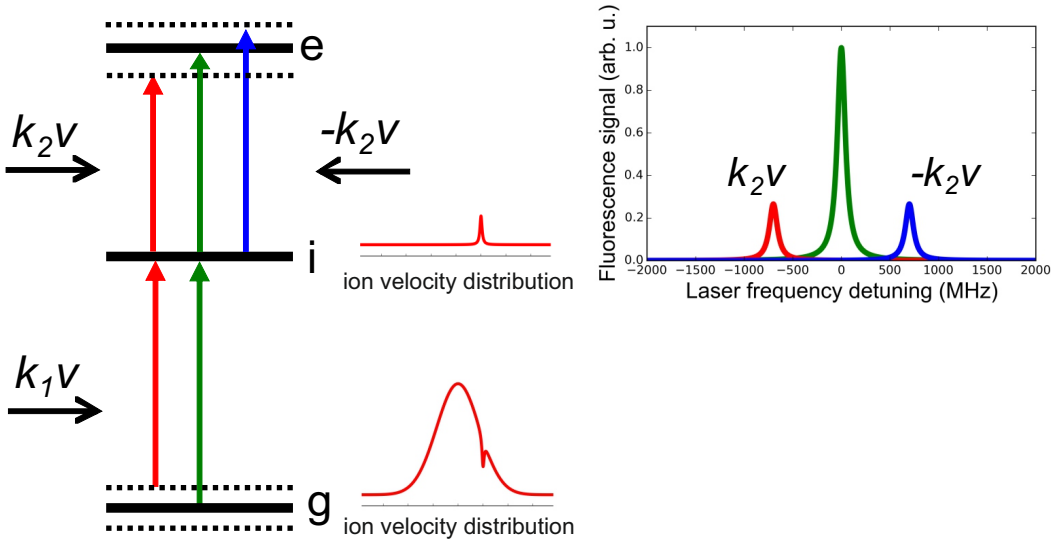

Figure 4.2: **Schematic representation of a two-step excitation.** Ions in the ground state (g) exhibit a thermal velocity distribution along the trap axis. Only ions with a certain velocity v are in resonance with the first excitation step laser and get excited to the intermediate level (i). Excitation from the intermediate level to the higher excited level (e) by scanning the second excitation step laser shows therefore a narrow fluorescence line. The resonance frequency of the second laser, as well as the resonance amplitude are dependent on the frequency of the first laser and the beam alignment (co- or counter-propagating).

4.2 Hyperfine structure of the 49960 cm⁻¹ level

For the two-step excitation of ^{229}Th$^+$ the transition $0_{3/2} \rightarrow 24874_{5/2} \rightarrow 49960_{7/2}$ is selected (see Fig. 4.3). Two advantages of this scheme are that the HFS constants for the lower two levels are already known [31] and that the spectroscopy lasers at 402 nm and 398.6 nm are available from a previous measurement of this transition in ^{232}Th$^+$ [30]. Furthermore, the upper level exhibits decay channels at wavelengths between 300 nm and 390 nm, which gives the opportunity for background free detection using a PMT (Hamamatsu, R7459) with a 390 nm short pass interference filter. The two laser beams are overlapped and aligned in a counter-propagating configuration along the trap axis.
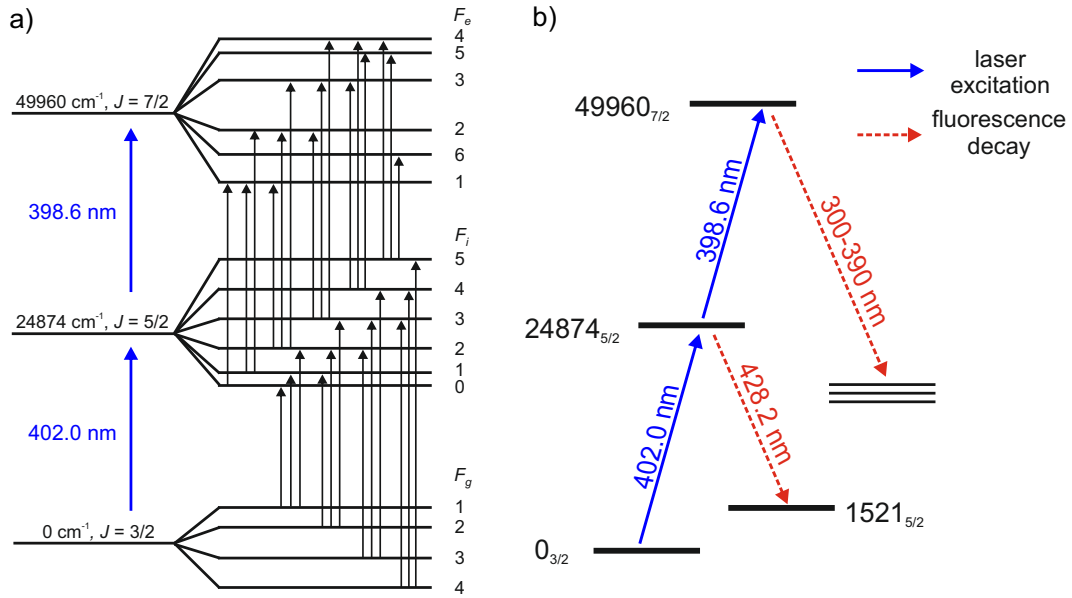

Figure 4.3:   **Two-step excitation scheme for Th$^+$.** a) Level scheme of the $0_{3/2} \rightarrow 24874_{5/2} \rightarrow 49960_{7/2}$ transition showing the individual hyperfine components. Th$^+$ ions are excited from the ground state to the 24874 cm⁻¹ level using a 402 nm laser and then further excited to the 49960 cm⁻¹ level by a laser at 398.6 nm to achieve Doppler-free resonances. The two-step HFS consists of 32 individual hyperfine transitions $F_g \rightarrow F_i \rightarrow F_e$. b) Simplified excitation scheme showing the decay channels selected for fluorescence detection.

To measure the hyperfine splitting constants of the $49960_{7/2}$ level, two-step hyperfine spectra are recorded by setting the 402 nm laser to 45 selected

frequencies within the Doppler-broadened HFS of the $0_{3/2} \rightarrow 24874_{5/2}$ line. The frequency of the 402 nm laser is stabilized to a Fizeau wavelength meter (Angstrom HighFinesse WS7) via a computer based locking scheme. The wavelength meter is periodically calibrated using an ECDL at 780 nm, which is locked to the $^2S_{1/2}$ F $= 3 \rightarrow {}^2P_{3/2}$ F $= 4$ line of ^{85}Rb in a vapor cell by the modulation transfer spectroscopy technique (see, e.g., Ref. [82]). By this method an absolute instability of the wavelength meter below 5 MHz is achieved. For each frequency of the first-step transition, the second-step laser is continuously scanned over a range of 3 GHz. The tuning is monitored by a confocal cavity, which is placed in a temperature stabilized vacuum chamber.

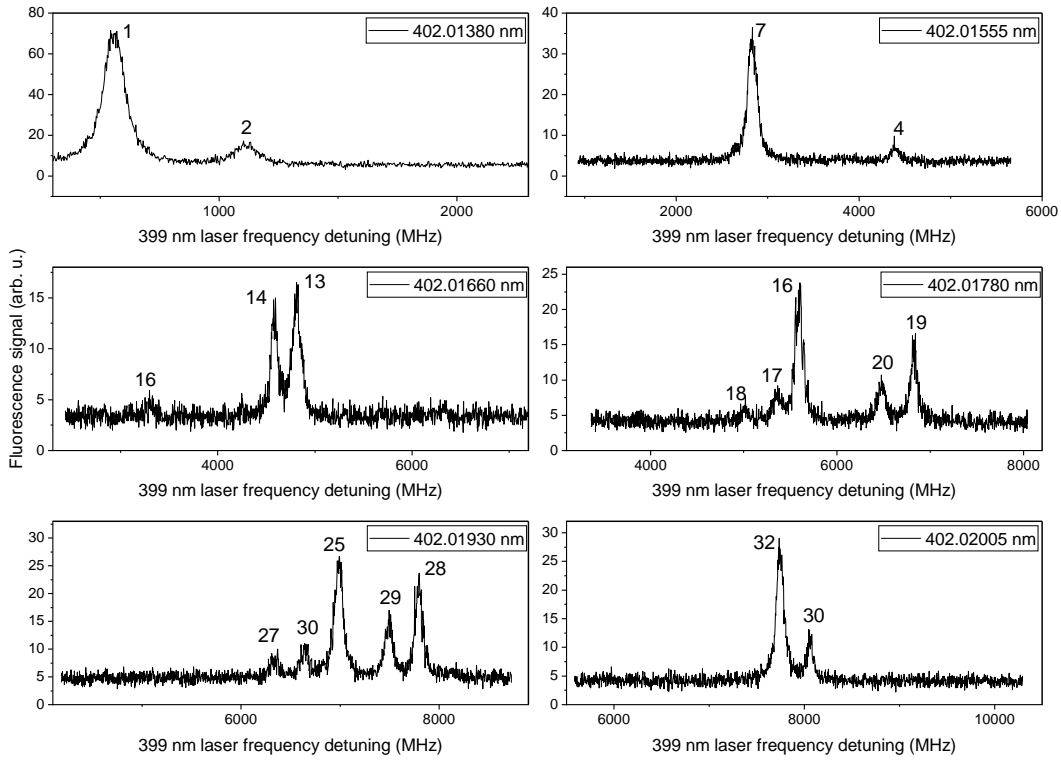Figure 4.4: **Selected fluorescence spectra of the** $0_{3/2} \rightarrow 24874_{5/2} \rightarrow 49960_{7/2}$ **two-step transition.** The spectra are recorded by stabilizing the 402 nm laser to a selected wavelength, given in the top right corner, and scanning the 398.6 nm laser over a range of 3 GHz. The observed resonances are labeled with numbers 1 to 32 and the corresponding hyperfine transitions are given in Tab. 4.1.

Table 4.1:   **Labeling of the** $0_{3/2} \rightarrow 24874_{5/2} \rightarrow 49960_{7/2}$ **two-step excitation resonances.** The detected resonances are labeled with numbers 1 to 32 and are listed with the total angular momenta of the electronic states $F_g \rightarrow F_i \rightarrow F_e$ involved in the excitation (see Fig. 4.3).

Label	$F_g \rightarrow F_i \rightarrow F_e$	Label	$F_g \rightarrow F_i \rightarrow F_e$	Label	$F_g \rightarrow F_i \rightarrow F_e$
1	$4 \rightarrow 5 \rightarrow 6$	12	$4 \rightarrow 3 \rightarrow 2$	23	$2 \rightarrow 2 \rightarrow 2$
2	$4 \rightarrow 5 \rightarrow 5$	13	$3 \rightarrow 3 \rightarrow 4$	24	$2 \rightarrow 2 \rightarrow 1$
3	$4 \rightarrow 5 \rightarrow 4$	14	$3 \rightarrow 3 \rightarrow 3$	25	$1 \rightarrow 2 \rightarrow 3$
4	$4 \rightarrow 4 \rightarrow 5$	15	$3 \rightarrow 3 \rightarrow 2$	26	$1 \rightarrow 2 \rightarrow 2$
5	$4 \rightarrow 4 \rightarrow 4$	16	$2 \rightarrow 3 \rightarrow 4$	27	$1 \rightarrow 2 \rightarrow 1$
6	$4 \rightarrow 4 \rightarrow 3$	17	$2 \rightarrow 3 \rightarrow 3$	28	$2 \rightarrow 1 \rightarrow 2$
7	$3 \rightarrow 4 \rightarrow 5$	18	$2 \rightarrow 3 \rightarrow 2$	29	$2 \rightarrow 1 \rightarrow 1$
8	$3 \rightarrow 4 \rightarrow 4$	19	$3 \rightarrow 2 \rightarrow 3$	30	$1 \rightarrow 1 \rightarrow 2$
9	$3 \rightarrow 4 \rightarrow 3$	20	$3 \rightarrow 2 \rightarrow 2$	31	$1 \rightarrow 1 \rightarrow 1$
10	$4 \rightarrow 3 \rightarrow 4$	21	$3 \rightarrow 2 \rightarrow 1$	32	$1 \rightarrow 0 \rightarrow 1$
11	$4 \rightarrow 3 \rightarrow 3$	22	$2 \rightarrow 2 \rightarrow 3$		

Typical recordings of the two-step excitation are depicted in Fig. 4.4. Since the transitions of the first step are Doppler-broadened, more than one hyperfine transition is usually excited by the 402 nm laser at a certain frequency. A single scan is therefore insufficient to assign the observed resonances to certain first-step or second-step transitions. However, it is possible to identify the same resonance for each of the first-step frequencies, since its frequency in the second-step spectrum will shift by $\Delta f_2 = -\Delta f_1 \cdot k_2/k_1$, when the first-step laser is shifted by Δf_1, as stated above. In this way 32 individual resonances are identified, which corresponds to the predicted number (see Fig. 4.3a).

4.2.1   Identification of hyperfine transitions

For each of the 45 two-step excitation spectra, the frequency positions and amplitudes of all observed resonances are noted, using a multi-peak fit function [83]. The amplitudes are corrected concerning variations of the amount of ions for the individual scans and changes of the laser power. Since the employed 398.6 nm ECDL also shows a non-linear frequency scanning, the frequency

axis for each measurement is adjusted using the transmission peaks of the monitoring cavity. The resulting uncertainty for the position of each resonance is between 5 and 30 MHz.

As a first evaluation step, the resonances are assigned to their corresponding first-step hyperfine transitions $F_g \rightarrow F_i$. To this end, the amplitude for each resonance in each measurement is plotted as a function of the first-step laser frequency. Fitting Gaussian functions to the data points results in 32 curves, from which selected curves are depicted in Fig. 4.5 and Fig. 4.6. The center position of each curve corresponds to the respective first-step hyperfine transition frequency, which were determined in Ref. [31]. Although the center position of each curve has an uncertainty of about 150 MHz, limited by the absolute accuracy of the wavelength meter of about 100 MHz and the fitting uncertainty for the amplitudes of the two-step resonances, it is possible to assign a first-step transition $F_g \rightarrow F_i$ to all 32 curves (see Fig. 4.5).

Up to three two-step resonances belong to the same first excitation step (see Fig. 4.3). By calculating the theoretical relative amplitudes of the second step using Eq. 2.22, it is possible to also assign the corresponding hyperfine states F_e of the $49960_{7/2}$ level to the transitions (see Fig. 4.6 and Tab. 4.1).

4.2.2 Hyperfine constants of the $49960\,\mathrm{cm^{-1}}$ level

Although the two-step resonances are shifting in frequency with respect to the 402 nm laser frequency, the relative intervals between the resonances only depend on the hyperfine splitting of the three involved levels and the ratio k_2/k_1, which can be assumed as constant. These intervals can therefore be used to recalculate the hyperfine constants A and B for each level based on Eqs. 2.19 and 4.2. Only few of the 32 resonances are visible in every individual measurement, but it is possible to determine the frequency intervals between all resonances, as long as at least one is visible in two subsequent measurements when shifting the first excitation step laser frequency.

The hyperfine constants of the ground state $0_{3/2}$ and the $24874_{5/2}$ level have already been measured previously in Refs. [31; 76] (see Fig. 4.1). The A and the B constant of the $49960_{7/2}$ level are determined by fitting the measured two-step hyperfine structure intervals using Eqs. 2.19 and 4.2 and a gradient-descent algorithm (see, e.g., Ref. [84]). The validity of a result produced by the
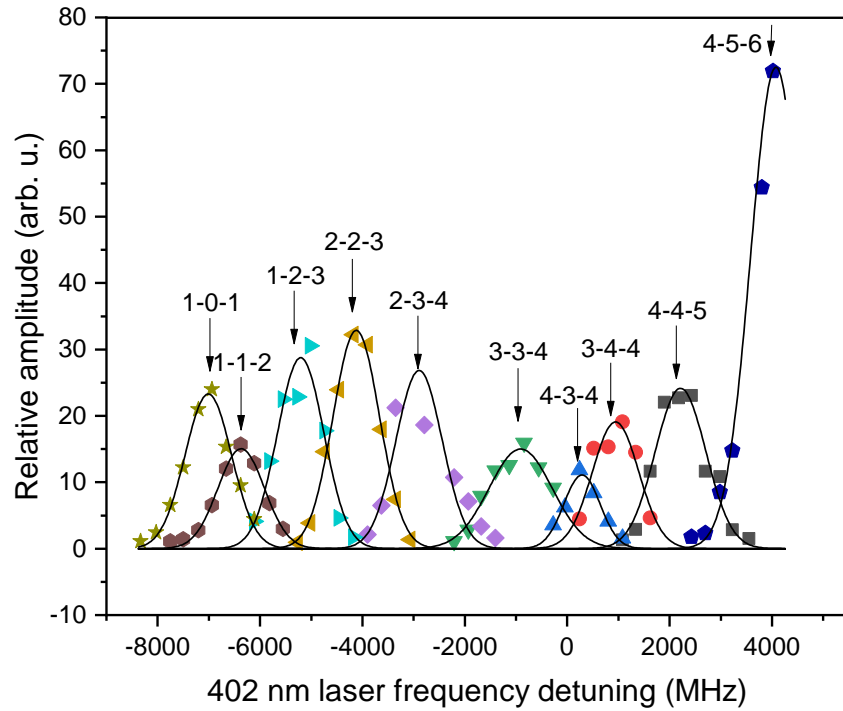
Figure 4.5: **Identification of first excitation step transitions.** For 10 of the 32 two-step resonances, the amplitude measured in each scan is plotted as a function of the 402 nm laser frequency of that scan. The points lie on Gaussian functions (shown with best fit), which are centered on the respective first-step resonance (see Fig. 4.1). The shown transitions are labeled by their respective F quantum numbers of the involved states $F_g \rightarrow F_i \rightarrow F_e$.
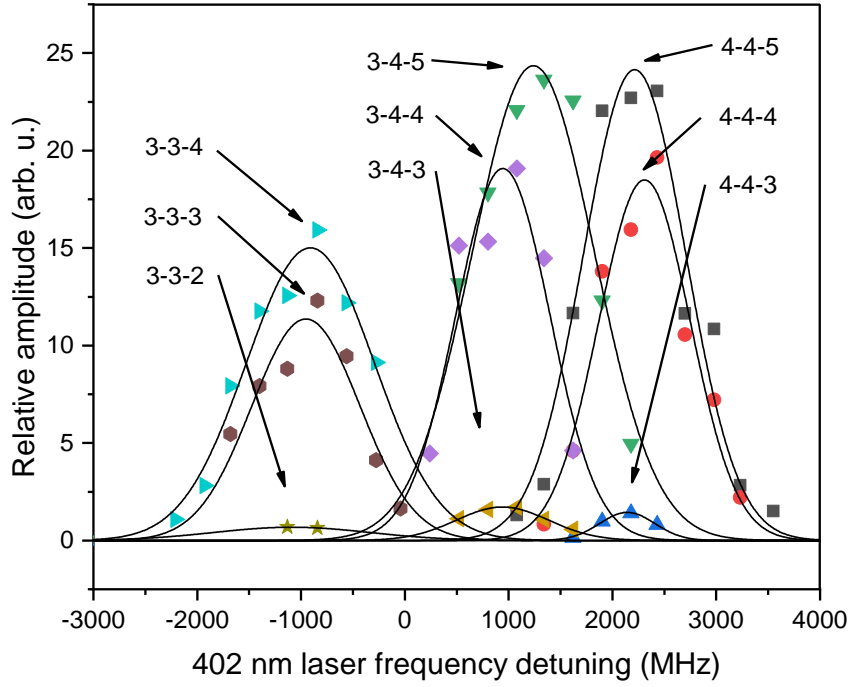
Figure 4.6: **Identification of second excitation step transitions.** Three groups of resonances, each belonging to one first-step transition $F_g \rightarrow F_i$, are depicted. Data points are plotted in the same way as in Fig. 4.5. The assignment of the respective state F_e inside one group is based on their relative amplitudes, compared to the theoretical rel. amplitudes from Eq. 2.22. Differences in the center frequencies of curves of the same group arise due to the limited absolute accuracy of the wavelength meter of about 100 MHz and the fitting uncertainty for the amplitudes of the two-step resonances.

algorithm is checked by comparing the calculated assignment of resonances to hyperfine transitions with the result obtained in Sec. 4.2.1.

To account for the uncertainties of the hyperfine constants of the levels $0_{3/2}$ and $24874_{5/2}$, the fitting algorithm is executed repeatedly with randomized values for these constants based on their 1σ-uncertainty and a Gaussian distribution. In the same manner, the measurement uncertainties of the frequency intervals are taken into account. For each initial data set, the algorithm calculates the A and the B constant of the $49960_{7/2}$ level, determined by the minimal mean squared error of the differences between the calculated and measured intervals. This minimal error also defines the fit quality. The final results for the hyperfine constants (see Tab. 4.2) are calculated as the mean values of the individual fitting results weighted by their respective fit quality. Selected two-step measurements are combined in Fig. 4.7 to create a spectrum as it would appear for the second-step transition $24874_{5/2} \rightarrow 49960_{7/2}$, if the $24874_{5/2}$ level would be homogeneously populated without Doppler-broadening. A theoretical curve based on the determined HFS constants is depicted to give an impression of the overall fit quality.

Table 4.2: **Hyperfine splitting constants of the** $49960_{7/2}$ **level in** ^{229}**Th**$^+$ **obtained via spectroscopy of the two-step transition** $0_{3/2} \rightarrow 24874_{5/2} \rightarrow$ $49960_{7/2}$.

Level (cm^{-1})	A (MHz)	B (MHz)
49960	-7.9(3.5)	-1107(39)

Additionally to the HFS constants of the $49960_{7/2}$ level, the isotope shift of the $24874_{5/2} \rightarrow 49960_{7/2}$ transition between the isotopes ^{229}Th and ^{232}Th is measured. To this end, the transition frequency in ^{232}Th$^+$ is measured using the Fizeau wavelength meter by stabilizing the 402 nm laser to the center of the $0_{3/2} \rightarrow 24874_{5/2}$ transition and scanning the 398.6 nm laser over the resonance. The center of the second-step transition is measured to be 398.6192(1) nm. The line center of the ^{229}Th HFS is determined by fitting the measured two-step spectra with fixed hyperfine constants, while leaving the line center frequency as a free parameter. With this analysis, the isotope shift is determined as 16.9(3) GHz.
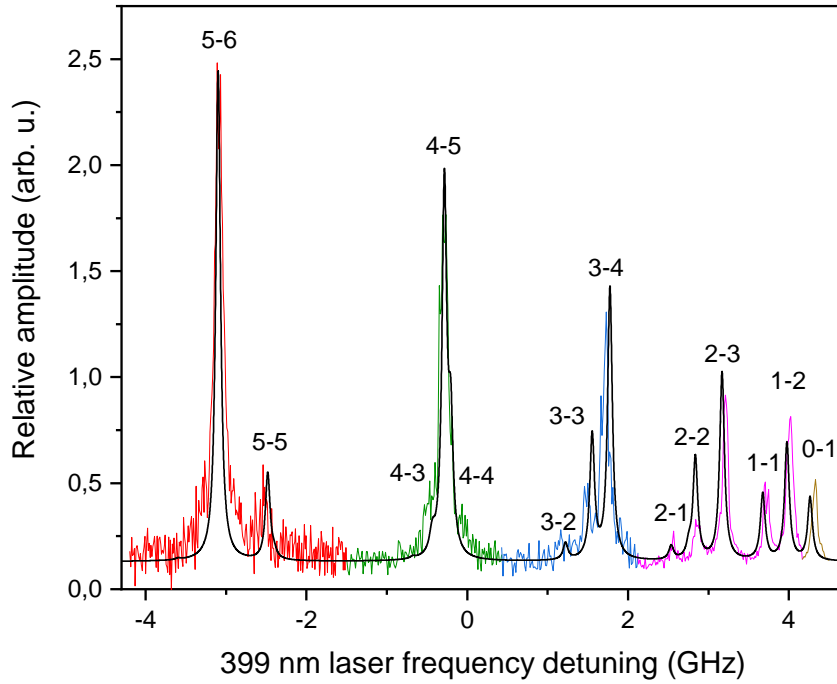
Figure 4.7: **Reconstructed HFS of the** $24874_{5/2} \rightarrow 49960_{7/2}$ **transition.**
Selected two-step measurements (distinguished by color) are combined to create a spectrum as it would appear for the $24874_{5/2} \rightarrow 49960_{7/2}$ transition, if all sub-levels of the $24874_{5/2}$ level would be homogeneously populated without Doppler-broadening. The components are labeled with their respective $F \rightarrow F'$ transitions and a theoretical curve based on the determined hyperfine constants of the $49960_{7/2}$ level is shown. The transition $5 \rightarrow 4$ is not observed.

4.3   Measurements using the recoil source at LMU

Measurements of the $0_{3/2} \rightarrow 24874_{5/2}$ transition using the α-recoil loaded ion trap at LMU unfortunately show an average ion number of only $\leq 100\,\mathrm{Th}^+$ ions in the trap. This number is estimated to be too small to achieve a suitable signal-to-noise ratio (SNR) to resolve the isomeric signal with the two-step excitation during the available measurement time of three weeks. Measurements of the single-step excitation of the $0_{3/2} \rightarrow 24874_{5/2}$ transition are therefore performed using linear spectroscopy to search for isomer signals outside the $^{229\mathrm{g}}\mathrm{Th}^+$ hyperfine structure. These signals would be visible in the case of a large isomeric shift. To achieve background-free signals, the excitation of the $24874_{5/2}$ level is recorded by detecting the fluorescence decay to the $1521_{5/2}$ level at $428.2\,\mathrm{nm}$ using a bandpass filter with a transmission range of $450 \pm 35\,\mathrm{nm}$ (see Fig. 4.3).

The measurements show deformations of the 3-4 and 4-5 hyperfine components (see Fig. 4.1), as well as eight additional resonances on the high frequency side (see Fig. 4.8). However, since these resonances are of similar amplitude as the $^{229\mathrm{g}}\mathrm{Th}^+$ HFS, they can not originate from the isomeric state.

Apart from thorium in its 2+ and 3+ charge states, the most abundant ions in the trap are $^{233}\mathrm{U}^+$ and $^{233}\mathrm{U}^{2+}$ (see Fig. 4.9). Since the level structure of uranium in several charge states has been extensively investigated (see, e.g., Ref. [85]), it is assumed that the additional resonances arise from a transition between known levels of one of these ions. The most probable candidate is the excitation of the $289_{11/2} \rightarrow 25164_{13/2}$ transition in $^{233}\mathrm{U}^+$. This is the only transition that fits the criteria of having an initial state that can be populated via collisions with the buffer gas and having a fluorescence decay of the upper level inside the spectral window of the detection ($25164_{13/2} \rightarrow 1749.123_{13/2}$, $\lambda = 427.1$ nm, Ref. [85]).

Based on these assumptions, the hyperfine constants of the levels $289_{11/2}$ and $25164_{13/2}$ are determined by employing the previously introduced gradient-descent fitting algorithm. Since the hyperfine structures of $^{229}\mathrm{Th}^+$ and $^{233}\mathrm{U}^+$ are partially overlapped, only the intervals of the eight resonances outside the Th^+ HFS are considered by the algorithm. The results are shown in Tab. 4.3.

Since the hyperfine A constants are measured with an uncertainty of about

2 %, they could potentially be used, together with measurements on neutral ^{233}U [86], to improve the current value of $\mu = 0.59(5)\,\mu_N$ [87] for the nuclear magnetic dipole moment of ^{233}U by employing high-precision electronic structure calculations (see, e.g., Ref. [47]). The measured B constants are, due to their large uncertainty, not suitable to improve the measured value for the electric quadrupole moment of $Q_s = 3.663(8)\,eb$ $(1\,b = 10^{-28}\,m^2)$ [88].

Since the Th$^+$ measurements using the recoil source show an insufficient amount of loaded ions to resolve the isomeric HFS in a reasonable timescale, further experiments are conducted using Th^{2+} ions.
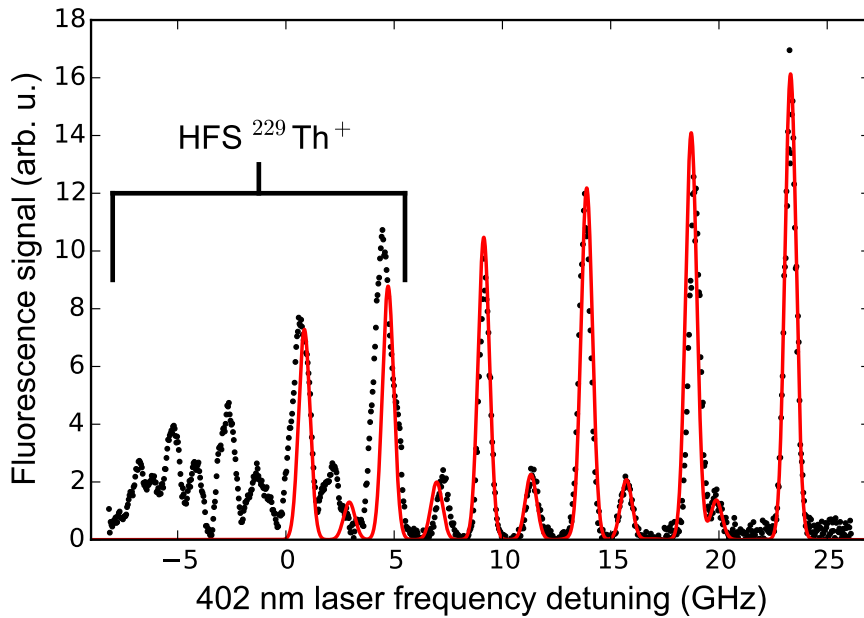

Figure 4.8: **Fluorescence signal recorded using ions loaded from the** ^{233}**U recoil source.** Trapped ions are excited with a laser at 402 nm and fluorescence decay is detected in the wavelength range from 415 nm to 485 nm. Additionally to the expected hyperfine structure of the $0_{3/2} \rightarrow 24874_{5/2}$ transition of ^{229}Th$^+$ (see Fig. 4.1), further resonances are visible. These resonances are assumed to belong to the HFS of the $289.041_{11/2} \rightarrow 25164_{13/2}$ transition of ^{233}U$^+$, which is partially overlapped with the ^{229}Th$^+$ signal. A theoretical curve based on the extracted hyperfine constants is shown in red.
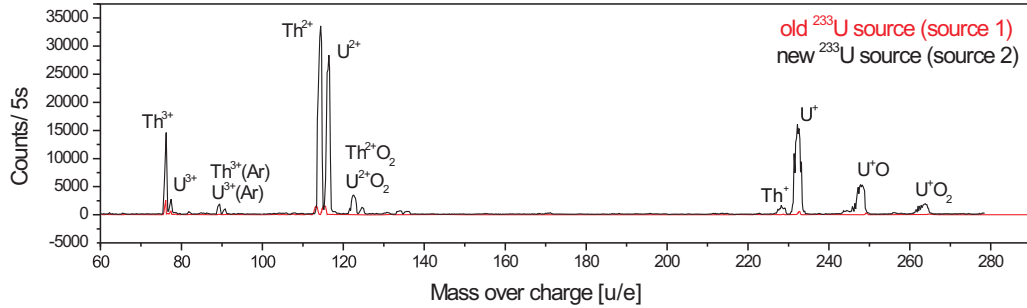
Figure 4.9: **Mass scan of ions loaded from the ^{233}U recoil source.** The mass scan shows that apart from thorium in its 2+ and 3+ charge states, the most abundant ions in the trap are ^{233}U$^+$ and ^{233}U^{2+}. The spectroscopy experiments described here are performed using source 2 (black data points). The figure is adapted from Ref.[17].

Table 4.3: **Hyperfine splitting constants of the levels $289_{11/2}$ and $25164_{13/2}$ of ^{233}U$^+$.** The observed intervals are only slightly effected by the nuclear quadrupole moment, causing large uncertainties for the results of the B constants.

Level (cm^{-1})	A (MHz)	B (MHz)
289	-301(6)	2860(320)
25164	371(8)	215(600)

Chapter 5

Th^{2+} measurements

The HFS of ^{229}Th^{2+} is investigated with three single-step excitations and one two-step excitation with the goal to also measure the HFS of the isomeric state (see Fig. 5.1). Although the amount of Th^{2+} ions generated from photoionization in the trap at PTB is only about 10 % of the Th$^+$ ion number, its extraction rate is about 30 times higher compared to Th$^+$ from the uranium recoil source at LMU (see Fig. 4.9). Detecting the isomer HFS is therefore more likely using hyperfine spectroscopy of Th^{2+}. The transitions are first investigated in the PTB trap before searching for an isomer signal in the LMU trap. Parts of this chapter are already published in Refs. [26; 53; 89].

5.1 Single-step excitations using the PTB trap

Single-photon excitations of Th^{2+} at three different wavelengths, which can be addressed by ECDLs (see Fig. 5.1), are studied to record their HFS in ^{229}Th^{2+} and their isotope shift with respect to ^{232}Th^{2+}. The levels 15148_4 and 21784_4 are excited from the electronic ground state 0_4 via laser radiation at 660.1 nm and 459.1 nm, respectively. The 21784_4 level has a decay channel to the level 3188_4 at 537.8 nm, allowing for a detection free from background of laser stray light by using a narrowband interference filter (transmission window 540 ± 8 nm), while the 15148_4 excitation is detected on the laser wavelength. The level 20711_1 is excited from 63_2 by laser radiation at 484.3 nm and the excitation is detected via fluorescence decay of the $16037_2 \rightarrow 510_2$ transition at 644 nm using a filter transmitting at 643 ± 10 nm. The 63_2 level population

is coupled to the ground state via collisions with the buffer gas, resulting in a population ratio of approximately 0.6. This ratio is calculated assuming a thermal equilibrium described by the Boltzmann distribution.
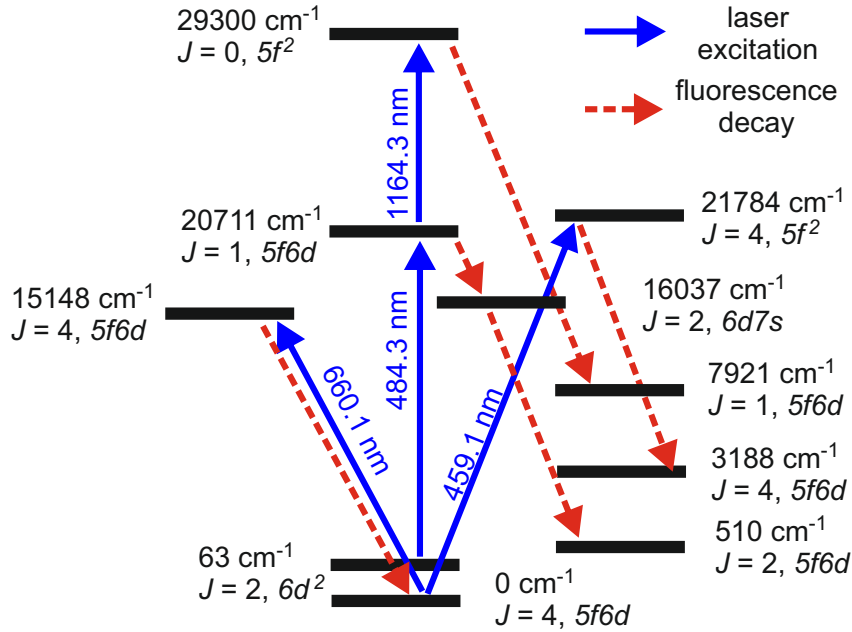

Figure 5.1: **Partial scheme of the ^{229}Th^{2+} level structure.** The investigated transitions of Th^{2+} are depicted. The involved levels are labeled by their energy in cm^{-1}, their angular momentum J and their electronic configuration. Solid arrows show laser excitation and dashed arrows indicate fluorescence decay.

For each of the selected single-step transitions the HFS of ^{229}Th^{2+} and the resonance of ^{232}Th^{2+}, which has no hyperfine structure since the nuclear spin of ^{232}Th is $I = 0$, are measured at the same time to also determine their isotope shifts. To this end, Th^{2+} ions of both isotopes are stored in the trap simultaneously. The fluorescence signals of the three transitions are each recorded while scanning the excitation lasers over a frequency range of up to 12 GHz. The frequency tuning of the lasers during the scanning is measured using a temperature stabilized confocal cavity, similar to the one used in Ch. 4. The output power of each laser is in the range of 10 mW and the beams are retro-reflected to provide saturation absorption spectroscopy as described in Ch. 4. The recorded spectra are shown in Fig. 5.2.
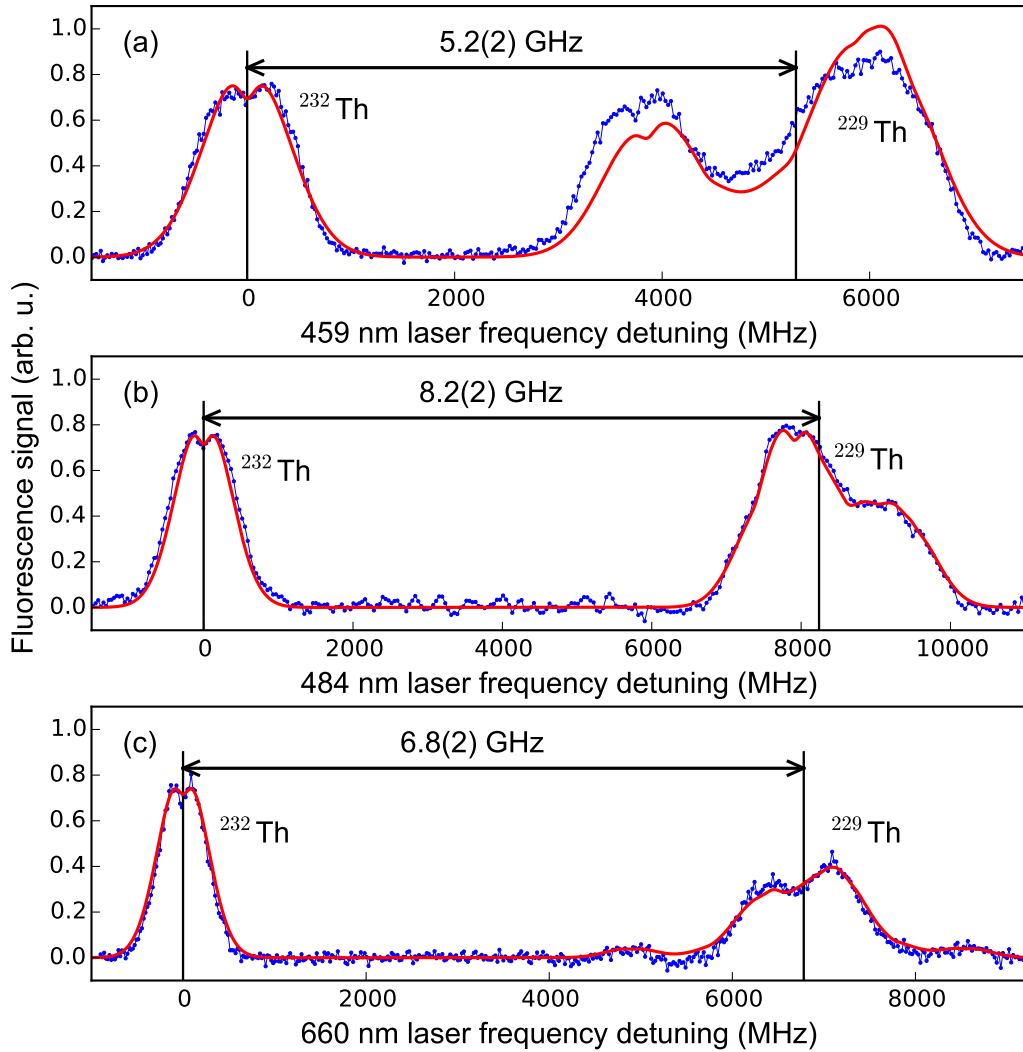
Figure 5.2: **Fluorescence signals of ^{232}Th^{2+} and ^{229}Th^{2+}.** Signals obtained with saturated absorption spectroscopy are shown (blue), together with the theoretical line shapes (red) and the determined isotope shifts. Doppler-free resonances are visible for the ^{232}Th^{2+} signals, but most of them are not resolved for the ^{229}Th^{2+} hyperfine structures due to limited contrast. The ^{229}Th^{2+} HFS centers are determined by overlaying the fluorescence signal with a theoretical line shape based on hyperfine constants presented in Ref.[89] and noting the frequency for $A = B = 0$. The depicted transitions are a) $0_4 \rightarrow 21784_4$ at 459 nm, b) $63_2 \rightarrow 20711_1$ at 484 nm and c) $0_4 \rightarrow 15148_4$ at 660 nm.

The centers of the $^{232}\text{Th}^{2+}$ lines can be easily identified by their nonlinear resonance, but most of the Doppler-free Lamb dips of the $^{229}\text{Th}^{2+}$ HFS are not resolved due to insufficient contrast and SNR, limited by the ion storage time. The center of each HFS is therefore identified by overlaying the spectroscopy signal with a theoretical line shape using the hyperfine constants (A, B) of the involved levels given in Ref. [89]. The amplitudes are calculated based on Eq. 2.22 and taking into account saturation effects to obtain the relative line strengths of the hyperfine components. While the measured and calculated spectra for the $63_2 \rightarrow 20711_1$ and $0_4 \rightarrow 15148_4$ transitions are in good agreement, a mismatch in amplitudes for the $0_4 \rightarrow 21784_4$ transition is visible (see Fig. 5.2 (a)). This mismatch can be probably attributed to optical pumping of the decay channels (see, e.g., Ref. [90]). However, this effect can not be easily taken into account, due to limited data on the decay rates of the involved intermediate levels. This HFS is therefore recorded with a higher SNR to achieve a better contrast for the non-linear resonances (see Fig. 5.3 (a)), in order to determine the hyperfine splitting constants.

The frequency positions of the individual resonances are determined by the zero crossings with negative slope of the third derivative of the spectroscopic signal. The positions of the four main features are marked in Fig. 5.3 with vertical lines. The hyperfine constants are obtained by fitting the intervals between resonances by employing the previously introduced gradient-descent fitting algorithm, taking into account crossover resonances. The best fit is achieved for 0_4: $A = 80\,\text{MHz}$, $B = 3500\,\text{MHz}$ and 21784_4: $A = 25\,\text{MHz}$, $B = 215\,\text{MHz}$. The theoretical values for the hyperfine constants given in Ref. [89] are 0_4: $A = 81(4)\,\text{MHz}$, $B = 3008(260)\,\text{MHz}$ and 21784_4: $A = 26(2)\,\text{MHz}$, $B = 39(45)\,\text{MHz}$. The experimental values for the A constants are in agreement with Ref. [89] and the B constant of the 0_4 level agrees within 2σ. Only the B constant of the level 21784_4 shows a significant discrepancy between theoretical prediction and best experimental fit. However, the HFS centers for the theoretical and the experimental values, determined in both cases by overlapping the measured spectrum with the calculated resonance positions and setting $A = B = 0$, only differ by $50\,\text{MHz}$. Estimating an uncertainty of $150\,\text{MHz}$ for the overlapping of the measurement in Fig. 5.2 (a) and the calculated spectrum yields a total uncertainty of $160\,\text{MHz}$ for the hyperfine

structure center position. The excitation laser exhibits a nonlinear scanning behavior caused by the piezoelectric transducer inside the ECDL. This effect is corrected in the recorded spectrum by monitoring the laser frequency with a reference cavity. The interval measurement between the resonance of ^{232}Th^{2+} and the HFS of ^{229}Th^{2+} has a remaining uncertainty of 80 MHz, giving a total uncertainty of 180 MHz for the isotope shift.

The resulting isotope shifts for all three transitions are depicted in Fig. 5.2. The main contributions to the uncertainties for the transitions $63_2 \rightarrow 20711_1$ and $0_4 \rightarrow 15148_4$ result from the laser frequency interval measurement and from the fit of the calculated HFS to the experimental spectra, giving the same combined rounded value of 200 MHz for the uncertainty in all three transitions.
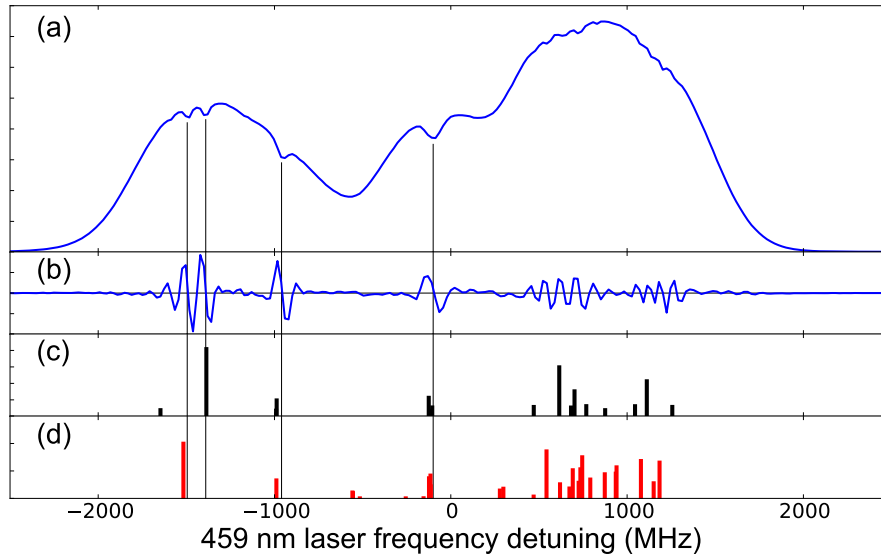

Figure 5.3: **Comparison between measurement and best fit for the** $0_4 \rightarrow 21784_4$ **HFS.** a) Fluorescence signal of the $0_4 \rightarrow 21784_4$ transition in ^{229}Th^{2+}, obtained with saturated absorption spectroscopy. b) Third derivative of the fluorescence signal, showing the non-linear resonances as zero crossings with negative slope (marked with vertical lines). c) Positions and amplitudes of the hyperfine components, obtained from fitting the hyperfine constants A and B of the states 0_4 and 21784_4 to the resonance positions. d) Positions and amplitudes of the expected crossover resonances.

5.2 Single-step excitations using the recoil source

Measurements of the $0_4 \rightarrow 21784_4$ and the $0_4 \rightarrow 15148_4$ single-step transitions in $^{229}\mathrm{Th}^{2+}$ are also conducted using the LMU trap. A wide scanning range of up to 30 GHz is chosen to not only search for the isomeric signal, but also to detect possible signals from other isotopes, elements or molecules which might interfere with the measurements. A SNR of 500 is achieved for the spectrum of the $0_4 \rightarrow 21784_4$ hyperfine structure (see Fig. 5.4). Spurious signals can therefore be excluded for the investigated scan range down to 0.2 % of relative amplitude. Since no additional signal from the isomer is visible, it is assumed that these resonances are covered by the Doppler-broadened nuclear ground state HFS. A two-step excitation scheme is therefore performed as a next experiment.
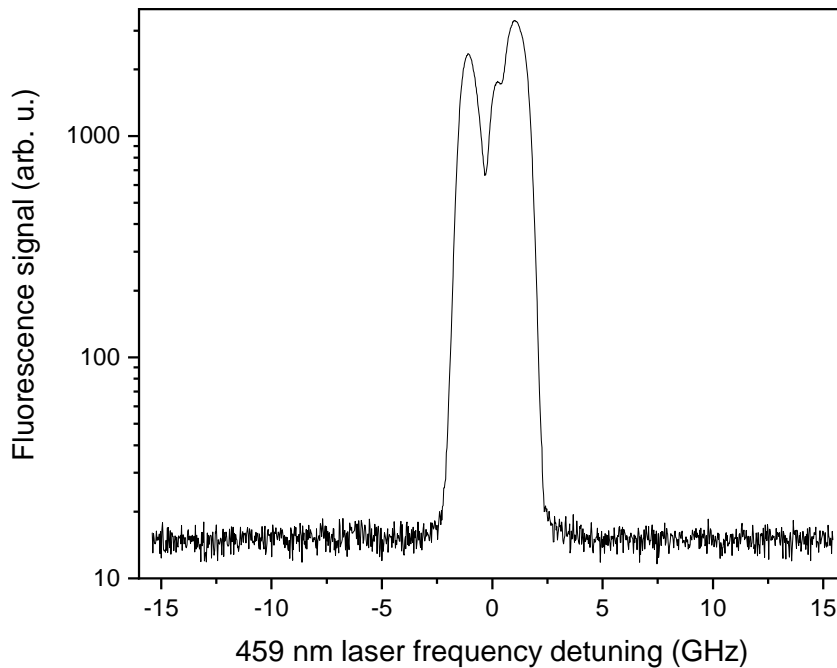

Figure 5.4: **Hyperfine structure of the $0_4 \rightarrow 21784_4$ transition in $^{229}\mathrm{Th}^{2+}$.** The signal is recorded using fluorescence detection free from laser stray light and is depicted in logarithmic scale. A SNR of 500 is achieved, but no isomeric signal was observed inside the scan range of 30 GHz.

5.3 Two-step excitation using the PTB trap

The transition from the 63_2 electronic state to 29300_0 via the 20711_1 intermediate state is selected for Doppler-free two-step spectroscopy (see Fig. 5.1). The 63_2 electronic level is split into five sub-levels for the nuclear ground state ($I = 5/2$) and four sub-levels for the isomeric state ($I = 3/2$). The 20711_1 level consists of three hyperfine levels in both nuclear states. Following the selection rules for electric dipole transitions ($\Delta F = 0, \pm1$ with $F = 0 \nleftrightarrow 0$), the two-step excitation spectrum with $J = 2 \rightarrow 1 \rightarrow 0$ for the nuclear ground and the isomeric state consists of nine and eight resonances, respectively (see Fig. 5.5). The decay of the 29300_0 level to the 7921_1 level at $467.7\,\mathrm{nm}$ also gives the opportunity to employ fluorescence detection free from laser stray light using a bandpass interference filter that transmits in the range of $445 \pm 23\,\mathrm{nm}$.

The HFS is first investigated using the ablation loaded trap at PTB to obtain reference spectra with no isomeric signals present. The spectroscopy part of the experimental setup consists of three ECDLs. The two-step excitation is provided by ECDLs at $484\,\mathrm{nm}$ and $1164\,\mathrm{nm}$ (see Fig. 5.1). Their beams are overlapped and aligned along the trap axis. The diode laser at $459\,\mathrm{nm}$ is used for single-photon excitation of Th^{2+} from the 0_4 ground state to the 21784_4 state to monitor the amount of Th^{2+} ions in the trap in order to normalize the fluorescence signals observed from different HFS components. This is required because the ion number decreases in time due to chemical reactions and charge exchange with impurities in the buffer gas. The power of all lasers in the trap is about $4\,\mathrm{mW}$, corresponding to an intensity of $1.5\,\mathrm{W/cm^2}$ for each beam, which is sufficient to saturate the transitions. A schematic of the employed laser setup is depicted Fig. 5.6.

The recording of the two-step hyperfine structure is performed similar to Sec. 4.2. The frequency of the $484\,\mathrm{nm}$ laser is tuned within the Doppler-broadened HFS of the $63_2 \rightarrow 20711_1$ line in 35 discrete steps of $\approx 120\,\mathrm{MHz}$, shown in Fig. 5.7 schematically as a blue bar. The frequency of the first-step laser is stabilized at each position to the Fizeau wavelength meter with a resulting absolute instability below $5\,\mathrm{MHz}$. For each frequency step of the $484\,\mathrm{nm}$ laser, the second laser at $1164\,\mathrm{nm}$ is scanned continuously over a range of $4\,\mathrm{GHz}$ to provide the excitation of the two-step HFS resonances.
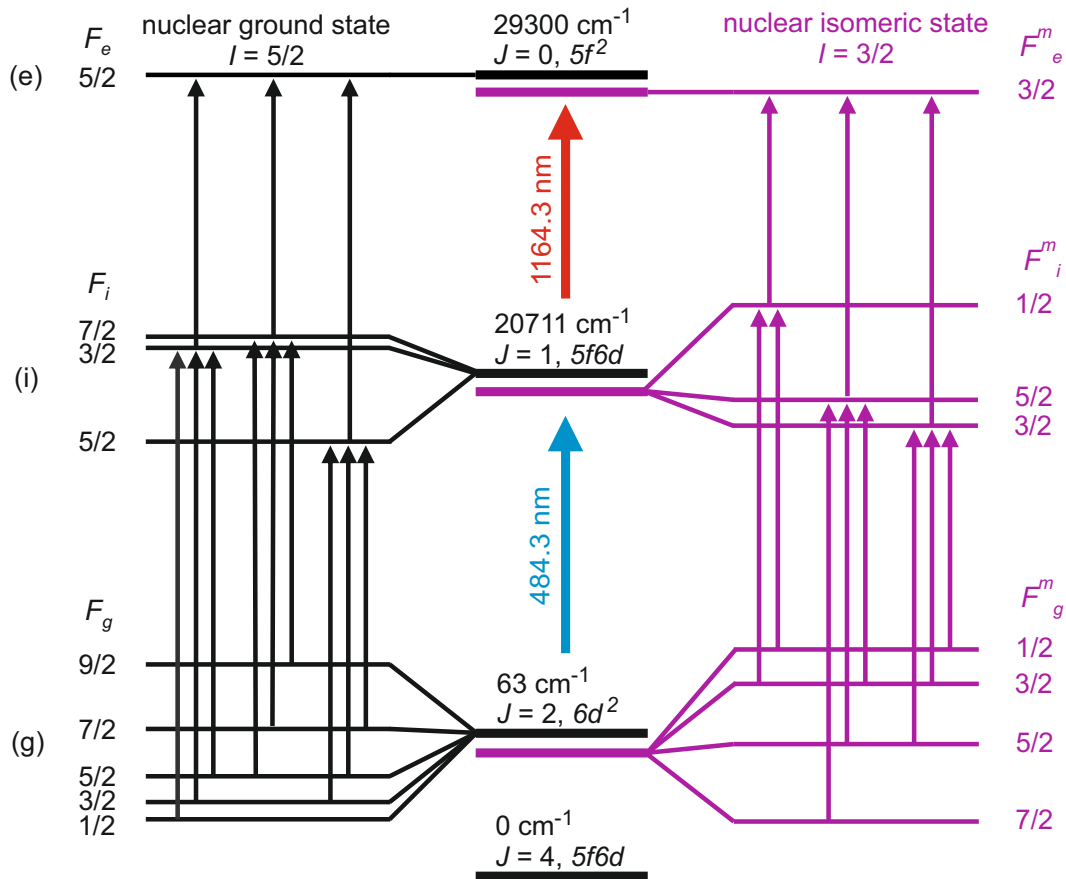
Figure 5.5: **Hyperfine level splitting of the selected Th²⁺ two-step excitation.** The HFS of the transition between initial (g) and intermediate level (i) consists of nine resonances for the nuclear ground state and eight for the isomer. The two-step excitation spectra consist of the same number, respectively, since the intermediate hyperfine sub-levels only have one transition to the excited level (e) each. Hyperfine sub-levels are labeled by their total angular momentum F and F^m.
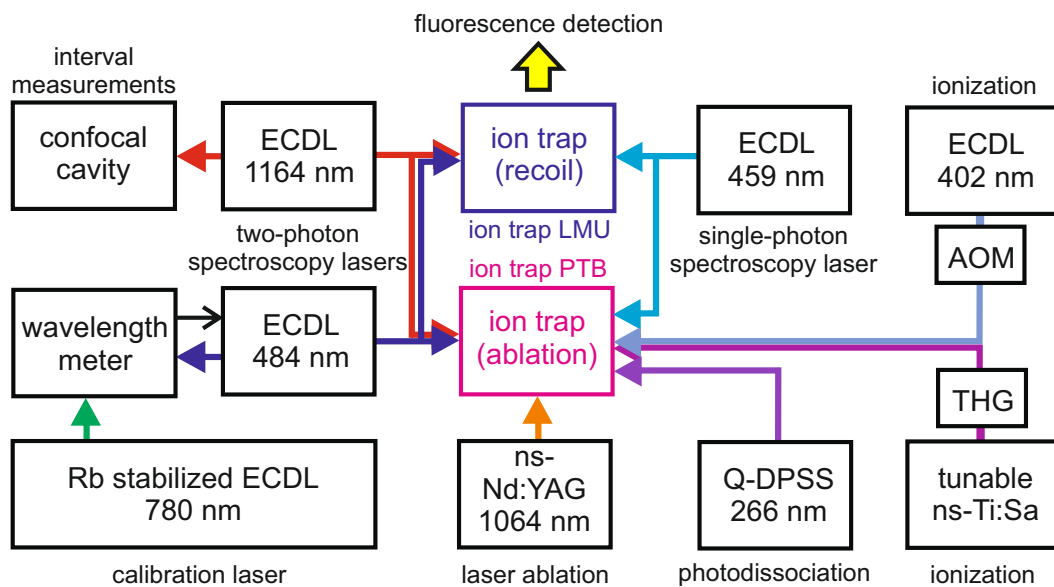
Figure 5.6: **Scheme of the optical setup for the two-step excitation of Th^{2+}.** The first step excitation laser at 484 nm is locked to the wavelength meter. The wavelength meter is calibrated using an ECDL at 780 nm, which is locked to a rubidium line. The tuning of the second step laser at 1164 nm is monitored with a confocal cavity. The 459 nm ECDL is used to determine the amount of ions in the traps via fluorescence detection. The loading of Th^{2+} in the PTB trap is provided by ablation loading of Th$^+$ ions (ns-Nd:YAG 1064 nm) and further three-photon ionization (1st step: 402 nm ECDL, 2nd/3rd steps: THG of ns-Ti:Sa).

The scanning is monitored via a confocal cavity, placed inside a temperature stabilized vacuum chamber. The drift of the cavity resonance frequency at 1164 nm is measured to be less than 5 MHz over the course of one month. The FWHM of the two-step resonances obtained in the PTB trap is 70 MHz using argon as a buffer gas. Six selected spectra of the two-step nuclear ground state HFS resonances for co-propagating beams are shown in Fig. 5.8. All spectra are also recorded with counter-propagating laser beams.
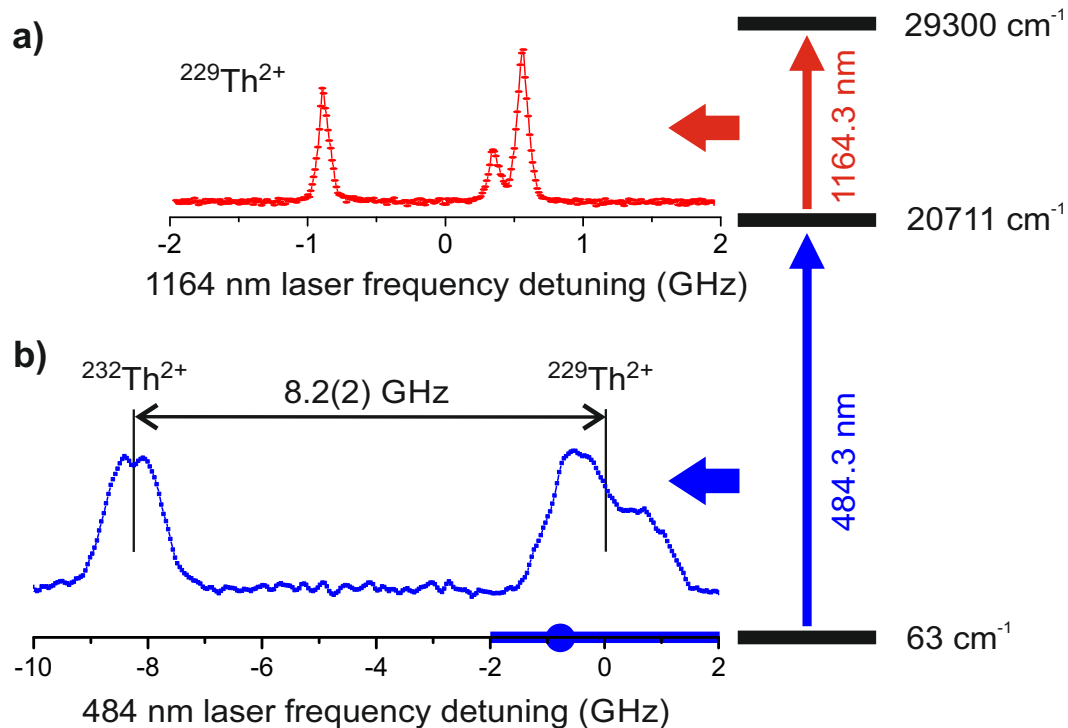

Figure 5.7: **^{229}Th^{2+} two-step excitation.** Exemplary high resolution two-step spectrum (a), depicted together with the Doppler-broadened single-photon spectrum of the first step (b). The first step excitation shows the 8.2(2) GHz isotope shift between ^{232}Th^{2+} and ^{229}Th^{2+}. For the two-step spectrum, the frequency of the first excitation step laser is fixed at -800 MHz detuning (indicated by the blue dot) with respect to the center of the ^{229}Th HFS. Measurements are performed for 35 discrete steps of the laser at 484 nm, indicated schematically by the blue bar on the frequency axis.
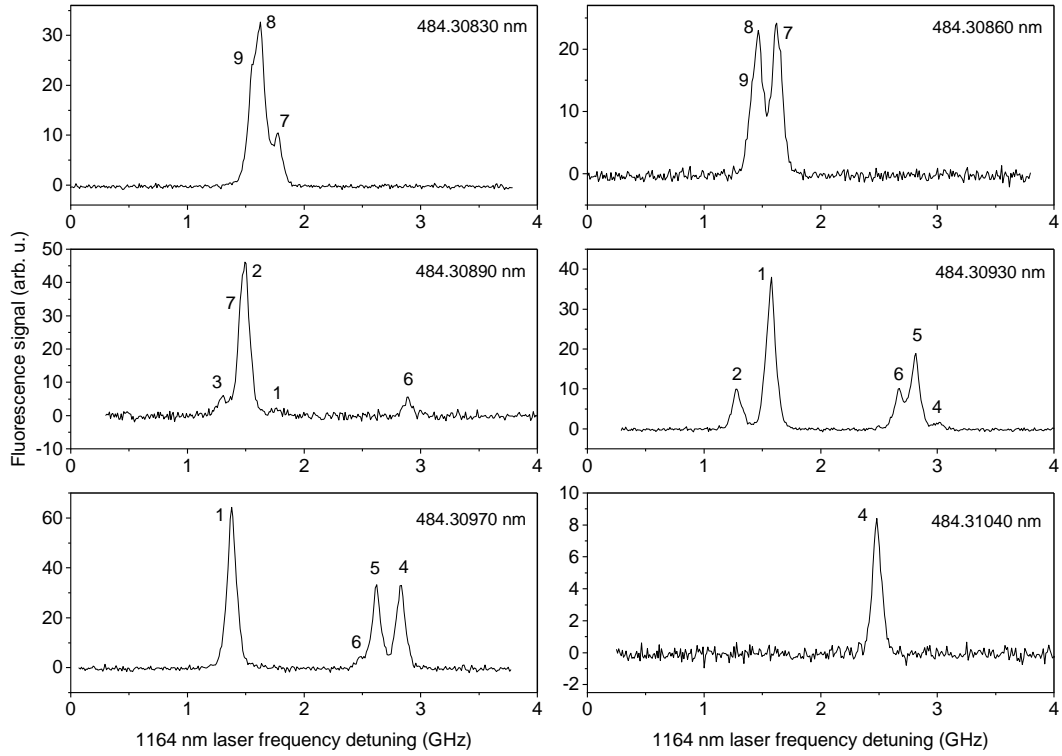
Figure 5.8: **Selected spectra of the two-step excitation of ^{229}Th^{2+} using the PTB trap.** Six spectra for different wavelengths of the first excitation step ECDL at 484 nm (shown in the upper right corners) recorded with co-propagating beams are shown. Resonances are labeled with numbers 1 to 9. The description of the peaks with their respective hyperfine transitions is given in Tab. 5.3.

Analogous to Sec. 4.2 the second-step frequency positions and amplitudes of all resonances for each of the first-step frequencies are extracted by using the multi-peak fit function of Ref. [83]. Nine components are identified in co- and counter-propagating beam configurations, labeled subsequently 1 to 9 (see also Tab. 5.3). In contrast to Sec. 4.2, the amplitude for each resonance in each measurement is now plotted not as a function of the first-step, but as a function of the second-step laser frequency. Fitting Gaussian functions to the data points results in nine curves which are therefore each centered on their corresponding second-step hyperfine transition (see Fig. 5.9).

Some curves show different amplitudes in the co- and counter-propagating plots (see, e.g., No. 2 in Fig. 5.9). These differences occur when the two-step

excitation resonances are not sufficiently resolved, causing distorted values for their amplitudes in the multi-peak fit. However, the influence of this distortion on the later determination of the hyperfine splitting constants is small, since the constants only depend on the intervals between the two-step resonances, not their amplitudes.

Since the 29300_0 level has no hyperfine splitting, the visible structure of three groups only depends on the hyperfine constants of the intermediate 20711_1 level. This allows for a preliminary estimation on its splitting constants as $A \approx 90\,\mathrm{MHz}$ and $B \approx 900\,\mathrm{MHz}$, as well as the assignment of the corresponding second-step hyperfine transitions to the nine resonances, which are also shown in Fig. 5.5.
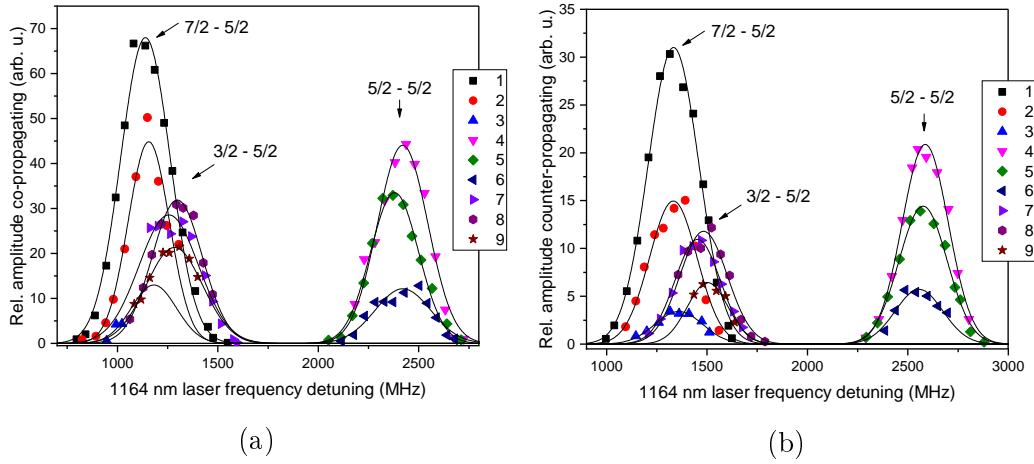

Figure 5.9: **Identification of the second excitation step** $20711_1 \rightarrow$ 29300_0. The experimental points present amplitudes and positions of the two-step resonances obtained by setting the 484 nm laser on selected frequencies and tuning the 1164 nm laser. The frequency of the 484 nm laser is changed in steps of 120 MHz. The results from (a) co- and (b) counter-propagating measurements are depicted. This representation shows, that the resonances 1 to 3, 4 to 6 and 7 to 9 each belong to the same second-step hyperfine transitions, labeled as $F_i \rightarrow F_e$.

The hyperfine constants of the 63_2 level, as well as more precise values for the 20711_1 level, are obtained by fitting the frequency intervals of the two-step hyperfine resonances with the same algorithm used in Sec. 4.2. The determined hyperfine constants are shown in Tab. 5.1. The experimental values

agree with the theoretical values of Ref. [89] inside their 1σ-uncertainty, except for the B constant of the 20711_1 level, which is apart by 2σ. This gives further reassurance that all resonances are identified correctly. The isotope shift of the $20711_1 \rightarrow 29300_0$ transition between ^{232}Th and ^{229}Th is determined analogously to the two-step transition in Sec. 4.2 as 6.2(3) GHz.

Table 5.1: **Hyperfine constants of the ^{229}Th^{2+} levels 63_2 and 20711_1 obtained using the PTB ion trap.**

Level (cm^{-1})	A (MHz)	B (MHz)
63	146(9)	77(67)
20711	86(6)	890(19)

5.4   Two-step excitation using the recoil source

The two-step excitation measurements are conducted at LMU, using the recoil loaded trap, analogously to the experiments with the PTB trap. The frequency of the 484 nm laser is stabilized to the same 35 selected frequencies within the Doppler-broadened HFS of the $63_2 \rightarrow 20711_1$ transition while the 1164 nm laser is scanned. The fluorescence signals are again recorded in co- and counter-propagating beam configurations, resulting in 70 individual spectra. Because the expected isomer signal is in the range of only 2 % of the signal from ions in the nuclear ground state, averaging times of typically four hours per spectrum are chosen. Six representative spectra are shown in Fig. 5.10, while all 70 spectra are available online at Ref. [91]. The measured frequency intervals of the nuclear ground state HFS are used together with the measurements at PTB to reduce the uncertainty of the values for the hyperfine splitting constants.

The final results are shown in Tab. 5.2. 50 % of the total uncertainty is given by the systematic uncertainty, with the main contributions coming from the uncertainty in the reference cavity length, the instability of the frequency of the first excitation step laser and the non-linearity of the frequency tuning of the second-step laser.
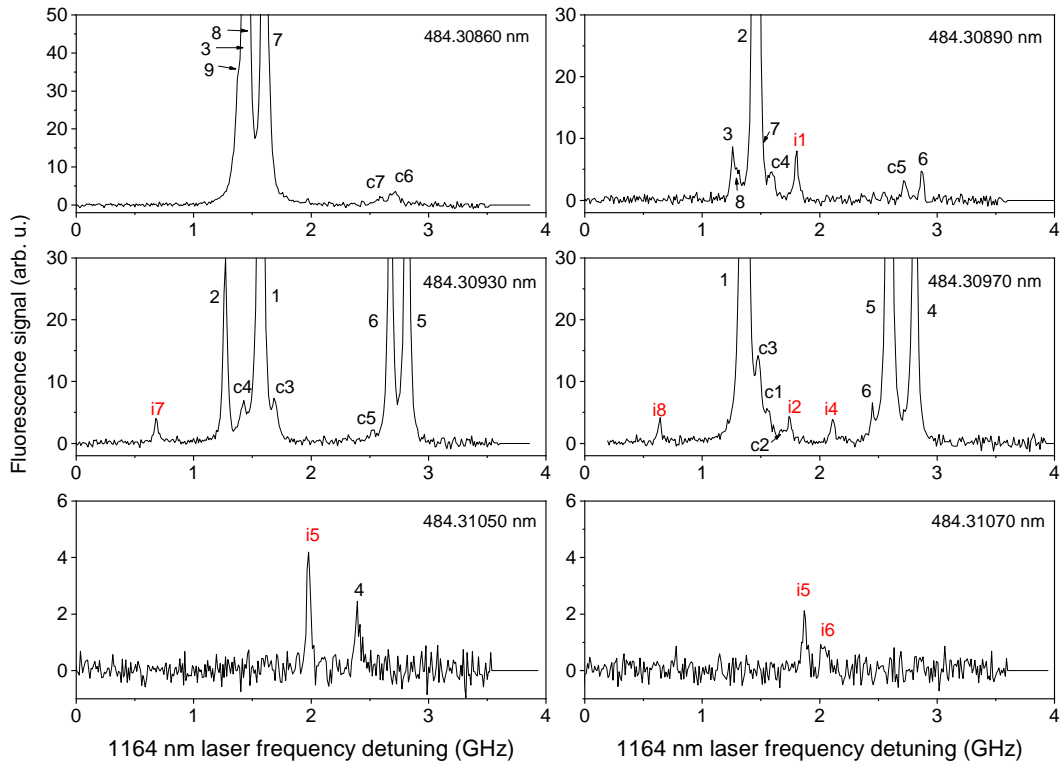
Figure 5.10:   **Selected spectra of the two-step excitation of ^{229}Th^{2+} loaded from the recoil source.** Six spectra for different wavelengths of the first excitation step ECDL at 484 nm (shown in the upper right corners) recorded with co-propagating beams are shown. Resonances belonging to the nuclear ground state are labeled with numbers 1 to 9, isomeric resonances with i1 to i8. Resonances originating from state-changing collisions of ions in the intermediate state with the buffer gas are labeled c1 to c7. The description of the peaks with their respective hyperfine transitions is given in Tab. 5.3.

Table 5.2:   **Final values for the hyperfine constants of the levels 63_2 and 20711_1 of ^{229}Th^{2+}.**

Level (cm^{-1})	A (MHz)	B (MHz)
63	151(8)	73(27)
20711	88(4)	897(14)

The recordings are evaluated analogously to the previous two-step experiments. The individual resonances are identified by their expected shift of $\Delta f_2 = \pm \Delta f_1 \cdot k_2/k_1 = 50\,\mathrm{MHz}$ between scans, when the first excitation step laser at $484\,\mathrm{nm}$ is shifted by $120\,\mathrm{MHz}$. Additionally to the nine resonances of the nuclear ground state HFS, 16 extra resonances for the co-propagating and 13 extra resonances for the counter-propagating beam configuration are observed (see, e.g., Fig. 5.10). The isomer HFS consist of eight resonances, which leads to the conclusion that at least one additional source of signals must be present. These resonances need to be identified to distinguish them from the isomer HFS.
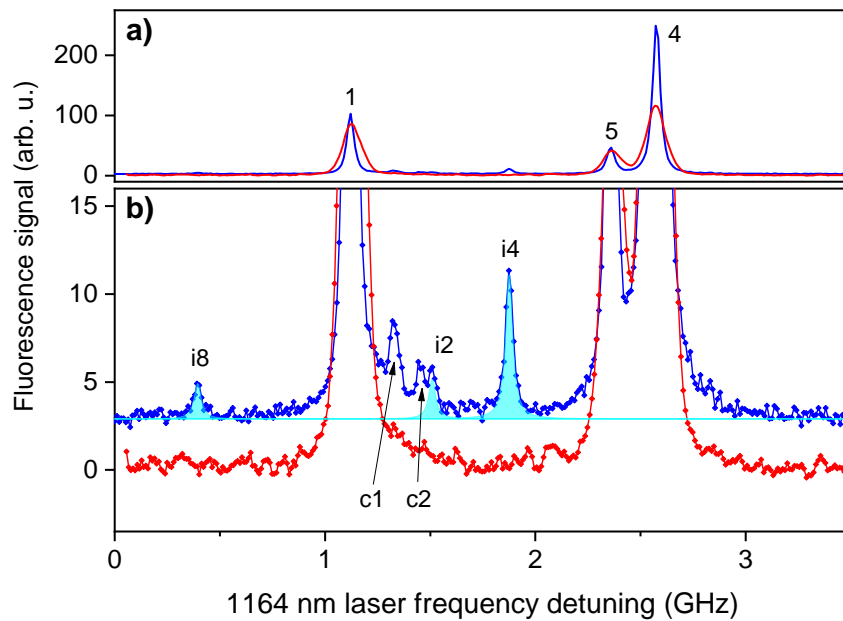

Figure 5.11: **Comparison of excitation spectra obtained in the two traps.** a) Two-step excitation spectrum of $^{229}\mathrm{Th}^{2+}$, where the first excitation step laser is stabilized at $-800\,\mathrm{MHz}$ detuning with respect to the $^{229}\mathrm{Th}$ HFS center and the second excitation step laser is scanned. Signals obtained using the PTB and the LMU trap are shown in red and blue, respectively. Resonances are labeled according to Tab. 5.3. b) Enlarged view of (a), with the signal recorded at LMU up-shifted for better inspection and the isomeric state resonances marked in cyan. The resonances c1 and c2 belong to the nuclear ground state and arise from a collision-induced change of the intermediate HFS state.

Table 5.3: **Labeling of the observed ^{229}Th^{2+} two-step resonances.** The two-step excitation resonances are listed with the total angular momenta F of the electronic states involved in the excitation. The resonances belonging to the nuclear ground state are labeled with numbers 1 to 9. Resonances that arise from changes of the intermediate hyperfine state via collisions are described by both quantum numbers, F_i (before the collision) and F_i' (after the collision), and are labeled c1 to c7. Isomeric resonances are labeled i1 to i8. The resonance i3 (marked with an asterisk) is not observed in the experiment.

Label	$F_g \to F_i \to F_e$	Label	$F_g \to F_i\,;\,F'_i \to F_e$	Label	$F^m_g \to F^m_i \to F^m_e$
1	$9/2 \to 7/2 \to 5/2$	c1	$7/2 \to 5/2;\ 7/2 \to 5/2$	i1	$7/2 \to 5/2 \to 3/2$
2	$7/2 \to 7/2 \to 5/2$	c2	$7/2 \to 5/2;\ 3/2 \to 5/2$	i2	$5/2 \to 5/2 \to 3/2$
3	$5/2 \to 7/2 \to 5/2$	c3	$9/2 \to 7/2;\ 3/2 \to 5/2\ \&$	i3*	$3/2 \to 5/2 \to 3/2$
4	$7/2 \to 5/2 \to 5/2$		$5/2 \to 5/2;\ 3/2 \to 5/2$	i4	$5/2 \to 3/2 \to 3/2$
5	$5/2 \to 5/2 \to 5/2$	c4	$7/2 \to 7/2;\ 3/2 \to 5/2$	i5	$3/2 \to 3/2 \to 3/2$
6	$3/2 \to 5/2 \to 5/2$	c5	$7/2 \to 7/2;\ 5/2 \to 5/2$	i6	$1/2 \to 3/2 \to 3/2$
7	$5/2 \to 3/2 \to 5/2$	c6	$5/2 \to 3/2;\ 5/2 \to 5/2$	i7	$3/2 \to 1/2 \to 3/2$
8	$3/2 \to 3/2 \to 5/2$	c7	$3/2 \to 3/2;\ 5/2 \to 5/2$	i8	$1/2 \to 1/2 \to 3/2$
9	$1/2 \to 3/2 \to 5/2$				

5.4.1 Exclusion of spurious signals

As a first possible source of additional signals, the radiation of the spectroscopy lasers is investigated. Unwanted additional resonances can, for example, occur if a laser emits several frequencies simultaneously. This multi-mode operation has been excluded by investigating the transmission signal of the reference cavity, which would show the additional modes, and by varying the laser diode current, which would change the ratio of the mode amplitudes. Additionally, a back reflection of the spectroscopic laser beams, which would lead to a mixing of co- and counter-propagating signals, is excluded by comparing measurements for the same laser frequencies in both beam geometries. These tests confirm that the observed resonances are original spectroscopic features.

The next possible candidates for extra resonances are other isotopes of thorium and elements emitted from the uranium recoil source, like the ^{233}U$^+$ line observed in Ch. 4. Tab. 3.1 shows upper limits for the presence of the isotopes ^{228}Th and ^{230}Th. The resonance of ^{230}Th, which has no HFS since the nuclear spin of ^{230}Th is 0, should appear between the lines of ^{232}Th and ^{229}Th, like

those of the ^{229m}Th HFS. However, the isotope shift of ^{230}Th^{2+} with respect to ^{229}Th^{2+} for the $63_2 \rightarrow 20711_1$ transition is determined as 3.2 GHz, calculated from measurements of the $0_4 \rightarrow 21784_4$ transition in ^{230}Th^{2+} using a ^{234}U source and from Ref. [76]. This is outside the frequency range of the observed resonances. A dedicated search experiment with the ^{233}U source did not show a ^{230}Th^{2+} resonance, indicating a significantly smaller extraction rate than listed in Tab. 3.1.

Concerning spectral lines of other elements than thorium, only uranium and plutonium have an extracted flux high enough to possibly be detected. Possible transitions need to originate from low-lying levels that can be populated via collisions with the buffer gas. For the first excitation step at 484 nm, the nearest U and Pu lines are detuned by ≈ 200 GHz (^{238}U$^+$, $\tilde{\nu} = 20640.51$ cm^{-1}, $915_{9/2} \rightarrow 21555_{9/2}$) and ≈ 60 GHz (^{240}Pu$^+$, $\tilde{\nu} = 20645.62$ cm^{-1}, $3970_{5/2} \rightarrow 24615_{3/2}$) (Refs. [85; 92; 93]). These lines are outside the investigated spectral range and can therefore also be excluded.

Compounds of thorium with organic molecules are present in the ablation loaded PTB trap (see Ch. 3), but do not lead to additional resonances inside the investigated frequency ranges. Influences from Th^{2+}He complexes, potentially formed by interaction with the buffer gas, are excluded as well. Measurements of the two-step excitation of ^{232}Th^{2+} ions with He buffer gas using the PTB trap do not show additional features arising from Th-He-compounds. Moreover, the binding energy can be estimated to be below 7500 cm^{-1} (see, e.g., Ref. [94]). The laser excitation at 484 nm (20648 cm^{-1}) is therefore expected to dissociate possible Th-He compounds. Even if these compounds are present, the line shift is expected to be at least some tens of GHz, i.e. outside the analyzed frequency range (see, e.g., Ref. [95]). Concerning other noble gas compounds, mass spectrometry analyses of the LMU system show the presence of Th^{3+}Ar, but no Th^{2+}Ar.

The above listed exclusions only regard spurious signals at the first excitation step wavelength of 484 nm. Since the detected signals additionally require the coincidence of two resonance conditions, it can be excluded with a high confidence that the recorded thorium spectra are affected by other elements.

5.4.2 Hyperfine state-changing collisions

Some of the additional resonances appear at fixed intervals from strong ground state resonances of 1126 MHz, 1250 MHz and 124 MHz, which correspond to the second step hyperfine splitting (see Fig. 5.9 and Fig. 5.12). These resonances also display a dependency on the buffer gas in the way that their relative amplitudes decrease with reduction of the buffer-gas pressure in comparison with the other resonances (see Fig. 5.13).
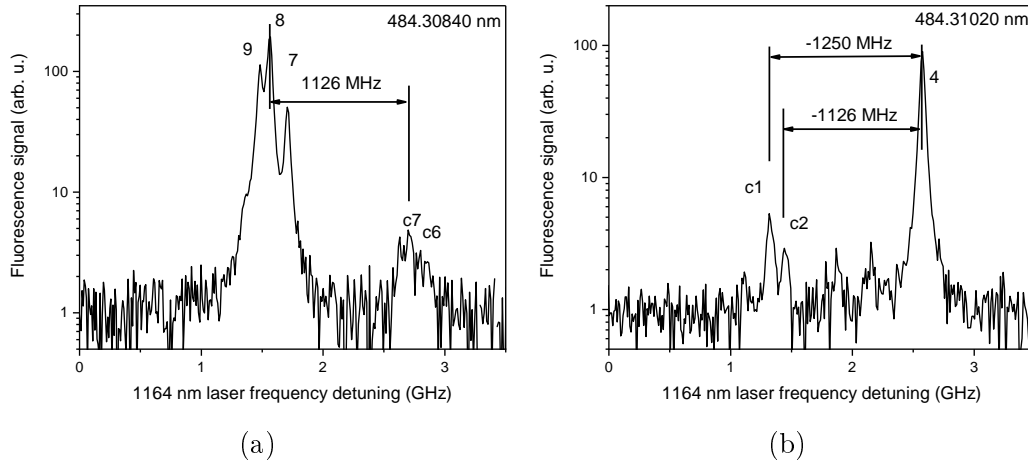

Figure 5.12: **Collision-induced intermediate HFS state changes.** Two exemplary spectra showing weak resonances with a characteristic frequency interval of 1126 MHz or 1250 MHz from a strong resonance. These weak signals arise from different intermediate hyperfine states than the main feature. These states are populated via collisions of ions in the intermediate level with the buffer gas. The resonances are labeled according to Tab. 5.3.

These characteristics lead to the conclusion, that these resonances arise from collision-induced changes of the intermediate state HFS population due to interactions with the buffer gas (see, e.g., Ref. [96]). The width of these resonances is approximately 1.5 times larger than the width of the nine main HFS resonances. The spectra recorded using the PTB trap only show slight deformations instead of resonances, indicating that the magnitude of this effect is significantly higher with helium as buffer gas in the LMU trap than with argon in the PTB trap. This can be explained by the larger momentum transfer of collisions with argon atoms, leading to a stronger line broadening and a higher quenching rate to lower electronic levels. Also, the He buffer gas in the

LMU trap is applied through the Laval nozzle between the stopping cell and the quadrupole chamber (see Fig. 3.5), probably resulting in a higher gas density along the trap axis. The positions of resonances caused by collision-induced hyperfine state changes can be calculated based on the measured hyperfine splitting of the intermediate state. By this method, nine resonances in the co-propagating measurements and six in the counter-propagating are classified as originating from collisions, appearing, e.g., as resonances c1 and c2 in Fig. 5.11.

Based on the analysis above, seven new resonances in both beam configurations cannot be attributed to sources of spurious signals. These resonances are therefore identified as the isomeric hyperfine structure.
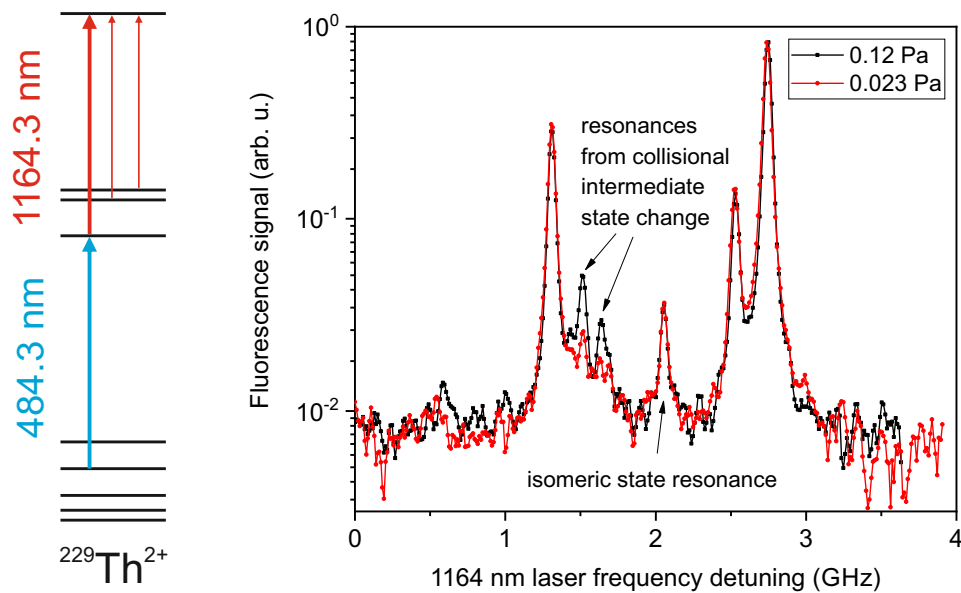
Figure 5.13: **Pressure dependence of collision-induced intermediate HFS state changes.** Two-step excitation spectra of Th^{2+} recorded for two different He buffer-gas pressures are shown. With reduction of the buffer-gas pressure, the relative amplitudes of the collisional resonances decrease. Note that neither the three strong nuclear ground state resonances, nor the isomeric resonance are affected by the change in He pressure. The collisional resonances are shown in the level scheme on the left as thin red lines.

5.4.3   Splitting constants of the isomeric HFS

The seven resonances are evaluated analogously to the previously described two-step hyperfine structures. Plotting the amplitudes as a function of the second-step laser frequency enables an assignment of the individual hyperfine transitions (see Fig. 5.14). Calculating their relative amplitudes using Eq. 2.22 shows that the missing 8th resonance is supposed to be the weakest one and is too small to be resolved at the SNR achieved in the experiment.

The evaluation of the newly observed seven peaks using the gradient-descent fitting algorithm gives consistent results for the data from co- and counter-propagating beam geometries and fits to the HFS pattern of a $I = 3/2$ nuclear spin. The isomeric hyperfine constants of the investigated levels are shown in Tab. 5.4.

The fitting for the isomeric state is provided without imposing fixed proportions A^m/A and B^m/B, which have to occur for both electronic states. That these proportions are in fact the same for both levels and that all observed resonances in all individual spectra can be classified without ambiguities makes it highly unlikely for a spurious unrelated spectral feature to be misinterpreted and gives confidence that the isomeric signal is identified correctly.

Table 5.4: **Hyperfine splitting constants of the levels 63_2 and 20711_1 for the isomeric nuclear state.**

Level (cm^{-1})	A^m (MHz)	B^m (MHz)
63	-263(29)	53(65)
20711	-151(22)	498(15)
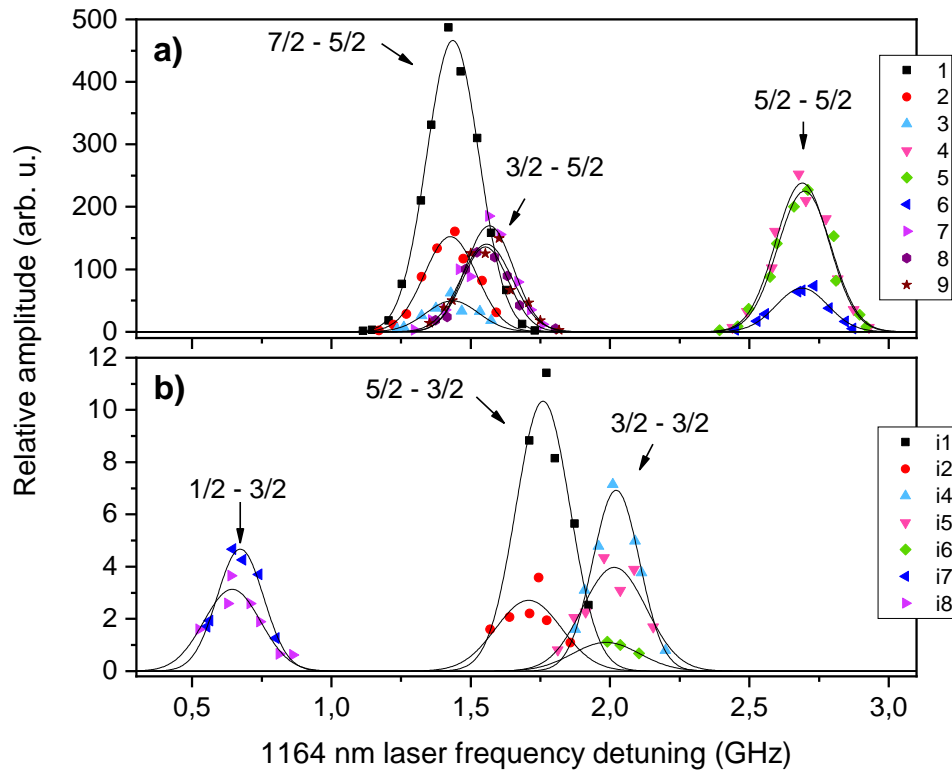
Figure 5.14: **Identification of the second excitation steps for ^{229}Th^{2+} and ^{229m}Th^{2+}.** The data points represent amplitudes and positions of the two-step resonances of a) nuclear ground state and b) isomer in all 35 spectra obtained with co-propagating beam configuration, analogous to Fig. 5.9a. Groups are labeled by their corresponding second excitation step momenta $F_i \rightarrow F_e$ and resonances are labeled according to Tab. 5.3.

Chapter 6

Isomer properties

Based on the observed hyperfine structure of the Th^{2+} ions in the isomeric state, the hyperfine constants of the 63_2 and the 20711_1 level for both nuclear states are determined in the previous chapter. These constants are directly coupled to the interaction between the electron shell and the nucleus (see Ch. 2) and can therefore be used to gain knowledge on the nuclear structure of the isomeric state. Parts of this chapter are already published in Ref. [26].

6.1   Magnetic dipole moment

The hyperfine splitting constant A is related to the nuclear magnetic dipole moment μ by Eq. 2.20. The measured ratio $A^m/A = -1.73(25)$ therefore determines the magnetic dipole moment μ^m of the isomer according to the relation $\mu^m = \mu A^m I^m/(AI)$, with μ being the magnetic moment of the nuclear ground state and I^m and I being the nuclear spin values of the isomeric and the nuclear ground state, respectively (see, e.g., Ref. [48]). Hyperfine structure anomalies are neglected, since they are small for the d^2, fd, and f^2 electronic configurations of Th^{2+} levels [97; 98]. Therefore, the ratio of the magnetic moments of the isomer and nuclear ground state is $\mu^m/\mu = $ -1.04(15). The nuclear magnetic moment μ of the ground state has been measured in two experiments [99; 100], with the most precise value $\mu = 0.360(7)\,\mu_N$ resulting from the combination of high-precision calculations [47] and hyperfine spectroscopy of laser-cooled $^{229}Th^{3+}$ ions [100]. Based on this value the magnetic dipole moment of the isomeric state is derived as $\mu^m = -0.37(6)\,\mu_N$.

As introduced in Ch. 2, an estimate based on the leading Nilsson configuration [44; 46] had predicted $\mu^m = $ -0.076 μ_N. Assuming that the discrepancy is not caused by experimental errors, this indicates that the simplifying Nilsson approach is insufficient for quantitatively characterizing the isomer (see also Refs. [39; 101]). In a recent paper, Minkov and Pálffy gave a value for the magnetic dipole moment of the isomer, based on a model that includes among others the effects of collective quadrupole-octupole vibration-rotation motion and the Coriolis interaction between the valence neutron and the core [102]. Their result of $\mu^m = $ -0.35 μ_N is in good agreement with the experimental value, although the discrepancy between predicted and measured nuclear ground state magnetic moment slightly increased. They also investigated the transition probability B(M1) for magnetic decay of the isomeric state, pointing out that their model yields a considerable smaller value, leading to a longer radiative lifetime than the so far assumed $\approx 3 \cdot 10^3$ s [42].

6.2 Electric quadrupole moment

Employing Eq. 2.20, the spectroscopic quadrupole moment of the isomeric state Q_s^m can be determined from $Q_s^m = Q_s B^m / B$, with Q_s being the spectroscopic quadrupole moment of the nuclear ground state. The measured ratio $B^m / B = 0.555(19)$ (see Tab. 5.2 and Tab. 5.4) is mostly derived from the constants of the 20711_1 electronic state, due to the large uncertainty of the values obtained for the 63_2 level. The electric quadrupole moment of the nuclear ground state Q_s has been measured in two independent experiments as 3.15(3) eb [45] and 3.11(6) eb [47; 100]. Using the weighted mean of these two values, the spectroscopic quadrupole moment of the isomer is determined as $Q_s^m = 1.74(6)$ eb.

As introduced in Ch. 2, the quadrupole deformation in the reference frame of the nucleus is given by the intrinsic quadrupole moment Q_0, which is connected to Q_s via Eq. 2.18, giving $Q_0 = \frac{14}{5} Q_s$ for the nuclear ground state and $Q_0 = 5 Q_s$ for the isomer. The resulting intrinsic quadrupole moments are $Q_0 = 8.8(1)$ eb and $Q_0^m = 8.7(3)$ eb, respectively. To within the uncertainty, the intrinsic quadrupole moments of both states are therefore the same

$(Q_0^m/Q_0 = 0.991(34))$, which is in good agreement with theoretical predictions [101; 103].

6.3   Mean squared charge radius

The isomeric state is also expected to have a different mean squared charge radius compared to the nuclear ground state, resulting in an isomeric shift of the HFS. The shifts of the two excitation steps are derived from the centers of the hyperfine structures, calculated by setting $A = B = 0$. The isomeric HFS is shifted to lower frequency relative to ^{229}Th^{2+} by $0.29(3)$ GHz for the $63_2 \rightarrow 20711_1$ transition and by $0.21(5)$ GHz for the $20711_1 \rightarrow 29300_0$ transition. The corresponding isotope shifts between ^{229}Th^{2+} and ^{232}Th^{2+} are $8.2(2)$ GHz and $6.2(3)$ GHz (see Ch. 5). The isomeric shift arises purely from the field shift caused by the change in nuclear radius. The isotope shift on the other hand also depends on the mass shift (see Ch. 2). Since only the field shifts have to be compared to extract the nuclear radius change, the contribution of the mass shift needs to be excluded. This is achieved by employing results of a theoretical analysis of the isotope shift between ^{232}Th and ^{229}Th in Ref. [53], which is partially based on experimental results of Ch. 5. The resulting average ratio of isomer and isotope field shifts for both transitions is $0.036(5)$. The difference in mean-squared charge radius between ^{232}Th and ^{229}Th is $\delta\langle r^2 \rangle^{232,229} = 0.299(15)$ fm^2 [53], with $\langle r^2 \rangle^{229} = 33.13(17)$ fm^2 [41]. Therefore, the difference between the mean squared radii of the isomeric and nuclear ground state in ^{229}Th is $\delta\langle r^2 \rangle^{229m,229} = 0.0107(16)$ fm^2.

6.4   Sensitivity to temporal variations of α

The possibility of temporal variations of fundamental constants has been discussed already in 1937 in the framework of relativistic cosmology [104; 105], but they have not been experimentally observed yet. A nuclear clock based on ^{229}Th has been proposed in Ref. [16] as a particularly sensitive system to search for temporal variations of the fine structure constant α.

The proposal is based on the model that the small nuclear transition energy $E_{is} \approx 8$ eV appears as the result of the nearly perfect cancellation of

the changes in Coulomb energy $\Delta E_C = E_C^m - E_C \approx -1\,\text{MeV}$ and energy from the strong interaction between the two nuclear states. The sensitivity $((\alpha/f)\mathrm{d}f/\mathrm{d}\alpha)$ of the nuclear transition frequency to the value of α would then be equal to the ratio $\Delta E_C/E_{is}$. However, this model has been criticized based on the reasoning that the transition is mainly performed by an unpaired neutron, leaving the Coulomb energies of ^{229}Th and $^{229\mathrm{m}}$Th essentially equal [106]. Theoretical estimations of ΔE_C from nuclear structure calculations [101; 106] vary from a few keV to a few MeV. It has therefore been proposed to calculate E_C via the change of the nuclear charge radius and electric quadrupole moment from measured isomer shift and HFS data [107]. Following Ref. [107] and treating the nucleus as a uniform, hard-edged, prolate spheroid, the change in Coulomb energy can be expressed in terms of the change in mean squared charge radius and electric quadrupole moment, which are measured above, as

$$\Delta E_C = -485\,\text{MeV}((\langle r^2\rangle^{229\mathrm{m}}/\langle r^2\rangle^{229}) - 1) + 11.6\,\text{MeV}((Q_0^m/Q_0) - 1), \quad (6.1)$$

using updated values of Q_0 and $\langle r^2\rangle^{229}$. The resulting change in Coulomb energy is $\Delta E_C = -0.26(40)\,\text{MeV}$. The uncertainty of ΔE_C is dominated by the $4\,\%$ uncertainty of Q_0^m/Q_0. This result is therefore not sufficient to prove $|\Delta E_C| \gg E_{is}$. Nevertheless, the obtained value for the change in Coulomb energy would correspond to a sensitivity of a ^{229}Th nuclear clock to changes in α of about 10^4. It is therefore likely, that the sensitivity of such a clock exceeds those of present atomic clocks by several orders of magnitude [108].

6.5 Further isomer properties

Apart from the nuclear structure, the simultaneous measurement of the HFS for both nuclear states gives insight into further properties of ^{229}Th and its isomeric state.

The fraction of ions in the isomeric state that are extracted from the ^{233}U recoil source was so far only inferred from γ-spectroscopy [109]. By comparing the integrated fluorescence signals of isomeric and nuclear ground state resonances, the first directly measured value can be provided, determining a branching ratio of $2.1(5)\,\%$ (see Fig. 5.14), which confirms the previously assumed value.

The experimental setup is in principle also suitable to determine the isomeric lifetime in Th^{2+}. Since the isomeric state has a finite lifetime, the amplitudes of the corresponding resonances will show an exponential decay. However, this experiment is impeded by the limited storage time of the ions in the trap of $\tau \approx 60\,\mathrm{s}$, determined by chemical reactions and charge exchange with impurities in the buffer gas. During this time, no change in the amplitude ratio is observed. Hence, the value of $60\,\mathrm{s}$ can only be given as a lower limit for the isomer lifetime, confirming the result in Ref. [24]. To measure the isomeric lifetime on its expected timescale of $\approx 10^4\,\mathrm{s}$ [42] via this method, an improvement of the storage time by two orders of magnitude would be necessary.

The nuclear moments of the isomer are also important when estimating the performance of a future nuclear clock. In the case of a single ion clock based on ^{229}Th^{3+} and employing stretched states, the hyperfine-mediated shift ΔX^{HFS} on the transition can be expressed as [13]:

$$\Delta X^{HFS} = \left(\frac{\mu^m - \mu}{\mu_N} \right) \bar{X}_{\mu}^{HFS} + \left(\frac{Q_0^m - Q_0}{|e|\mathrm{b}} \right) \bar{X}_{Q}^{HFS}, \qquad (6.2)$$

with $\bar{X}_{\mu,Q}^{HFS}$ being form factors that only depend on the electronic wave functions. With the new value for the magnetic dipole moment of the isomer, the differential Zeeman shifts can be calculated as $\Delta E_Z / \mathrm{B} \approx \pm 5.5\,\mathrm{kHz/mT}$, which is about $40\,\%$ larger than the value given in Ref. [13]. However, this will not impact the estimated uncertainty for the transition frequency of the clock, which is still dominated by the effects of excess micromotion and gravitational shifts.

Chapter 7

Search for electronic bridge excitation in Th^{2+}

This chapter discusses an experiment aimed at exciting the ^{229}Th nucleus via an electronic bridge process in Th^{2+} ions. As introduced in Ch. 2, electronic bridge excitation relies on the coupling between the electron shell and the nucleus. In the case of the low-lying ^{229}Th isomer, if an M1 or E2 decay channel of the electron shell is in resonance with the nuclear excitation, the shell can decay non-radiative while exciting the nucleus [32; 110; 111].

Experiments have already been performed to search for a corresponding process using Th^{+}, which exhibits a high electronic level density due to its three valence electrons [65]. In this experiments, ions were excited in a two-step scheme with one visible and one UV photon to address levels in the energy range of the isomer, subsequently referred to as 'high-lying' states. However, exciting high-lying levels in Th^{+} can lead to three-photon ionization (see Ch. 3), since one additional UV photon can excite the ion above its ionization potential of 12.1(2) eV [66]. The laser power applied during these experiments was therefore limited to be far below saturation, leading in turn to a limited population transfer to the high-lying states.

In contrast, no ionization of Th^{2+} is expected in a similar scheme due to its ionization potential of 18.33(5) eV [93]. This allows for saturating transitions to high-lying states to maximize their population. A disadvantage of Th^{2+} is, that it does not possess electronic levels inside the 1σ-range of the isomer energy 8.28(17) eV (Refs. [9; 112; 113]), which could enhance a bridge excita-

tion [32]. However, it does possess levels at higher energy between 9.25 eV and 10.32 eV. These levels can couple to low-lying states of up to 2.57 eV via M1 or E2 transitions, which in turn decay to the ground state, either via dipole transitions or via collisional quenching induced by the buffer gas [30]. This allows for M1/E2 transitions from 7.14 eV to 10.46 eV, which can couple to the nuclear transition in the case of resonance (see Fig. 7.1). All individual levels are listed in the appendix in Tab. A.3 and Tab. A.4. This process has also been referred to as 'nuclear excitation via a two-photon electron transition' (NETP) [33]. Its excitation rate, depending on the isomer energy and the high-lying electronic level, has been investigated in a theoretical study (Ref. [33], see Fig. 7.2).
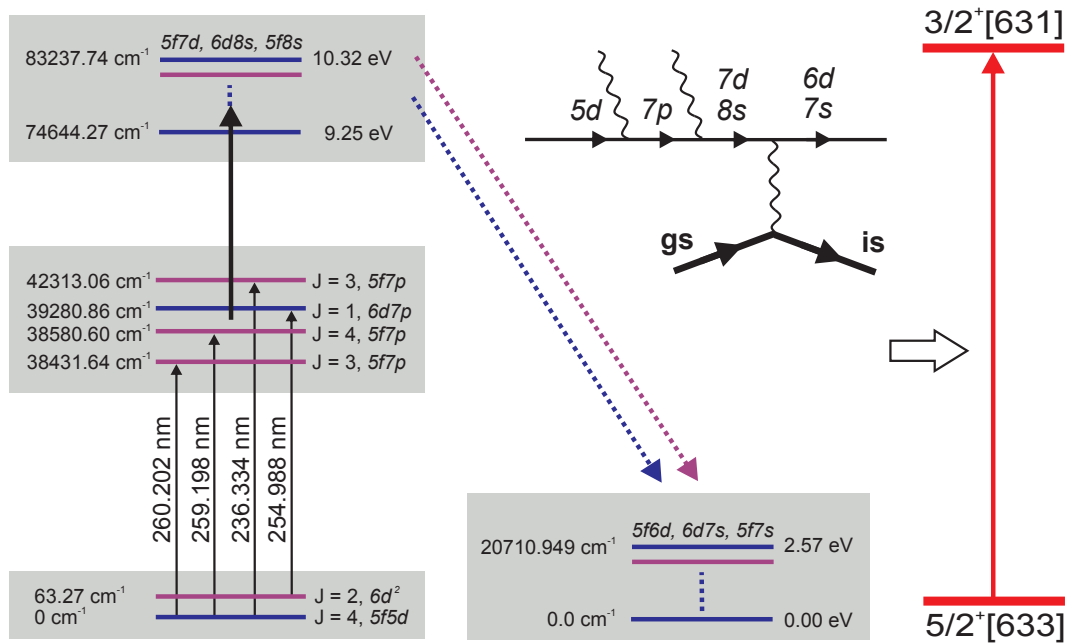

Figure 7.1: **Scheme of the NETP process.** Th^{2+} ions are excited from two initial levels via four intermediate levels to the energy range from 9.25 eV to 10.32 eV. Levels of odd parity are depicted with blue lines, levels of even parity with purple lines. These levels can couple to low-lying states up to 2.57 eV via M1/E2 transitions to excite the nucleus (red transition on the right) by the electronic bridge mechanism. A Feynman diagram of the process is shown in the upper center.
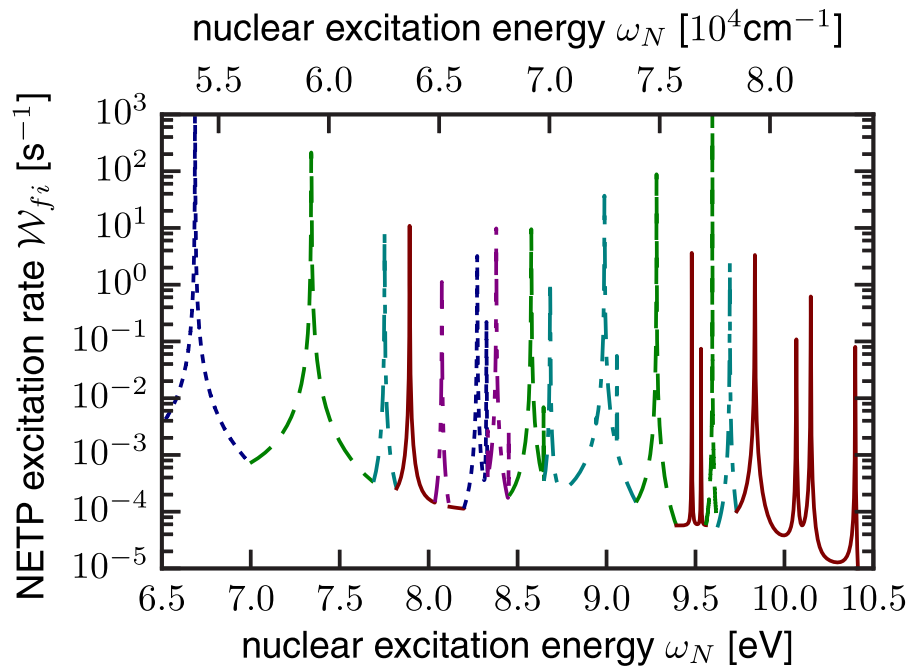
Figure 7.2: **Expected rate of the nuclear excitation via the NETP process for selected high-lying levels.** The predicted excitation rate is depicted as a function of the isomer energy for the high-lying levels 74644_2 (dotted blue line), 78333_2 (dash-double-dotted purple line), 79916_2 (dashed green line), 83237_2 (dash-dotted cyan line) and 84374_3 (red solid). The figure is adapted from Ref. [33].

7.1 NETP experiment

The measurements are conducted using the PTB trap and ^{229}Th^{2+} ions are loaded as described in Ch. 3. The electronic levels in the energy range between 9.25 eV and 10.32 eV are accessed via two-step excitations using two frequency tripled pulsed Ti:Sa lasers (Sirah, Credo). Both lasers produce pulses with a duration of 10 ns at a repetition rate of 1 kHz and an average pulse power in the third harmonic of about 100 W.

Four intermediate levels (Tab. A.2) and 15 high-lying levels (Tab. A.3) can be excited, determined by selection rules and the tuning range of the Ti:Sa lasers from 710 nm to 900 nm. All transitions are first excited in ^{232}Th^{2+} ions to obtain necessary experimental parameters, namely saturation power of each excitation and the detection efficiency for fluorescence decay from the upper levels. Fluorescence of the intermediate levels is detected on decay channels in the wavelength range from 300 nm to 500 nm using a PMT (Hamamatsu, R647) with a 300 nm long pass interference filter to block stray light from the UV pulses (see Fig. 7.3a). The observed linewidth is a convolution of the Doppler-broadened transition and the averaged laser spectrum, which consists of several longitudinal modes (see Fig. 7.4). VUV fluorescence from all high-lying levels is detected using a solar blind PMT (Hamamatsu, R6835) together with a VUV filter (transmission window 140 ± 30 nm) (see Fig. 7.3b).

Employing the obtained experimental parameters, excitation of the high-lying states is performed with ^{229}Th^{2+} ions to search for nuclear excitation. Two-step hyperfine spectroscopy of the $63_2 \rightarrow 20711_1 \rightarrow 29300_0$ transition using ECDLs is performed in parallel as a method to detect HFS components of the isomer, employing the results from Ch. 5. A scheme of the optical setup is shown in Fig. 7.5. The wavelengths of the 484 nm and the 1164 nm laser are chosen to excite the isomer transition $F^m = 5/2 \rightarrow 3/2 \rightarrow 3/2$ (resonance i4 in Fig. 5.11). The 1164 nm laser is set to scan in a narrow range around the resonance frequency to distinguish a possible signal from the background (see Fig. 7.6), with a single scan taking ≈ 60 s of measurement time. Data is taken and averaged for up to three weeks per high-lying state to increase the SNR. Drifting of the 1164 nm laser frequency out of the scan range during the measurements is corrected with respect to the reference cavity.
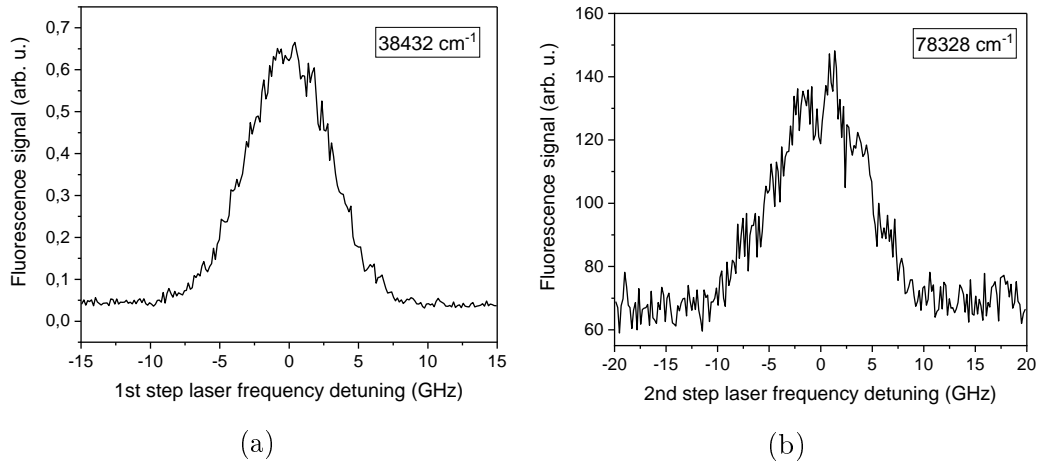
(a)

(b)

Figure 7.3: **Fluorescence of the two excitation steps using ^{232}Th^{2+} ions.** Fluorescence of the 38432 cm^{-1} level (a) and the high-lying level 78328 cm^{-1} (b). All intermediate and high-lying levels are first investigated using ^{232}Th^{2+} ions to determine the required saturation power.
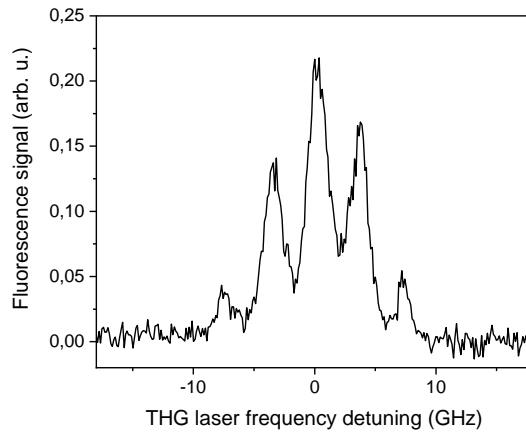

Figure 7.4: **Example of the titanium-sapphire laser spectrum.** The spectra of the employed pulsed Ti:Sa lasers consist of several longitudinal modes. The shown spectrum is recorded in a two-step excitation scheme using ^{232}Th^{+} ions and the transition $0_{3/2} \rightarrow 24874_{5/2}$ as the first step, excited by 402 nm radiation from an ECDL. The emission spectrum of the Ti:Sa laser strongly depends on the laser frequency and adjustment.
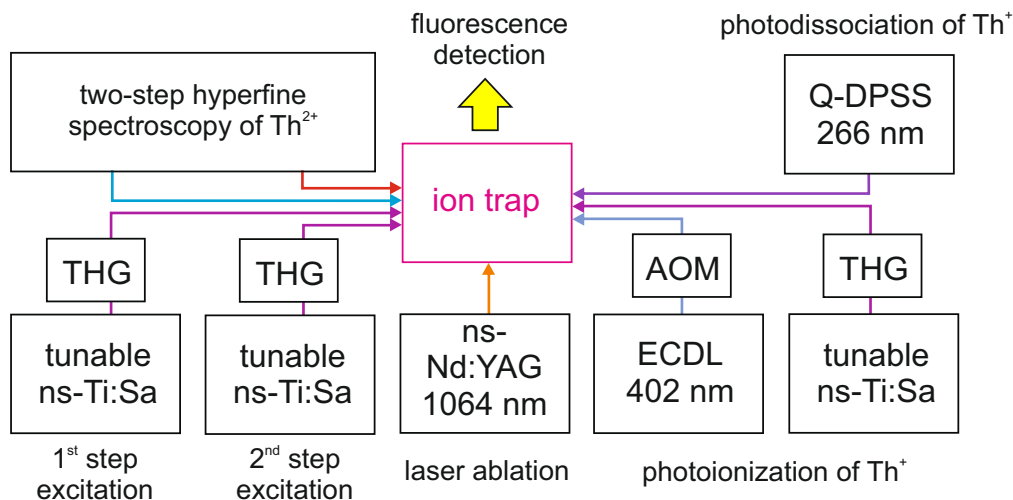
Figure 7.5: **Scheme of the optical setup.** The optical setup is similar to Fig. 5.6, but includes the two frequency tripled (THG) pulsed Ti:Sa lasers to drive the two-step transition to high-lying levels. The nuclear state detection via two-step hyperfine spectroscopy using lasers at 484 nm and 1164 nm is collectively represented by the box in the upper left corner.

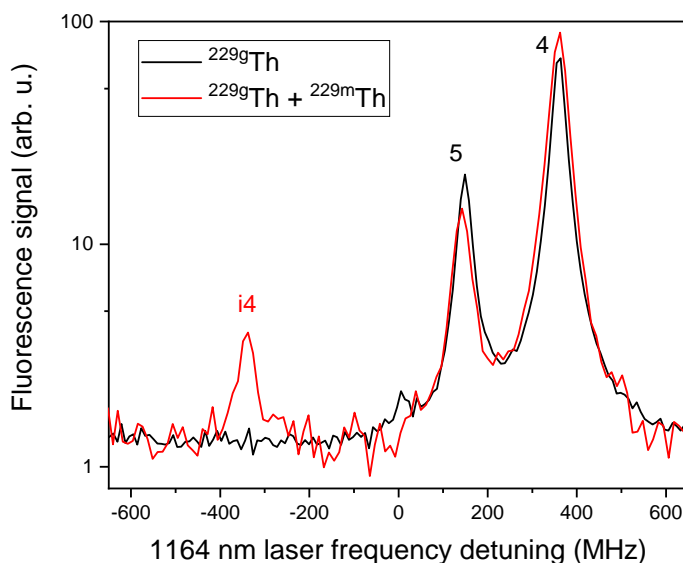Figure 7.6: **Selected two-step hyperfine excitation for nuclear state detection.** The isomer transition i4 ($F^m = 5/2 \rightarrow 3/2 \rightarrow 3/2$) is sufficiently isolated with a distance of 350 MHz to the next nuclear ground state resonance. The spectrum recorded with ions from the ^{233}U recoil source is shown in red, the same spectrum recorded with ions from laser ablation is shown in black.

7.2 Detection limit

For the integrated time of the experiment no signal of the isomeric state is observed. Therefore, only a limit on the detectable NETP excitation rate via the selected electronic levels can be given. To this end, the achieved SNR of the recorded HFS is compared with a reference measurement using ions loaded from the ^{233}U recoil source (see Fig. 7.6). The reference signal has therefore a known isomer population of about 2 %. With this comparison, an upper limit on the average relative population of the isomeric state can be given, which would be detectable with a SNR of 1.

For all selected high-lying levels, a corresponding limit of $3 \cdot 10^{-4}$ is achieved. Assuming that the decay rate Γ_{is} of the isomeric state is only determined by its natural lifetime of $\approx 3000\,$s, an upper limit on the excitation rate $W_{ex} \leq 10^{-7}\,\text{s}^{-1}$ can be given, using the steady state condition $N_{is}/N_{gr} \approx W_{ex}/\Gamma_{is}$. N_{gr} and N_{is} are the ground state and isomeric state population.

In the theoretical analysis of the NETP process in Ref. [33], 100 % of the ions in the nuclear ground state were assumed to populate the excited electronic state. However, the effective excitation time in the experiments is $10^{-5}\,$s during one second, given by the Ti:Sa laser pulse duration of $10\,$ns and a repetition rate of $1\,$kHz. The lifetime of the excited electronic state is observed to be $< 5\,$ns. Saturating the two-step excitation also only leads to $\approx 25\,\%$ of the population being in the high-lying electronic state. The experimental limit on the detectable excitation rate has therefore to be multiplied by a factor of $4 \cdot 10^5$ to compare it to the theoretical rate. The resulting minimal detectable excitation rate is $\approx 4 \cdot 10^{-2}\,\text{s}^{-1}$ in terms of the theoretical calculation (see Fig. 7.2).

For the levels 74644_2, 78333_2 and 79916_2 a higher SNR ratio is achieved, giving a limit for the excitation rate of $\approx 10^{-2}\,\text{s}^{-1}$. Comparing this limit to the theoretical prediction of the excitation rate in Ref. [33] shows that only isomeric energy values close to the electronic resonances can be excluded (see Fig. 7.7).
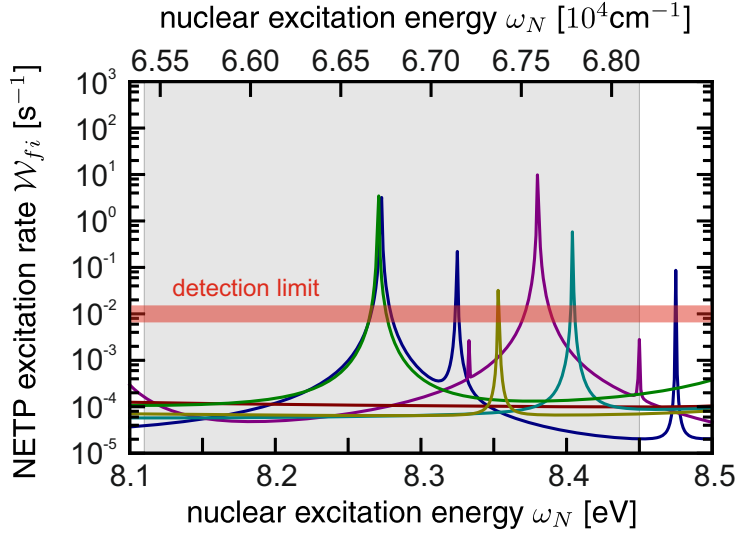
Figure 7.7: **Detection limit for the NETP excitation rate.** An excerpt of Fig. 7.2 is shown with the achieved detection limit (red bar). The limit represents a nuclear excitation rate, which would be visible with a SNR of 1. The gray area marks the 1σ-uncertainty of the isomer energy value measured in Ref. [9]. The figure is adapted from Ref. [114].

7.3   Further steps

The lowest exclusion limit is achieved with a measurement time of about three weeks per selected electronic state. To be able to detect an isomeric signal for any nuclear excitation energy inside the current 3σ-range, the SNR has to be improved by two orders of magnitude. This is not feasible with the current experimental setup, since it would require to extend the measurement time by four orders of magnitude. To improve future experiments, the hyperfine detection scheme could be changed from scanning over the isomeric resonance frequency to measuring only the fluorescence at two frequency points, one on the resonance and one off resonance. This would speed up the data acquisition by a factor of about 30, since currently 75 data points are recorded per scan. To this end, an improved frequency stabilization has to be employed. This can be achieved by locking the lasers to the rubidium reference (see Ch. 4) via a transfer cavity (see, e.g., Ref. [115]), instead of using a wavelength meter. Additionally, the average population time of the high-lying level could be extended by using cw lasers instead of the currently used pulsed lasers.

Chapter 8

Conclusion and outlook

The main result of this thesis is the first measurement of the hyperfine structure of $^{229}\text{Th}^{2+}$ in the isomeric nuclear state and the extraction of fundamental nuclear properties of the isomer [26]. The determination of the magnetic dipole moment μ, the electric quadrupole moment Q and the mean squared charge radius of the isomer allows one to calculate now the hyperfine structure of ^{229m}Th for any electronic transition, when its hyperfine constants and isotope shift are known for the nuclear ground state. This facilitates the sensitive and non-destructive electronic-nuclear double resonance detection [8] of the isomer also for other systems than Th^{2+}. This is particularly important for future experiments towards the development of a nuclear clock, when the long radiative lifetime of the isomer makes it difficult to detect photons emitted in the decay of the isomer. The results for the intrinsic electric quadrupole moment and charge radius of the isomer were used to estimate the sensitivity of such a clock to the temporal variation of the fine structure constant α.

Within the scope of this thesis, the hyperfine structures of selected transitions in $^{229}\text{Th}^+$ and $^{229}\text{Th}^{2+}$ as well as their isotope shifts with respect to ^{232}Th have been measured. The results of this measurements have been used by collaborating theoretical groups to improve the value of the nuclear ground state mean squared charge radius [53] and to confirm precision atomic structure calculations [89]. All hyperfine splitting constants that have been measured in this thesis are shown in Tab. A.1.

Furthermore, the excitation of the nucleus via an electronic bridge process in $^{229}\text{Th}^{2+}$ has been investigated. Since so far no excitation has been observed,

detection limits for an observable excitation rate have been given, based on the achieved SNR.

Results of this thesis will be employed in an upcoming extension of an experiment searching for electronic bridge excitation in Th^+. In previous measurements, only even parity high-lying levels have been investigated [116]. In the new experiment, based on three-photon excitation, levels of odd parity in the energy range of the isomer will be excited to search for nuclear excitation. This experiment will now also employ hyperfine spectroscopy to detect ions in the isomeric state. To this end, the two-step excitation $0_{3/2} \rightarrow 24874_{5/2} \rightarrow 49960_{7/2}$, described in Ch. 4, will be used. Based on the determined isotope shift and hyperfine constants of the $49960_{7/2}$ level and the isomeric nuclear properties, the frequencies of the expected isomeric hyperfine resonances have been calculated and a suitable detection scheme has been chosen (see Fig. 8.1). In parallel, improvements of the Th^{2+} experiment discussed in Ch. 7 are in preparation.

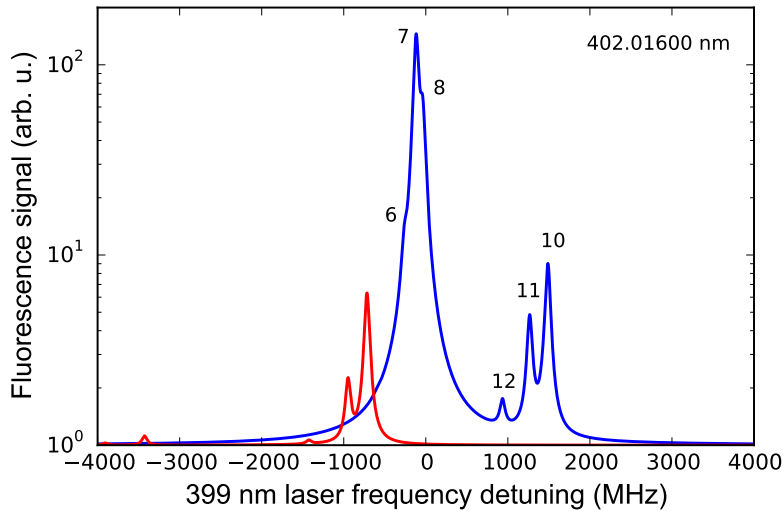Figure 8.1: **Nuclear state detection via hyperfine spectroscopy in Th^+.** The two-step excitation $0_{3/2} \rightarrow 24874_{5/2} \rightarrow 49960_{7/2}$ in $^{229}Th^+$ can be used to distinguish ions in the nuclear ground state (blue) from ions in the isomeric state (red). In the presented calculated spectra, a 2 % fractional population of the isomeric state is assumed. Resonances are labeled according to Tab. 4.1.

The recently started 'ThoriumNuclearClock' collaboration, consisting of groups from TU Wien, LMU, University of Delaware and PTB, aims for the direct optical excitation of the nuclear transition. To this goal, three VUV laser systems are in preparation. The groups at TU Wien and LMU will employ two frequency combs with high harmonic generation to achieve linewidths below $1\,\mathrm{kHz}$ at $150\,\mathrm{nm}$.

At PTB, a laser system to produce VUV radiation based on a four-wave difference mixing process (see, e.g., Ref. [117]) is currently set up. In the four-wave mixing process, three frequencies are coupled in a non-linear medium to generate a fourth frequency. A corresponding scheme is shown in Fig. 8.2.
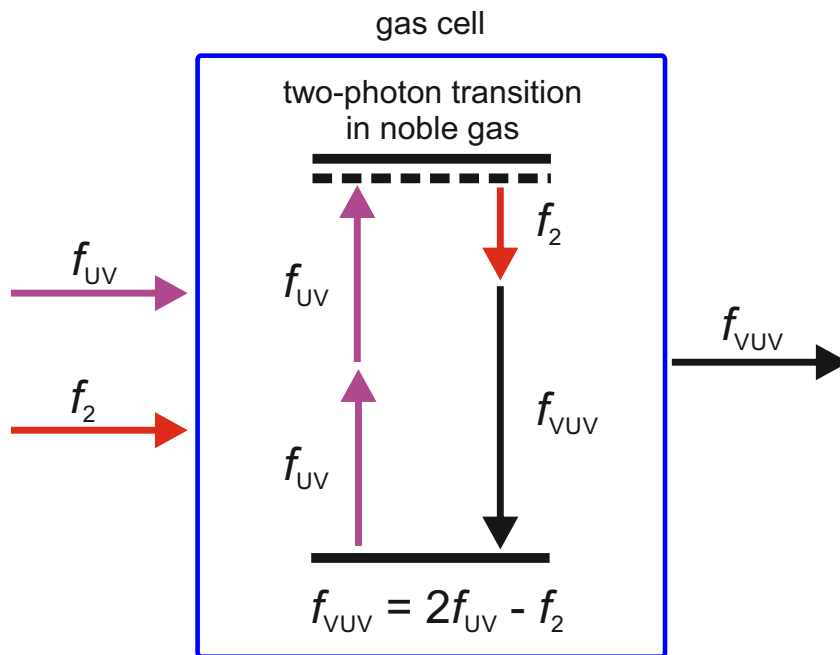
Figure 8.2: **Scheme of a four-wave difference mixing process.** Laser radiation with the frequency f_{UV} drives a near-resonant two-photon transition in a non-linear medium, in this case a noble gas. Since the de-excitation has to occur also via two photons due to symmetry, supplying one of these photons via laser radiation at f_2 yields VUV radiation with $f_{VUV} = 2f_{UV} - f_2$.

In the presented scheme, radiation of the frequency f_{UV} is tuned close to a two-photon transition in the non-linear medium. The de-excitation has also to occur via two photons due to the inversion symmetry of the atom [118]. By applying additional laser radiation with the frequency f_2, the system can

be stimulated to emit photons with the frequency $f_{VUV} = 2f_{UV} - f_2$. By tuning the frequency f_2, VUV radiation over a wide frequency range can be produced. The efficiency of this process strongly depends on the phases of the three wavelengths. Phase matching can be achieved by adjusting the pressure of the noble gas and by selecting a suitable mixture of different gases, which therefore maximizes the efficiency of the conversion.
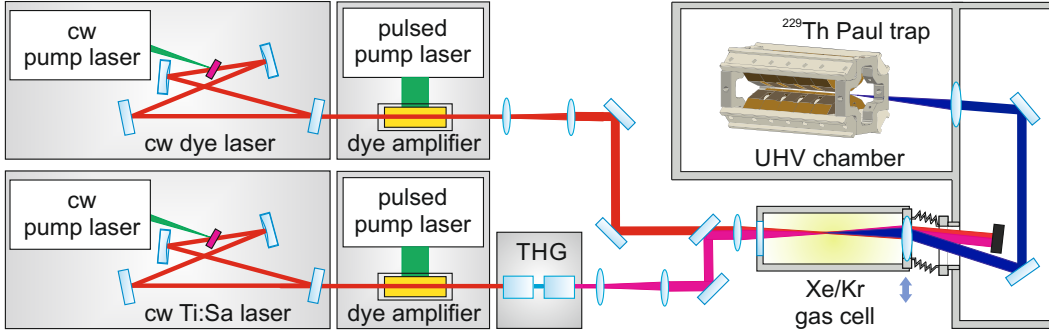

Figure 8.3: **Schematic of the planned laser setup for four-wave mixing.** Two tunable cw lasers (dye or Ti:Sa laser) each seed a pulsed dye amplifier. The radiation of one amplifier is frequency tripled to generate photons of f_{UV} to drive a near resonant two-photon transition in xenon or krypton gas. Difference mixing with the fundamental or second harmonic frequency (not shown) of the second amplifier yields the VUV radiation for nuclear excitation in the ion trap.

In the planned configuration, f_{UV} will be produced by frequency tripling of a pulsed dye amplifier, which is seeded with a cw Ti:Sa or dye laser. A second tunable cw laser produces radiation of the frequency f_2 which also undergoes pulsed amplification and optional second harmonic generation (see Fig. 8.3). By selecting different two-photon transitions in xenon or krypton, VUV radiation with a photon energy from 7.4 eV to 10.2 eV can be achieved. The system is planned to produce VUV pulses with $10^{13} - 10^{14}$ photons per pulse in the energy range from 8.0 eV to 8.5 eV and a Fourier-transform-limited linewidth of less than 1 GHz, resulting in a spectral power density of 10^6 photons/Hz·s. This can be treated as a broadband radiation source with respect to the narrow nuclear transition. Assuming a beam waist of 0.25 mm, the excitation rate can therefore be estimated based on the Einstein B coefficient (see, e.g., Ref. [119] to be about $5 \cdot 10^{-7}\,\mathrm{s}^{-1}$ per ion.

As a first stage, the laser will be used to search for excitation of the isomeric state in Th^{2+} ions using the ablation loaded ion trap introduced in Ch. 3. In a later experiment, it is planned to excite sympathetically cooled Th^{3+} ions, which are embedded in a Coulomb crystal of laser-cooled Sr^+ ions. To this end, a new ion trap loaded with Th^{3+} ions from a ^{233}U recoil source is currently in development.

Appendix

Table A.1: **Hyperfine splitting constants A and B that have been measured in this thesis.** Values are listed with their 1σ-uncertainty. If no uncertainty is given, the value represents a quantitative estimate, based on a not completely resolved HFS.

Ion	Energy (cm^{-1})	Electronic level configuration	J^{Π}	A (MHz)	B (MHz)
$^{229}\text{Th}^+$	49960	$5f^2 6d + 5f6d7p$	$7/2^+$	-7.9(3.5)	-1107(39)
$^{233}\text{U}^+$	289	$5f^3 6d7s$	$11/2^-$	-301(6)	2860(320)
	25164	$5f^2 6d^2 7s$	$13/2^+$	371(8)	215(600)
$^{229}\text{Th}^{2+}$	0	$5f6d$	4^-	80	3500
	63	$6d^2$	2^+	151(8)	73(27)
	20711	$5f6d$	1^-	88(4)	897(14)
	21784	$5f^2$	4^+	25	215
$^{229m}\text{Th}^{2+}$	63	$6d^2$	2^+	-263(29)	53(65)
	20711	$5f6d$	1^-	-151(22)	498(15)

Table A.2: **Excitation levels of Th^{2+}, used as intermediate levels for the NETP experiment.** Level energies and classifications are taken from Ref. [120].

Energy (cm^{-1})	Electronic configuration	Angular momentum J
38431.64	5f7p	3
38580.6	5f7p	4
39280.86	6d7p	1
42313.055	5f7p	3

Table A.3: **Excitation levels of Th^{2+}, used as high-lying levels for the NETP experiment.** Level energies and classifications are taken from Ref. [112].

Energy (cm^{-1})	Electronic configuration	Angular momentum J
74644.27	5f8s	2
74784.31	5f8s	3
78327.71	5f7d	3
78332.73	5f7d	2
78417.26	5f7d	4
78929.56	5f8s	4
79082.84	5f8s	3
79329.56	5f7d	4
79646.36	5f7d	3
79915.98	5f7d	2
80137.22	5f7d	5
81706.37	6d8s	1
82348.62	5f7d	4
82827.05	5f7d	3
83237.74	5f7d	2

Table A.4: **Low-lying states of Th^{2+}.** These states can couple to the states listed in Tab. A.3 to form M1/E2 transitions with energies from 7.14 eV to 10.46 eV. Level energies and classifications are taken from Refs. [112; 120; 121].

Energy (cm^{-1})	Electronic configuration	Angular momentum J
0	5f.6d	4
510.758	5f6d	2
2527.095	5f7s	3
3181.502	5f7s	2
3188.301	5f6d	4
4489.641	5f6d	5
4826.826	5f6d	3
5060.544	5f6d	3
6288.221	5f6d	2
6310.807	5f7s	4
7500.605	5f7s	3
7921.088	5f6d	1
8141.749	5f6d	4
8436.824	5f6d	6
8980.557	5f6d	4
10180.766	5f6d	2
10741.15	5f6d	3
11123.179	5f6d	1
11276.807	5f6d	5
13208.214	5f6d	2
15453.411	5f6d	3
19009.908	5f6d	5
20710.949	5f6d	1

Bibliography

[1] Riehle, F. *Frequency Standards* (Wiley-VCH, 2004).

[2] Derevianko, A. *Journal of Physics: Conference Series* **723**, (2016) 012043.

[3] Sanner, C., Huntemann, N., Lange, R., Tamm, C., Peik, E., Safronova, M. S., and Porsev, S. G. *Nature* **567**(7747), (2019) 204–208.

[4] Peik, E. *Nuclear Physics B - Proceedings Supplements* **203-204**, (2010) 18 – 32. Masses and Constants. Proceedings of the 48th Internationale Universitätswochen für Theoretische Physik.

[5] Ramsey, N. F. *Metrologia* **42**(3), (2005) 1–3.

[6] Brewer, S. M., Chen, J.-S., Hankin, A. M., Clements, E. R., Chou, C. W., Wineland, D. J., Hume, D. B., and Leibrandt, D. R. *Phys. Rev. Lett.* **123**(17), (2019) 033201.

[7] Oelker, E., Hutson, R. B., Kennedy, C. J., Sonderhouse, L., Bothwell, T., Goban, A., Kedar, D., Sanner, C., Robinson, J. M., Marti, G. E., Matei, D. G., Legero, T., Giunta, M., Holzwarth, R., Riehle, F., Sterr, U., and Ye, J. *Nature Photonics* **13**(10), (2019) 714–719.

[8] Peik, E. and Tamm, C. *Europhys. Lett.* **61**(2), (2003) 181–186.

[9] Seiferle, B., von der Wense, L., Bilous, P. V., Amersdorffer, I., Lemell, C., Libisch, F., Stellmer, S., Schumm, T., Düllmann, C. E., Pálffy, A., and Thirolf, P. G. *Nature* **573**(7773), (2019) 243–246.

[10] Ponce, F., Swanberg, E., Burke, J., Henderson, R., and Friedrich, S. *Phys. Rev. C* **97**(5), (2018) 054310.

[11] Asaro, F. and Perlman, I. *Phys. Rev.* **107**(1), (1957) 318.

[12] Beck, B. R., Becker, J. A., Beiersdorfer, P., Brown, G. V., Moody, K. J., Wilhelmy, J. B., Porter, F. S., Kilbourne, C. A., and Kelley, R. L. *Phys. Rev. Lett.* **98**, (2007) 142501.

[13] Campbell, C. J., Radnaev, A. G., Kuzmich, A., Dzuba, V. A., Flambaum, V. V., and Derevianko, A. *Phys. Rev. Lett.* **108**, (2012) 120802.

[14] Rellergert, W. G., DeMille, D., Greco, R. R., Hehlen, M. P., Torgerson, J. R., and Hudson, E. R. *Phys. Rev. Lett.* **104**(20), (2010) 200802.

[15] Kazakov, G. A., Litvinov, A. N., Romanenko, V. I., Yatsenko, L. P., Romanenko, A. V., Schreitl, M., Winkler, G., and Schumm, T. *New Journal of Physics* **14**(8), (2012) 083019.

[16] Flambaum, V. V. *Phys. Rev. Lett.* **97**(9), (2006) 092502.

[17] von der Wense, L. *On the Direct Detection of* ^{229m}Th. Springer Theses (Springer International Publishing, 2018).

[18] Kroger, L. A. and Reich, C. W. *Nuclear Physics A* **259**(1), (1976) 29 – 60.

[19] Burke, D. G., Garrett, P. E., Qu, T., and Naumann, R. A. *Phys. Rev. C* **42**, (1990) 499–501.

[20] Reich, C. W. and Helmer, R. G. *Phys. Rev. Lett.* **64**, (1990) 271–273.

[21] Helmer, R. G. and Reich, C. W. *Phys. Rev. C* **49**, (1994) 1845–1858.

[22] Beck, B. R., Wu, C. Y., Beiersdorfer, P., Brown, G. V., Becker, J. A., Moody, K. J., Wilhelmy, J. B., Porter, F. S., Kilbourne, C. A., and Kelley, R. L. Improved value for the energy splitting of the ground-state doublet in the nucleus ^{229m}Th. Technical report, Lawrence Livermore National Laboratory (2009). LLNL-PROC-415170.

[23] Jeet, J., Schneider, C., Sullivan, S. T., Rellergert, W. G., Mirzadeh, S., Cassanho, A., Jenssen, H., Tkalya, E. V., and Hudson, E. R. *Phys. Rev. Lett.* **114**(25), (2015) 253001.

[24] von der Wense, L., Seiferle, B., Laatiaoui, M., Neumayr, J. B., Maier, H.-J., Wirth, H.-F., Mokry, C., Runke, J., Eberhardt, K., Düllmann, C. E., Trautmann, N. G., and Thirolf, P. G. *Nature* **533**, (2016) 47.

[25] Köhler, S., Deienberger, R., Eberhardt, K., Erdmann, N., Herrmann, G., Huber, G., Kratz, J., Nunnemann, M., Passler, G., Rao, P. M., Riegel, J., Trautmann, N., and Wendt, K. *Spectrochimica Acta Part B: Atomic Spectroscopy* **52**(6), (1997) 717–726.

[26] Thielking, J., Okhapkin, M. V., Głowacki, P., Meier, D. M., von der Wense, L., Seiferle, B., Düllmann, C. E., Thirolf, P. G., and Peik, E. *Nature* **556**(7701), (2018) 321–325.

[27] Yamaguchi, A., Muramatsu, H., Hayashi, T., Yuasa, N., Nakamura, K., Takimoto, M., Haba, H., Konashi, K., Watanabe, M., Kikunaga, H., Maehata, K., Yamasaki, N. Y., and Mitsuda, K. *Phys. Rev. Lett.* **123**(22), (2019) 222501.

[28] Masuda, T., Yoshimi, A., Fujieda, A., Fujimoto, H., Haba, H., Hara, H., Hiraki, T., Kaino, H., Kasamatsu, Y., Kitao, S., Konashi, K., Miyamoto, Y., Okai, K., Okubo, S., Sasao, N., Seto, M., Schumm, T., Shigekawa, Y., Suzuki, K., Stellmer, S., Tamasaku, K., Uetake, S., Watanabe, M., Watanabe, T., Yasuda, Y., Yamaguchi, A., Yoda, Y., Yokokita, T., Yoshimura, M., and Yoshimura, K. *Nature* **573**(7773), (2019) 238–242.

[29] Peik, E. and Okhapkin, M. *Comptes Rendus Physique* **16**(5), (2015) 516 – 523. The measurement of time / La mesure du temps.

[30] Herrera-Sancho, O. A., Okhapkin, M. V., Zimmermann, K., Tamm, C., Peik, E., Taichenachev, A. V., Yudin, V. I., and Głowacki, P. *Phys. Rev. A* **85**, (2012) 033402.

[31] Okhapkin, M. V., Meier, D. M., Peik, E., Safronova, M. S., Kozlov, M. G., and Porsev, S. G. *Phys. Rev. A* **92**, (2015) 020503.

[32] Porsev, S. G., Flambaum, V. V., Peik, E., and Tamm, C. *Phys. Rev. Lett.* **105**, (2010) 182501.

[33] Müller, R. A., Volotka, A. V., and Surzhykov, A. *Phys. Rev. A* **99**(4), (2019) 042517.

[34] Mayer-Kuckuk, T. *Physik der Atomkerne: eine Einführung* (Teubner, 1974).

[35] Sobelmann, I. I. *Atomic Spectra and Radiative Transitions* (Springer, 1992), 2nd edition.

[36] Cowan, R. D. *The theory of atomic structure and spectra.* 3 (Univ of California Press, 1981).

[37] Nilsson, S. G. *Dan. Mat. Fys. Medd.* **29**(CERN-55-30), (1955) 1–69.

[38] Löbner, K. E. G., Vetter, M., and Hönig, V. Nuclear intrinsic quadrupole moments and deformation parameters. Technical report, Univ., Freiburg i. B. Technische Hochschule, Munich (1970).

[39] Minkov, N. and Pálffy, A. *Phys. Rev. Lett.* **118**(21), (2017) 212501.

[40] Möller, P., Nix, J. R., Myers, W. D., and Swiatecki, W. J. *At. Data Nucl. Data Tabl.* **59**, (1995) 185–381.

[41] Angeli, I. and Marinova, K. P. *At. Data Nucl. Data Tables* **99**, (2013) 69–95.

[42] Tkalya, E. V., Schneider, C., Jeet, J., and Hudson, E. R. *Phys. Rev. C* **92**, (2015) 054324.

[43] Schmidt, T. *Zeitschrift für Physik A Hadrons and Nuclei* **106**(5), (1937) 358–361.

[44] Dykhne, A. M. and Tkalya, E. V. *Journal of Experimental and Theoretical Physics Letters* **67**(4), (1998) 251–256.

[45] Bemis, C. E., McGowan, F. K., Ford Jr, J. L. C., Milner, W. T., Robinson, R. L., Stelson, P. H., Leander, G. A., and Reich, C. W. *Physica Scripta* **38**(5), (1988) 657.

[46] Chasman, R. R., Ahmad, I., Friedman, A. M., and Erskine, J. R. *Reviews of Modern Physics* **49**(4), (1977) 833.

[47] Safronova, M. S., Safronova, U. I., Radnaev, A. G., Campbell, C. J., and Kuzmich, A. *Phys. Rev. A* **88**(6), (2013) 060501.

[48] Kopfermann, H. *Kernmomente* (Akademische Verlagsgesellschaft, 1956), 2nd edition.

[49] Pauli, W. *Naturwissenschaften* **12**(37), (1924) 741–743.

[50] Beloy, K. *Phys. Rev. Lett.* **112**(6), (2014) 062503.

[51] Sonnenschein, V., Raeder, S., Hakimi, A., Moore, I. D., and Wendt, K. *Journal of Physics B: Atomic, Molecular and Optical Physics* **45**(16), (2012) 165005.

[52] Meschede, D. (Editor). *Gerthsen Physik* (Springer, 2010), 24th edition.

[53] Safronova, M. S., Porsev, S. G., Kozlov, M. G., Thielking, J., Okhapkin, M. V., Głowacki, P., Meier, D.-M., and Peik, E. *Phys. Rev. Lett.* **121**(21), (2018) 213001.

[54] Tralli, N. and Goertzel, G. *Phys. Rev.* **83**, (1951) 399–404.

[55] Krutov, V. A. and Fomenko, V. N. *Annalen der Physik* **476**(5-6), (1968) 291–302.

[56] Rösel, C., Karpeshin, F. F., David, P., Hänscheid, H., Konijn, J., de Laat, C. T. A. M., Paganetti, H., Risse, F., Sabirov, B., Schaller, L. A., Schellenberg, L., Schrieder, W., and Taal, A. *Zeitschrift für Physik A Hadrons and Nuclei* **345**(4), (1993) 425–426.

[57] Karpeshin, F. F. and Trzhaskovskaya, M. B. *Phys. Rev. C* **95**, (2017) 034310.

[58] Kekez, D., Ljubicic, A., Pisk, K., and Logan, B. A. *Phys. Rev. Lett.* **55**, (1985) 1366–1368.

[59] Morita, M. *Progress of Theoretical Physics* **49**(5), (1973) 1574–1586.

[60] Fujioka, H., Ura, K., Shinohara, A., Saito, T., and Otozai, K. *Zeitschrift für Physik A Atoms and Nuclei* **315**(1), (1984) 121–122.

[61] Seiferle, B., von der Wense, L., and Thirolf, P. G. *Phys. Rev. Lett.* **118**, (2017) 042501.

[62] Ricci, L., Weidemüller, M., Esslinger, T., Hemmerich, A., Zimmermann, C., Vuletic, V., König, W., and Hänsch, T. W. *Optics Communications* **117**(5-6), (1995) 541–549.

[63] Wright, A. G. *The photomultiplier handbook* (Oxford University Press, 2017).

[64] Zimmermann, K. *Experiments Towards Optical Nuclear Spectroscopy With Thorium-229*. Ph.D. thesis, Leibniz Universität Hannover (2010).

[65] Meier, D.-M. *Electronic level structure investigations in Th$^+$ in the energy range of the ^{229}Th isomer*. Ph.D. thesis, Leibniz Universität Hannover (2019).

[66] Herrera-Sancho, O. A., Nemitz, N., Okhapkin, M. V., and Peik, E. *Phys. Rev. A* **88**, (2013) 012512.

[67] Marçalo, J., Leal, J. P., and de Matos, A. P. *International journal of mass spectrometry and ion processes* **157**, (1996) 265–274.

[68] Cornehl, H. H., Wesendrup, R., Diefenbach, M., and Schwarz, H. *Chemistry–A European Journal* **3**(7), (1997) 1083–1090.

[69] De Almeida, K. and Duarte, H. *Organometallics* **29**(17), (2010) 3735–3745.

[70] Gibson, J. K., Haire, R. G., Santos, M., Marçalo, J., and Pires de Matos, A. *The Journal of Physical Chemistry A* **109**(12), (2005) 2768–2781.

[71] Neumayr, J. B. *The buffer-gas cell and the extraction RFQ for SHIP-TRAP*. Ph.D. thesis, Ludwig-Maximilians-Universität München (2004).

[72] von der Wense, L., Seiferle, B., Laatiaoui, M., and Thirolf, P. G. *The European Physical Journal A* **51**(3), (2015) 29.

[73] Vascon, A., Santi, S., Isse, A. A., Reich, T., Drebert, J., Christ, H., Düllmann, C. E., and Eberhardt, K. *Nuclear Instruments and Methods*

in Physics Research Section A: Accelerators, Spectrometers, Detectors and Associated Equipment **696**, (2012) 180–191.

[74] Neumayr, J. B., Thirolf, P. G., Habs, D., Heinz, S., Kolhinen, V. S., Sewtz, M., and Szerypo, J. *Review of scientific instruments* **77**(6), (2006) 065109.

[75] Soti, Z., Magill, J., and Dreher, R. *EPJ Nuclear Sciences & Technologies* **5**, (2019) 6.

[76] Kälber, W., Rink, J., Bekk, K., Faubel, W., Göring, S., Meisel, G., Rebel, H., and Thompson, R. C. *Zeitschrift für Physik A Atomic Nuclei* **334**(1), (1989) 103–108.

[77] Kälber, W., Meisel, G., Rink, J., and Thompson, R. C. *Journal of Modern Optics* **39**(2), (1992) 335–347.

[78] Demtröder, W. *Laser spectroscopy: vol. 2: experimental techniques*, volume 2 (Springer Science & Business Media, 2008).

[79] Lamb Jr, W. E. *Phys. Rev.* **134**(6A), (1964) A1429.

[80] Herrera-Sancho, O.-A. *Laser excitation of 8-eV electronic states in Th$^+$: A first pillarof the electronic bridge toward excitation of the Th-229 nucleus.* Ph.D. thesis, Leibniz Universität Hannover (2012).

[81] Bjorkholm, J. E. and Liao, P. F. *Phys. Rev. A* **14**(2), (1976) 751.

[82] McCarron, D. J., King, S. A., and Cornish, S. L. *Measurement science and technology* **19**(10), (2008) 105601.

[83] OriginLab Corporation, Northampton, MA, USA. Origin 2018G.

[84] Press, W. H., Teukolsky, S. A., Vetterling, W. T., and Flannery, B. P. *Numerical Recipes in C - The Art of Scientific Computing* (Cambridge University Press, 1997), 2nd edition.

[85] Palmer, B. A., Keller, R. A., and Engleman Jr, R. Atlas of uranium emission intensities in a hollow cathode discharge. Technical report, Los Alamos Scientific Lab. (1980).

[86] Gangrskij, Y. P., Zemlyanoj, S., Markov, B., Kolesnikov, N., Kul'dzhanov, B., and Marinova, K. Hyperfine splitting of the optical lines in the odd isotopes of uranium. Technical report, Joint Inst. for Nuclear Research (1996).

[87] Stone, N. J. Table of nuclear magnetic dipole and electric quadrupole moments. Technical report, International Atomic Energy Agency (2014).

[88] Zumbro, J. D., Shera, E. B., Tanaka, Y., Bemis Jr, C. E., Naumann, R. A., Hoehn, M. V., Reuter, W., and Steffen, R. M. *Phys. Rev. Lett.* **53**(20), (1984) 1888.

[89] Müller, R. A., Maiorova, A. V., Fritzsche, S., Volotka, A. V., Beerwerth, R., Głowacki, P., Thielking, J., Meier, D.-M., Okhapkin, M., Peik, E., and Surzhykov, A. *Phys. Rev. A* **98**(2), (2018) 020503.

[90] Sydoryk, I., Bezuglov, N. N., Beterov, I. I., Miculis, K., Saks, E., Janovs, A., Spels, P., and Ekers, A. *Phys. Rev. A* **77**(4), (2008) 042511.

[91] Thielking, J., Okhapkin, M. V., Głowacki, P., Meier, D. M., von der Wense, L., Seiferle, B., Düllmann, C. E., Thirolf, P. G., and Peik, E. Hyperfine spectroscopy data Th-229 + Th-229m (2018). `https://zenodo.org/communities/nuclock/`.

[92] Blaise, J., Fred, M., and Gutmacher, R. G. Atomic spectrum of plutonium. Technical report, Argonne National Lab. (1984).

[93] Blaise, J. and Wyart, J.-F. Database of Selected Constants, Energy Levels and Atomic Spectra of Actinides (2017). `http://web2.lac.u-psud.fr/lac/Database/Contents.html`.

[94] Wright, T. G. and Breckenridge, W. H. *The Journal of Physical Chemistry A* **114**(9), (2010) 3182–3189.

[95] Brahms, N., Tscherbul, T. V., Zhang, P., Kłos, J., Forrey, R. C., Au, Y. S., Sadeghpour, H. R., Dalgarno, A., Doyle, J. M., and Walker, T. G. *Phys. Chem. Chem. Phys.* **13**(42), (2011) 19125–19141.

[96] Liao, P. F., Bjorkholm, J. E., and Berman, P. R. *Phys. Rev. A* **21**(6), (1980) 1927.

[97] Bohr, A. and Weisskopf, V. F. *Phys. Rev.* **77**(1), (1950) 94.

[98] Büttgenbach, S. *Hyperfine Interactions* **20**(1), (1984) 1–64.

[99] Gerstenkorn, S., Luc, P., Verges, J., Englekemeir, D. W., Gindler, J. E., and Tomkins, F. S. *Journal de Physique* **35**(6), (1974) 483–495.

[100] Campbell, C. J., Radnaev, A. G., and Kuzmich, A. *Phys. Rev. Lett.* **106**, (2011) 223001.

[101] Litvinova, E., Feldmeier, H., Dobaczewski, J., and Flambaum, V. *Phys. Rev. C* **79**(6), (2009) 064303.

[102] Minkov, N. and Pálffy, A. *Phys. Rev. Lett.* **122**(16), (2019) 162502.

[103] Tkalya, E. V. *Phys. Rev. Lett.* **106**(16), (2011) 162501.

[104] Milne, E. A. *Proceedings of the Royal Society of London. Series A. Mathematical and Physical Sciences* **158**(894), (1937) 324–348.

[105] Dirac, P. A. M. *Nature* **139**(3512), (1937) 323–323.

[106] Hayes, A. C., Friar, J. L., and Möller, P. *Phys. Rev. C* **78**(2), (2008) 024311.

[107] Berengut, J. C., Dzuba, V. A., Flambaum, V. V., and Porsev, S. G. *Phys. Rev. Lett.* **102**(21), (2009) 210801.

[108] Flambaum, V. V. and Dzuba, V. A. *Canadian Journal of Physics* **87**(1), (2009) 25–33.

[109] Barci, V., Ardisson, G., Barci-Funel, G., Weiss, B., El Samad, O., and Sheline, R. K. *Phys. Rev. C* **68**(3), (2003) 034329.

[110] Karpeshin, F. F., Band, I. M., Trzhaskovskaya, M. B., and Listengarten, M. A. *Physics Letters B* **372**(1), (1996) 1 – 7.

[111] Matinyan, S. *Physics reports* **298**(4), (1998) 199–249.

[112] Wyart, J.-F. and Kaufman, V. *Physica Scripta* **24**(6), (1981) 941.

[113] Klinkenberg, P. F. A. *Physica* **16**(7), (1950) 618 – 650.

[114] Müller, R. A. -. Private comm., unpublished.

[115] Lindsay, B. G., Smith, K. A., and Dunning, F. B. *Review of scientific instruments* **62**(6), (1991) 1656–1657.

[116] Meier, D.-M., Thielking, J., Głowacki, P., Okhapkin, M. V., Müller, R. A., Surzhykov, A., and Peik, E. *Phys. Rev. A* **99**, (2019) 052514.

[117] Hanna, S. J., Campuzano-Jost, P., Simpson, E. A., Robb, D. B., Burak, I., Blades, M. W., Hepburn, J. W., and Bertram, A. K. *International Journal of Mass Spectrometry* **279**(2-3), (2009) 134–146.

[118] Demtröder, W. *Laser spectroscopy 1: basic principles* (Springer, 2014).

[119] Hilborn, R. C. *American Journal of Physics* **50**(11), (1982) 982–986.

[120] De Bruin, T. L. and Klinkenberg, P. F. A. In *Proc. Koninkl. Ned. Akad. Wetenschap.*, volume 43, pages 581–590 (1940).

[121] De Bruin, T. L., Klinkenberg, P. F. A., and Schuurmans, P. *Zeitschrift für Physik* **118**(1-2), (1941) 58–87.

Danksagung

Zuallererst möchte ich mich besonders bei meinem Doktorvater Ekkehard Peik bedanken. Ich danke ihm sowohl für die Möglichkeit, an diesem spannenden und herausvordernden Projekt mitwirken zu dürfen, als auch für viele hilfreiche Ratschläge, ein jederzeit offenes Ohr und das in mich gesetze Vertrauen während meiner bisherigen Zeit an der PTB.

Ein großer Dank gilt auch Maksim V. Okhapkin. Auf seine uneingeschränkte Unterstützung und Hilfsbereitschaft konnte ich sowohl im, als auch außerhalb des Labors jederzeit zählen und ohne ihn währe diese Arbeit nicht möglich gewesen. Ich bedanke mich auch für das viele Wissen, das er mir durch viele Ratschläge und Diskussionen vermittelt hat.

Lange Stunden im Labor vergehen am schnellsten, wenn man sie mit tollen Menschen teilen kann. Vielen Dank dafür an meine Laborkollegen David-Marcel Meier, Gregor Zitzer und Przemysław Głowacki. Bei Przemek möchte ich mich insbesondere für die gemeinsame Zeit am Experiment in München bedanken. Das lange Diskutieren und Grübeln über verwirrende Spektren hat sich mehr als ausgezahlt und ich behalte die Zeit in schöner Erinnerung.

Ich danke Burkhard Lipphard, Andreas Hoppmann, Thomas Leder und Martin Menzel für ihre umfassende technische Unterstützung, die unsere Experimente überhaupt erst ermöglicht. Vielen Dank auch an Martina Bäumler und Eva-Maria Berber für ihre unschätzbare Hilfe in allen Verwaltungsangelegenheiten, sowie an den gesamten Fachbereich 4.4 für die entspannte Arbeitsatmosphäre und die stete Hilfsbereitschaft.

Während meiner Arbeit traf ich in mehreren Kollaborationen auch auf viele großartige Kollegen außerhalb unserer Gruppe. Ein besonderer Dank gilt Peter G. Thirolf, Lars von der Wense und Benedict Seiferle von der Thorium-Gruppe an der LMU München, sowie Robert A. Müller für die wunderbare Zusammen-

arbeit. Darüber hinaus danke ich allen Kollegen der nuClock-Kollaboration und des SFBs DQ-mat für viele spannende Diskussionen.

Abschließend bedanke ich mich bei meiner Familie und insbesondere Susanne für sehr viel Verständnis und Geduld, sowie die unglaubliche Unterstützung über all die Jahre. Danke!

Curriculum Vitæ

Personal Data

Johannes Thielking

Born on 13th June 1988
in Minden, Germany

curriculum vitæ

1994 − 1999
Primary school in Hille, Germany

1999 − 2008
Grammar school in Espelkamp, Germany
Graduation: general qualification for university entrance

Jul. 2008 − Jun. 2009
voluntary social year at the Johanniter-Unfall-Hilfe e.V.
Bad Oeynhausen, Germany

Oct. 2009 − Oct. 2012
Study of physics (B.Sc.) at the University of Hamburg,
Germany

Oct. 2012 − Mar. 2015
Study of physics (M.Sc.) at the University of Hamburg,
Germany

from Aug. 2015
Ph.D. student at Physikalisch-Technische Bundesanstalt,
Braunschweig, Germany

Publications Laser spectroscopic characterization of the nuclear-clock isomer ^{229m}Th, Thielking et al., Nature **556**, 321-325 (2018), DOI: 10.1038/s41586-018-0011-8

Hyperfine interaction with the ^{229}Th nucleus and its low-lying isomeric state, Müller et al., Phys. Rev. A **98**, 020503(R) (2018), DOI: 10.1103/PhysRevA.98.020503

Nuclear Charge Radii of ^{229}Th from Isotope and Isomer Shifts, Safronova et al., Phys. Rev. Lett. **121**, 213001 (2018), DOI: 10.1103/PhysRevLett.121.213001

Electronic level structure of Th$^+$ in range of the ^{229m}Th isomer energy, Meier et al., Phys. Rev. A **99**, 052514 (2019), DOI: 10.1103/PhysRevA.99.052514